Institute for Geophysics, Astrophysics, and Meteorology
University of Graz

Atmospheric Remote Sensing and Climate System Research Group
ARSCliSys – on the art of understanding the climate system

IGAM/UG Technical Report for ESA/ESTEC No. 6/2001

ESA study:

ACE Scientific Support Study

[ESA/ESTEC Contract No. 14809/00/NL/MM, WP3000: Error Analysis for Climate Applications; Part WP3100]

Sensitivity of Atmospheric Profiles Retrieved from GNSS Radio Occultation Data to Instrumental Errors

by

J. Ramsauer and G. Kirchengast
(IGAM/University of Graz, Graz, Austria)

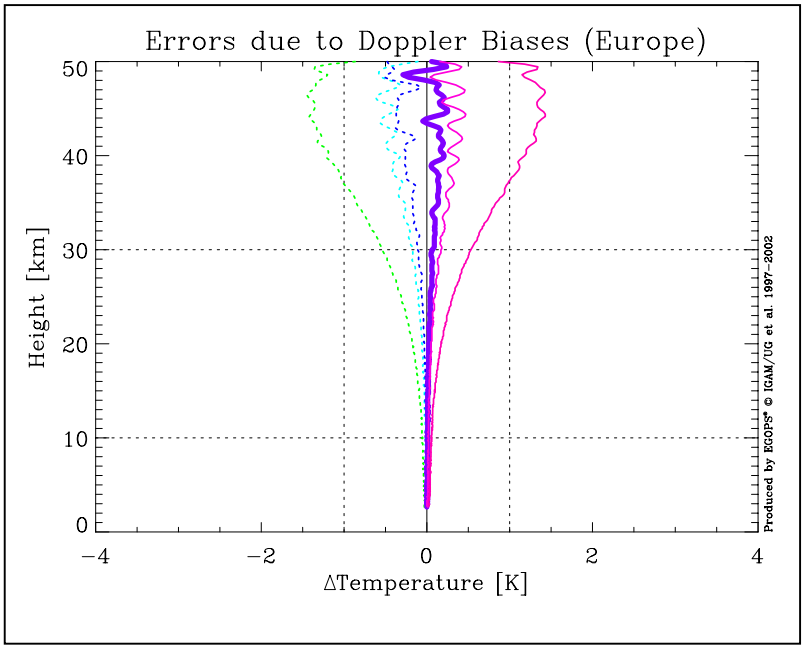

December 2001

Institute for Geophysics, Astrophysics, and Meteorology, University of Graz, Universitaetsplatz 5, A-8010 Graz, Austria
ARSCliSys E-Mail: arsclisys.igam@uni-graz.at, Web: http://www.uni-graz.at/igam-arsclisys

Table of Contents

1. INTRODUCTION

1.1. Instrumental Errors and Climate Applications

The main objective of the ACE (Atmosphere Climate Experiment) Scientific Support Study Work Package 3100 (WP3100) is to investigate the sensitivity of atmospheric profiles retrieved from GNSS (Global Navigation Satellite System) radio occultation data to instrumental errors. This instrumental error analysis inquires whether the accuracy expected to be reached with a state-of-the-art GNSS receiver (i.e., the GNSS Receiver for Atmospheric Sounding (GRAS) on the upcoming METOP weather satellites) is compliant with the instrument performance standards, which must be fulfilled for extensive climate applications of the radio occultation technique.

The study provides, in particular, a good overview on the individual behavior of different instrumental error sources and their importance for the whole error budget of the retrieved geophysical parameters. The results give a fair impression, which kind of errors are critical ones, were instrumental tolerances must be set very narrow to reach the needed output data quality and which instrumental errors sources are less critical for sucessful climate monitoring by means of GNSS radio occultation. Most computations for the study were done with the EGOPS (End to end GNSS Occultation Performance Simulator) software tool.

1.2. Study Overview

As mentioned above, the goal of WP3100 is to analyze a broad range of different instrumental errors on board the spacecraft and also of "instrumental" (general receiving system) errors, which occur in the ground segment. We analyzed the sensitivities of retrieval products to Doppler biases and bias drifts, clock stability/single-differencing errors, receiver noise, and errors due to local multipath, respectively. The total error obtained for a GRAS-type receiver was also summarized. The retrieval products explicitly addressed include the full range from bending angle via refractivity, pressure, and geopotential height to temperature profiles, respectively. Since the instrumental errors considered play no significant role in the troposphere, we performed dry air retrievals throughout.

As the main basis of the study we used two mutual-control occultation events (out of a set of 574 METOP/GRAS-type occultation events simulated over one day), forward modeled for them realistic phase delay data based on a high-resolution (T213L50) ECMWF (European Centre for Medium-Range Weather Forecasts) analysis field, and subsequently executed 3 to 6 different error cases per individual error source.

In order to cover the whole error source range we defined six basic error scenario groups. The retrieval results of all error scenario runs were then referred to results from associated reference runs, one with no errors at all (for internal control), the other one with typical (GRAS-type) errors for all "background" error sources (i.e., all error sources except the source of interest in a given scenario group). The latter was used as reference case for result plots.

In chapter 2 the study design and simulation setup are introduced. The whole set of results (comprising 70 individual plots) is shown and discussed in chapter 3. Finally, conclusions and an outlook are provided in chapter 4.

2. STUDY DESIGN AND SIMULATION SETUP

This chapter will give a description of the main steps necessary for the preparation of the individual instrumental error study analysis cases. We used the EGOPS software tool (Kirchengast, 1998a; Kirchengast *et al.*, 2001) – in a version close to the recent Version 4 – as "workhorse" for scenario preparation, data calculation, and for visualization and comparison of the resulting geophysical parameters. A limited number of modifications and extensions were made to the EGOPS tool in order to fully tailor it to study needs.

2.1. Selection of Occultation Events

The first step in investigating the error analysis cases was to search for two basic occultation events, which could give a fair control for potential event-dependent (e.g., location related) influences on the instrumental error results. What we finally selected as basic cases for the subsequent forward modeling calculations was one more northern rising occultation (about 50 deg North) and one tropical setting occultation event. For this purpose the EGOPS Mission Analysis/Planning (MAnPl) functionality was used. A one day MAnPl simulation scenario was prepared with input specifications as follows:

```
[*** MAnPl Input File for Task M ***]

-----------------------------------------------------------------------
[*Project-Id and Task-Id*]
Project-Id               = ACESS-WP3100
Task-Id                  = M
-----------------------------------------------------------------------

[*Data Type Selection*]
Data Type                = Occultation Data

[*UT Range*]
Start_Time               = 990915.000000  [yymmdd.hhmmss]
Simul_Time_Range         = 0240000        [hhhmmss]

[*Height Levels*]
Hlo1 Hhi1 HStep1 dh1     =    0.5   1.0   0.5  0.10  [km]
Hlo2 Hhi2 HStep2 dh2     =    1.0  15.0   7.0  0.10  [km]
Hlo3 Hhi3 HStep3 dh3     =   15.0  90.0  15.0  0.10  [km]

[*Geographic Area of Interest for Occultation Events*]
GeogrAreaChoice          = Global

[*GNSS-LEO Ray Treatment*]
RayTreatmentChoice       = Bended Line Rays

[*Earth Figure Model*]
EarthFigModelChoice      = Ellip.WGS84

[*GRAS Antennae Specifications*]
-V AntennnaChoice        = Used
-V BoresightElevation    =  27.0 [deg]
-V BoresightAzimuth      = 180.0 [deg]
-V FOVChoice             = Ell_Cartes
-V TPBW Vertical         =  60.0 [deg]
-V TPBW Horizontal       = 100.0 [deg]
```

```
+V AntennnaChoice         = Used
+V BoresightElevation     =  27.0 [deg]
+V BoresightAzimuth       =   0.0 [deg]
+V FOVChoice              = Ell_Cartes
+V TPBW Vertical          =  60.0 [deg]
+V TPBW Horizontal        = 100.0 [deg]

[*LEO Specifications*]
LEOOrbElemFilename        = leoMetOp199212.tle
LEOOrbModelChoice         = SGP Orbits (Impr. Kepler)

[*GNSS Specifications*]
GPS SatSystemChoice       = Standard
GPSOrbElemFilename        = gps99212.tle
GLON SatSystemChoice      = None
GNSSOrbitModelChoice      = SGP Orbits (Impr. Kepler)

[*Visibility Infos on Differencing*]
DiffVisInfChoice          = No_Diff_Vis_info
TrackVisInfChoice         = No_Track_Vis_info

[*** EOF MAnPl Input File for Task M ***]
```

Here is a brief summary of the major settings. The simulation start time was set to September 15, 1999, 0 UT (the date of the high-resolution ECMWF T213L50 analysis field then employed in the forward modeling), and the simulation time range was set to 24 hours. A sufficiently dense set of height levels was used and both GRAS antennae (+v antenna for rising and –v antenna for setting events) were activited, with a reasonable horizontal coverage (±50 deg azimuthal range). The nominal METOP satellite orbit was used as LEO orbit and the nominal GPS system (24 satellites) was selected for acting as transmitter satellite system.

The result of the MAnPl simulation is shown in Figure 2.1. From the illustrated set of 574 occultation events two representative ones as noted above were selected for further Forward Modeling (FoMod) calculations. Figure 2.2 shows occultation number 506, the more northern occultation event located over central Europe, whereas Figure 2.3 displays the selected tropical occultation, occultation number 188 near the Hawaiian Islands. One can clearly see that the rising occultation 506 starts over Tyrol (Austria) and ends in south-western Germany (from the Austrian alps to more flat regions in Germany). In contrast the chosen setting occultation event number 188 is located completely over the Pacific ocean near Hawaii.

In Figures 2.2 and 2.3, the small triangle denotes the beginning of the curved tangent point trajectory (in case of a rising occultation it is the footpoint of the tangent point trajectory, whereas for a setting occultation it marks the highest point of the tangent point trajectory). The bundle of "levers" about the tangent point trajectory indicate the along-ray directions between the transmitting GPS and the receiving LEO satellite (the number of rays, each corresponding to a simulated height level, can be freely adjusted in EGOPS). From the angular positions of the rays with respect to the tangent point trajectory one can get a good feeling on the "verticality" of the occultation event (i.e., if it is extremely smearing one should expect a degraded tropospheric data quality for the retrieved physical parameters later on). The two events chosen represent typical average occultation cases, neither particularly vertical nor extremely smearing.

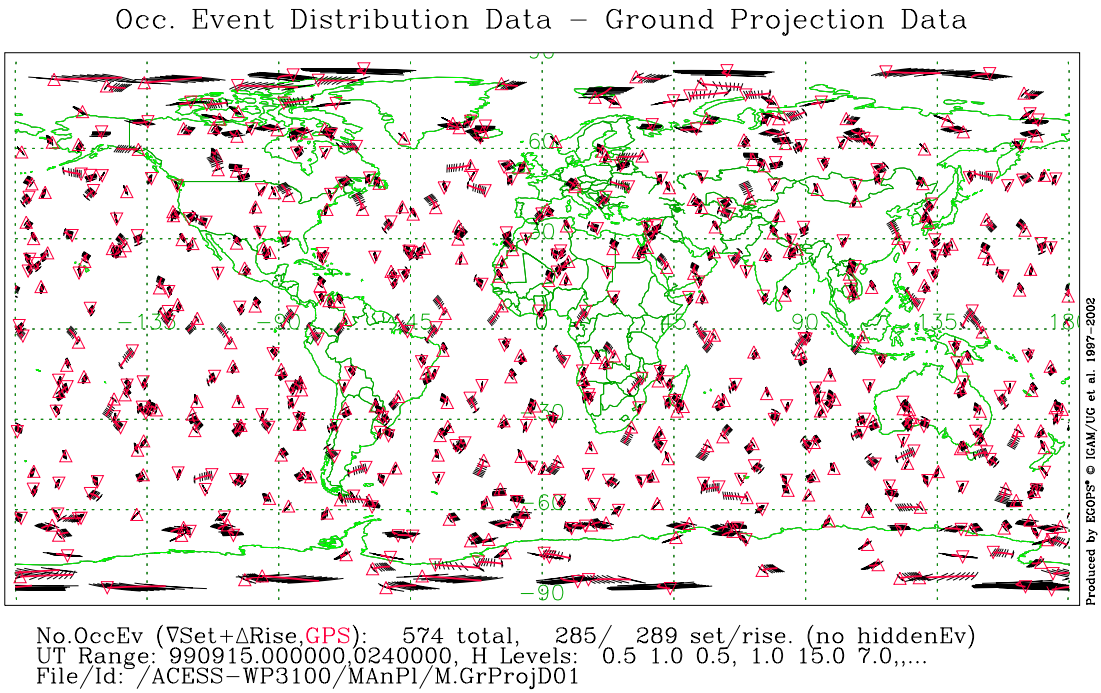

Figure 2.1: Occultation event distributation data for the full day.

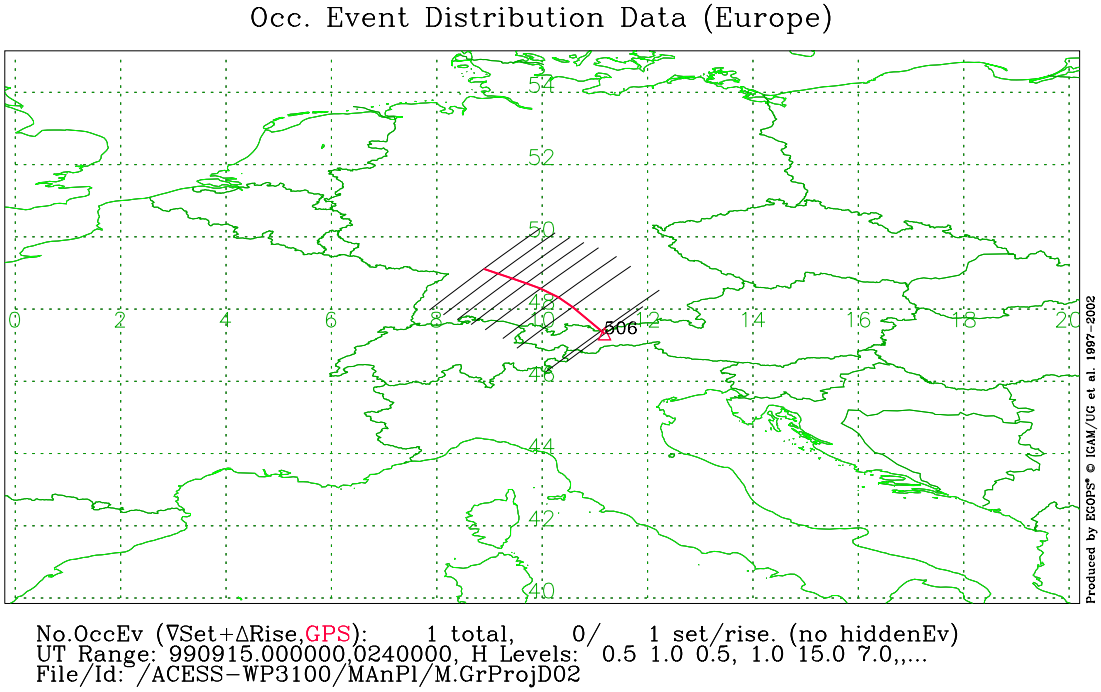

Figure 2.2: Occultation number 506 (rising occultation), termed "Europe" event in the result plots.

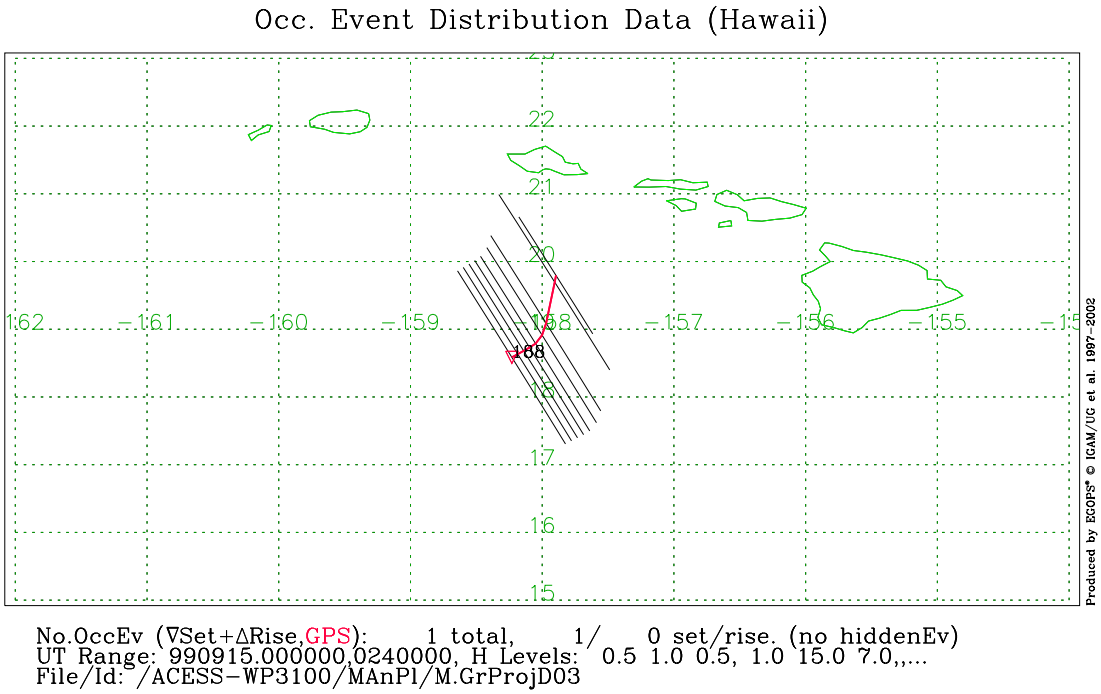

Figure 2.3: Occultation number 188 (setting occultation); termed "Hawaii" event in the result plots.

2.2. Forward Modeling

The next major step in preparing the different instrumental error analysis sets is the calculation of the pure (ideal) time-tagged phases and amplitudes without any instrumental error effects, the so called Forward Modeling (FoMod). These FoMod calculations were done with the help of the EGOPS FoMod processing functionality. Two separate FoMod simulations had to be done, one for each selected occultation, with all relevant physical input parameters identical for both cases.

Forward Modeling itself denotes the simulation of GNSS signal propagation through the atmosphere/ionosphere system, given the orbital motions of the GNSS and LEO satellites. This results in "ideal" signals, which contain the effects of the atmosphere/ionosphere media only. Ideal in the sense that it is the state of the signal right before it enters the receiving antenna and before any degradations by the receiving system are incurred. Thus FoMod results allow to inspect the environmental influence alone.

One could also introduce instrumental errors at this step but this is not very useful because the FoMod signal propagation simulation (high-precision ray tracing) is rather CPU-time consuming and such combination would thus be a very impractical. Within EGOPS, the FoMod process is thus completely separated from sensor degradations, or Observation System Modeling (OSMod). The latter was extensively employed for this study and is described in section 2.3.

A typical FoMod input is shown here for one of the selected occultations ("Europe" event):

```
[*** FoMod Input File for Task F-E ***]

------------------------------------------------------------------
[*Project-Id and Task-Id*]
Project-Id               = ACESS-WP3100
Task-Id                  = F-E
------------------------------------------------------------------

[*Occ. Event Simulation Type/Specifications*]
OccEventSimulType        = Single Event/Realistic Geometry
OccEv.HeightRange        =    0.5  90.0 [km]
ReferenceMAnPl/Task-Id   = M
OccNoRange               =   506  506    0

[*Atmospheric Models Choice/Specifications*]
AtmClimModelChoice       = GCM 3D Atmosphere (GCM3DAtm)
GRIB Data FilePath       = /home/jra/EGOPS/EGOPS4/test4/Daten/
GRIB Data FileName       = ecmwf19990915121.grb
Humidity Choice          = Humidity included (moist air)
AtmModelStructureChoice  = Atmos. Model Structure as is
AtmDistModelChoice       = No Atmos. Disturbance superposed

[*Ionospheric Models Choice/Specifications*]
IonClimModelChoice       = 3D Ionosphere (Iono3D_UoG)
Sol.Act./F10.7 index     = 130 [10-22Wm-2Hz-1]
IonModelStructureChoice  = Ionos. Model Structure as is
IonDistModelChoice       = No Ionos. Disturbance superposed

[*Forward Modeling Sampling Rates*]
GPS Sampling Rates       =   10.0  10.0 [Hz]
GLON Sampling Rates      = No GLON Event

[*Signal Propagation Simulator Specifications*]
PropSimulatorType        = Full-3D Ray Tracer
PropSimulatorAccuracy    = <  ~1 mm

[*Earth Figure Model*]
EarthFigModelChoice      = Ellip.WGS84

[*GNSS-LEO Ray Treatment*]
RayTreatmentChoice       = Bended Line Rays

[*GRAS Antennae Specifications*]
-V AntennnaChoice        = Not Used
+V AntennnaChoice        = Used
+V BoresightElevation    =  27.0 [deg]
+V BoresightAzimuth      =   0.0 [deg]
+V FOVChoice             = Ell_Cartes
+V TPBW Vertical         =  60.0 [deg]
+V TPBW Horizontal       = 100.0 [deg]

[*LEO Specifications*]
LEOOrbElemFilename       = leoMetOp199212.tle
LEOOrbModelChoice        = SGP Orbits (Impr. Kepler)

[*GNSS Specifications*]
GPS SatSystemChoice      = Standard
GPSOrbElemFilename       = gps99212.tle
GLON SatSystemChoice     = None
GNSSOrbitModelChoice     = SGP Orbits (Impr. Kepler)

[*** EOF FoMod Input File for Task F-E ***]
```

The only difference between the two FoMod input files involved in the study is (in addition to their different occultation numbers) that for occultation number 188 (a setting occultation) the –v antenna was applicable, instead of the +v antenna for the rising occultation number 506.

The atmospheric model used was the GCM 3D Atmosphere (GCM3DAtm) with a high-resolution (T213L50) ECMWF analysis data file (ecmwf19990915121.grb) as input data file. For the FoMod calculations humidity was included.

As ionospheric model, the 3D Ionosphere (Iono3D_UoG), a 3 dimensional ionosphere model developed at IGAM/University of Graz was chosen; the solar activity index F10.7 index was set to 130 – a typical value for medium solar activity. The receiver sampling rate was set to 10 Hz and as signal propagation simulator the EGOPS Full-3D Ray Tracer model with a propagator simulator accuracy of better than 1 mm was used. The results of these simulations were then used as the "ideal" input signal (phases and amplitudes) for the subsequent Observation System Modeling.

As an illustration of the realistic variability involved in the ECMWF analysis field employed, we show in Figures 2.4 and 2.5 two longitude slices of the temperature field. These slices give a good overview of temperature variations at the 10 deg East meridian and the 158 deg West meridian, just where the two selected occultation events occurred. In our context, the reasonably large stratospheric temperature variations are of interest, which ensure a good representation of real measurement conditions.

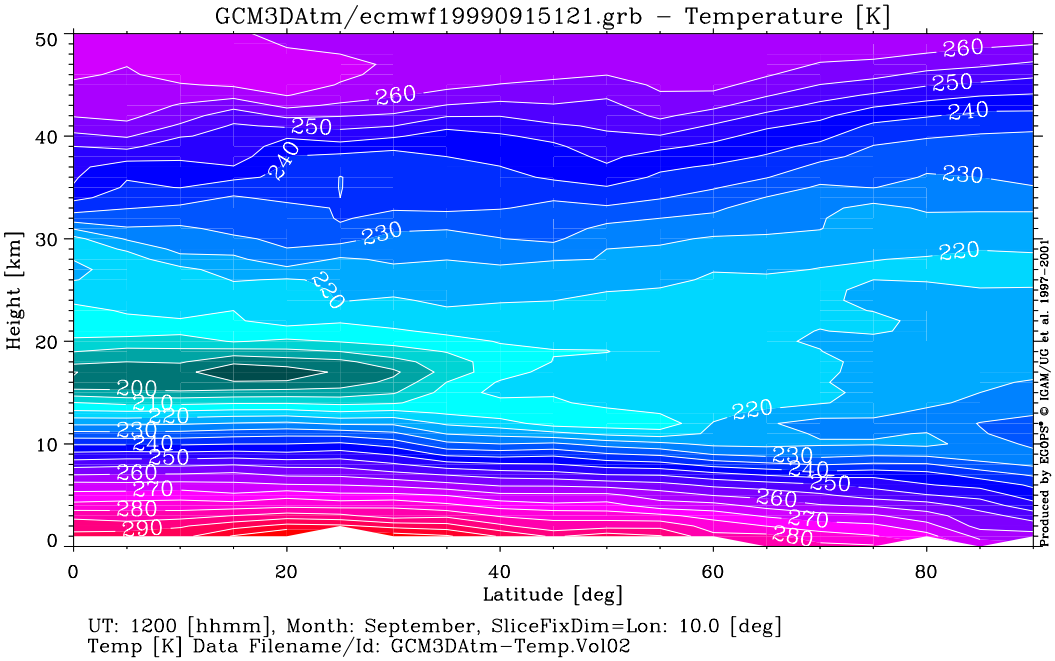

Figure 2.4: ECMWF T213L50 temperature field. Latitude-height slice at 10 deg East.

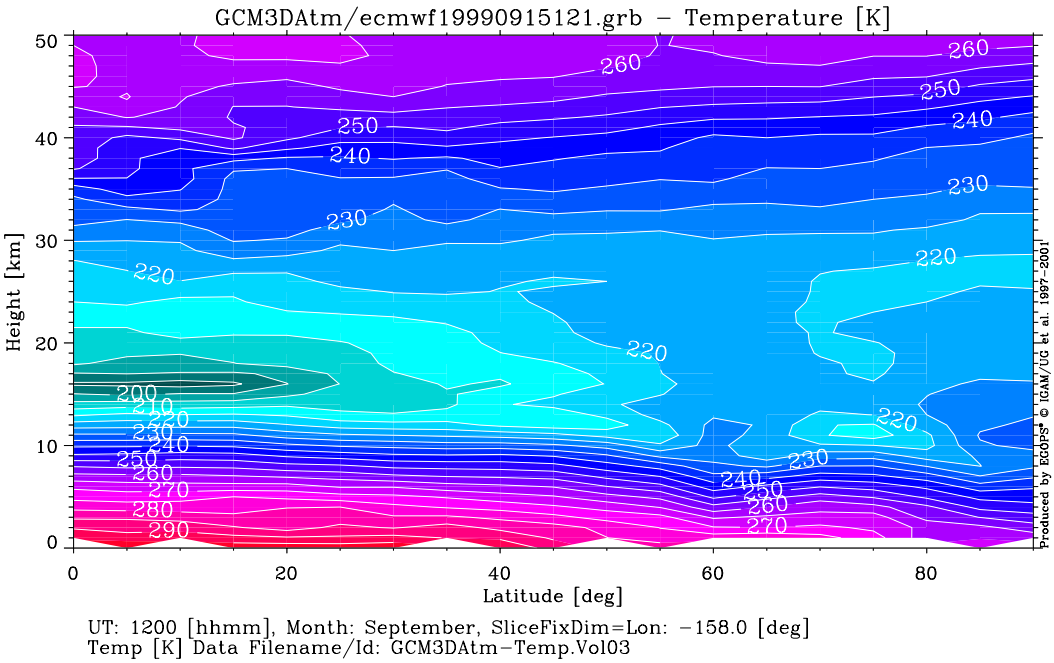

Figure 2.5: ECMWF T213L50 temperature field. Latitude-height slice at 158 deg West.

2.3. Instrumental Error Simulations

After having produced two ideal FoMod data sets we are now ready for introducing the main part of the study, the instrumental error simulations. Like in the two former cases (MAnPl and FoMod), the EGOPS S/W tool plays a key role here, with its Observation System Modeling (OSMod) functionality for different kinds of instrumental error simulations. The OSMod together with prior FoMod calculations performs quasi-realistic simulations of observables, and related auxiliary variables, of the GNSS occultation technique. The resulting main observables are time-tagged phase and amplitude measurements, directly mimicking those obtained in the real world via tracking GNSS signals with a LEO-mounted GRAS sensor during their setting or rising through the atmosphere due to orbital motion of the GNSS and LEO satellites.

Observation System Modeling itself denotes the superposition of all sorts of relevant physical and technical influences of the observation system (antenna, receiver, platform, fiducial sites) on the ideal signal (phase and amplitude data) arriving at the receiving antenna, and on the ideal orbit data (GNSS and LEO positions and velocities).

In this study we deal with four separate types of instrumental errors, which are investigated within six different error scenario groups. The first type comprises Doppler biases (scenario group 1) and Doppler drifts (group 2), the second type clock stability/single-differencing errors (group 3). The third type is concerned with receiver noise (group 4) and the fourth type addresses errors due to local multipath (groups 5 and 6). Before we started with error scenarios in all these scenario groups, a set of two "master cases" per occultation event was prepared in advance.

One master case was the so-called "ideal case", where all possible instrumental errors were set to zero. This case was utilized as an internal control case, confirming that the full forward-inverse processing chain was consistent and correct. The second master case was prepared with GRAS-type instrumental errors for all error sources (conservative values) in order to estimate the total errors, which may be associated with a GRAS-type sensor. The results of this "standard case" (total GRAS error minus ideal case) are illustrated at the end of chapter 3 (section 3.7) after discussing the results of all indivdual error components.

As an example for the input involved in OSMod simulations, the OSMod input parameters are shown below for the "standard case" ("Europe" event):

```
[*** OSMod Input File for Task O-ED ***]

-----------------------------------------------------------------
[*Project-Id and Task-Id*]
Project-Id               = ACESS-WP3100
Task-Id                  = O-ED
-----------------------------------------------------------------

[*Occ. Event Simulation Type/Specifications*]
OccEventSimulType        = Single Event/Realistic Geometry
OccEv.HeightRange        =    0.5  90.0 [km]
ReferenceFoMod/Task-Id   = F-E
OccNoRange               =   506  506    0
```

```
[*Receiver Sampling Rates*]
GPS Sampling Rates       =   10.0  10.0 [Hz]
GLON Sampling Rates      = No GLON Event

[*Transmitter Signal Powers*]
L1-C/A L2-P GPS Powers   =  27.0 20.0 [dBW]
L1-C/A L2-P GLON Powers  = No GLON Event

[*POD Error Modeling/Specifications*]
PODErrorModelChoice      = Kinematic POD Error Model
ErrApplicationType       = As specified
RadialPositionErrorGNSS  =   0.20 [m]
RadialPositionErrorLEOs  =   0.40 [m]
AlongRayVelocityError    =   0.05 [mm/s]
AlongRayAccelError       =   0.05 [µm/s²]

[*Receiving System Simulator Specifications*]
Rec. Sys. Simulator      = Parameterized Receiving System Simulator

[*GRAS Antennae Modeling*]
-V AntennaChoice         = Not Used
+V AntennaChoice         = Used
+V BoresightElevation    =  27.0 [deg]
+V BoresightAzimuth      =   0.0 [deg]
+V FOVChoice             = Ell_Cartes
+V HPBW Vertical         =  60.0 [deg]
+V HPBW Horizontal       = 100.0 [deg]
+V AntennaGain/Boresight =  11.0 [dB]

[*Receiver Performance Modeling*]
RecPerfModelChoice       = Realistic Perf./Noise Model
LoopBandwidth/singleside =  10.0 [Hz]
LEOAntennaeNoiseTemp     = 150.0 [K]
QuantLevelsADConversion  =   4

[*Local Multipath Modeling*]
LocalMultipModelChoice   = Sinusoidal Multipath Model
MultiPhaseErrPeriod      =   300.0    0.0    0.0    0.0 [sec]
MultiPhaseErrAmplitude   =   1.0  0.0  0.0  0.0  [mm]
MultiPhaseErrAmplTopRay  =   0.0  0.0  0.0  0.0  [mm]

[*Differencing Treatment/Clocks Modeling*]
DiffTreatmentChoice      = Groundb. Single Differencing
RelStabilityofWorstClock = 1.0E-13 [1secAllan]
AtmNoise per Groundlink  = 1.0E-13 [1secAllan]

[*Atmospheric Models Choice/Specifications*]
AtmClimModelChoice       = GCM 3D Atmosphere (GCM3DAtm)
GRIB Data FilePath       = /home/jra/EGOPS/EGOPS4/test4/Daten/
GRIB Data FileName       = ecmwf19990915121.grb
Humidity Choice          = Humidity included (moist air)
AtmModelStructureChoice  = Atmos. Model Structure as is
AtmDistModelChoice       = No Atmos. Disturbance superposed

[*Ionospheric Models Choice/Specifications*]
IonClimModelChoice       = 3D Ionosphere (Iono3D_UoG)
Sol.Act./F10.7 index     = 130 [10-22Wm-2Hz-1]
IonModelStructureChoice  = Ionos. Model Structure as is
IonDistModelChoice       = No Ionos. Disturbance superposed

[*Earth Figure Model*]
EarthFigModelChoice      = Ellip.WGS84

[*** EOF OSMod Input File for Task O-ED ***]
```

In the "ideal case", the precise orbit determination (POD) error modeling/specifications were set to "No POD Errors", the receiver perfomance modeling to "No Receiver Noise", local multipath modeling to "No Local Multipath", and the differencing treatment/clocks modeling to "No Differencing/Perfect Clocks", respectively. Thus, the "ideal case" does not affect the FoMod signal in any way (it just "carries through" the FoMod data, thus representing the case of no instrumental errors being present).

More important in the present context is the "standard case" (input listed above), because we have used these specification values in each individual error scenario analyzed for specifying the "background" errors, i.e., for all input values except the parameter of interest varied in a given scenario group (see sections 2.3.1 to 2.3.4 for details on parameter ranges tested).

Briefly explaining the "standard case" values (also termed "standard setting" hereafter), the most relevant standard POD errors are the standard along-ray velocity error of 0.05 mm/s, and the standard along ray acceleration error of 0.05 μm/s² (the possible errors for the radial positions of the GNSS or LEO satellite were always fixed to 0.2 m for the GNSS and 0.4 m for the LEO satellite system). For the receiver performance modeling, the standard value for the loop bandwith/single-side was set to 10 Hz, the LEO antenna noise temperatur to 150 K, and the number of quantization levels for A/D conversion to 4. Local multipath modeling was done by means of a sinusodial multipath model, where the standard multipath phase error period was set to 300 sec, the multipath phase error amplitude to 1 mm, and the standard multipath phase error amplitude at the topmost ray was set to 0 mm. For differencing treatment/clocks modeling ground-based single-differencing was used, with the standard values for relative stability of worst clock and atmospheric noise per ground link set to a 1-sec Allan deviation of 1×10^{-13}.

After computation of the four basic OSMod scenarios (the ideal and the standard case for both the "Europe" and the "Hawaii" event), the next step was to prepare the different instrumental error sets.

2.3.1. Doppler Bias and Doppler Drift Scenarios

These first two error scenario groups deal with errors introduced to the system due to Doppler biases and Doppler drifts (e.g., present due to POD residual errors). The kinematic EGOPS precise orbit determination (POD) error model was used for the purpose. This model mimicks POD position errors mainly by considering radial GNSS and LEO position errors, POD velocity errors by considering along-ray velocity bias and drift errors superposed to the ideal LEO velocity, and POD-induced excess phase errors by introducing along-ray excess phase drift and acceleration errors corresponding, after time derivation, to the Doppler bias and drift errors we focus on in this study.

Both the along-ray velocity errors (for Doppler bias estimation) and the along-ray acceleration errors (for Doppler drift estimation) were varied independently, and this performed for both the "Europe" and the "Hawaii" event, while all other OSMod input parameters were left at their standard setting introduced above.

The Doppler bias errors were simulated via variation of the along-ray velocity errors, whereby seven different representative velocity error scenarios were defined: -0.3, -0.1, -0.05, 0, 0.05, 0.1, 0.3 [mm/s]. (standard velocity error is 0.05 mm/s). The Doppler drift errors were simulated via variation of the along-ray acceleration errors, whereby again seven different acceleration error scenarios were defined: -0.3, -0.1, -0.05, 0, 0.05, 0.1, 0.3 [μm/s²] (standard acceleration error is 0.05 μm/s²).

The result of these Doppler bias and Doppler drift error scenario calculations are two sets (one for each "Europe" and "Hawaii") of 14 error-modified phase and amplitude output files (7 for Doppler bias and 7 for Doppler drift) waiting for later inversion/retrieval (InRet) processing.

2.3.2. Clock Stability/Single-Differencing Errors Scenarios

The third instrumental error scenario group was built around clock stability/single-differencing errors. For this purpose the EGOPS differencing treatement and clocks modeling functionality (relatively simple clock error models, which allow to mimick several different ground- and space-based single- and double-differencing scenarios) was used. We focused on the ground-based single-differencing clock correction method baselined for the METOP/GRAS operational processing. Ground-based single-differencing effectively implies that the relative stability of the LEO clock (assumed the worst clock in case of ground-based single-differencing) and the atmospheric noise for the ground-to-satellite link are involved the differencing process, respectively.

Four individual clock stability/single-differencing error scenarios were prepared and analysed. These scenarios were defined by different values for the relative stability of the LEO clock; we used the following clock error input values: 0, 1×10^{-13}, 3×10^{-13}, and 1×10^{-12} [1sec Allan] (standard case is 1×10^{-13}). All other settings in the OSMod input file where kept at their "standard case" values.

The result of these clocks/differencing-induced error scenario calculations are a set of 8 error-modified phase and amplitude output files (4 for each the "Europe" and "Hawaii" event).

2.3.3. Receiver Noise Scenarios

In the fourth instrumental error scenario group, the influence of the receiver noise on the output signal quality was studied. For this purpose the EGOPS-internal realistic receiver perfomance/noise model, which simulates phase and amplitude measurement errors with realistic "RMS" characteristics, was employed. The input specifications for this realistic performance/noise model are the loop bandwidth (single-sided), the LEO antenna noise temperature, and the number of quantization levels used in A/D conversion, respectively.

For the receiver noise study, four different error scenarios were executed, beginning from an ideal case (no receiver noise) up to a LEO antenna noise temperature of 250 K with 25 Hz loop bandwidth. More precisely, besides the no receiver noise case the following combinations of LEO antenna noise temperatures and single-side loop bandwidths were introduced: 150 K/10 Hz (the standard case), 150 K/25 Hz, and 250 K/25 Hz. All other settings in the OSMod input file where kept at their "standard case" values.

The results of these altogether eight error scenario runs (4 for each the "Europe" and "Hawaii" event) were obtained in the same OSMod output files form as already noted above.

2.3.4. Local Multipath Error Scenarios

The fifth and sixth instrumental error simulation scenario group focused on local multipath error analysis. Such local multipath signatures can be introduced to the measured observables by local platform structures in the vicinity of the receiving GRAS antennae. Like in all former error scenario runs, the EGOPS S/W tool was used for the local multipath error simulations.

For both analyzed local multipath scenario groups – one addressing local multipath amplitude (fifth group), the other one phase (sixth group) – a simple sinusoidal multipath model was used, which simulates sinusoidal phase measurement errors with user specified amplitude, period, and amplitude start value, respectively.

Within the fifth scenario group, four different error cases of varying phase error periods & phase error amplitude due to multipath were formulated: 0 (no local multipath), 300 s/1 mm (standard case), 100 s/1 mm, and 100 s/2 mm. For all these cases, the local multipath phase error amplitude of the topmost ray was fixed to the standard value of 0 mm. All other settings in the OSMod input file where kept at their "standard case" values.

Within the sixth scenario group, the phase error period and amplitude due to multipath were fixed to 300 s/1 mm (their standard values) and only the phase error amplitude of the topmost ray was varied between the two cases –1 mm and +1 mm. In addition, now fixing the multipath period and amplitude to 100 s/2 mm, the error amplitude at the topmost ray was set to either –2 mm or +2 mm, respectively. Again, all other settings in the OSMod input file where kept at their "standard case" values.

The calculations for these alltogether eight local multipath cases for each the "Europe" and the "Hawaii" event were performed with EGOPS in the same manner as the other cases before. After finishing these last OSMod simulation runs, all output data sets must be processed with atmosphere profile retrieval algorithms for finally obtaining the retrieved geophysical variables such as bending angle, refractivity, and temperature.

2.3.5. Total GRAS-type Error Budget

For the "standard case" with GRAS-type errors, the total excess phase error and its components from the different instrumental error sources have been inspected more closely, for both the "Europe" and "Hawaii" event. This served to check whether the error modeling is reasonable in general and whether the two events are representative, given that all random sequences involved in the OSMod algorithms had to be frozen to fixed realizations for all scenarios in order to allow meaningful comparison of different error magnitudes, unobscured by random behavior. Figure 2.6 depicts the total phase error together with its components and confirms that the two events furnish reasonably representative GRAS-type error behavior with total error magnitudes at the order of 1 mm.

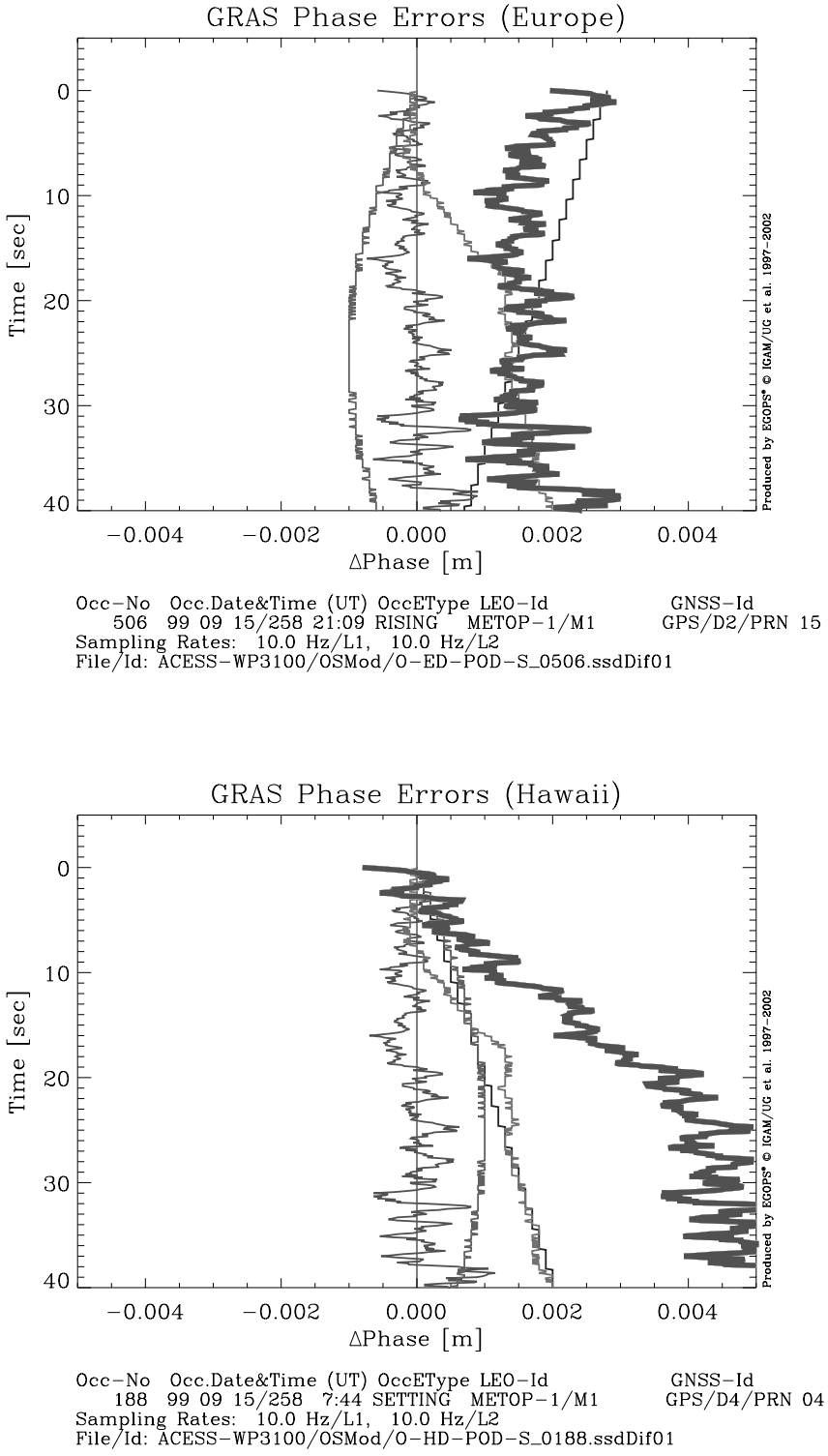

Figure 2.6: GRAS-type excess phase error components and total error. Doppler residual (black, linear curve), receiver noise (dark-grey, oscillating curve), local multipath error (medium-grey, sine-shaped curve), clocks/single-differencing error (light-grey curve), and total phase error (heavy dark-grey curve; sum of all error components) are shown. For better visualization in this figure, the receiver noise and total error curves are filtered to ~1 Hz rate (11-point running mean over the 10 Hz data).

The event time range illustrated (first 40 sec for the event starting at 90 km height) reaches down to below 10 km into the troposphere. The "Europe" event represents a typical realization, where the Doppler error within the first 20 sec (90 km to ~35 km height) – the decisive factor for retrieval accuracy – is somewhat variable and reaches bias levels of > 0.1 mm/s only over several seconds (~0.15 mm/s over the first about 8 sec). The "Hawaii" event represents a more worse case, where the error components incidentally add in a fairly coherent manner as to maintain a Doppler bias of ~0.15–0.2 mm/sec over the full first 20 sec. It is thus to be expected that the latter event will generally lead to somewhat higher retrieval errors than the former. Section 3.7, which shows the retrieval errors for the GRAS-type "standard case" for all geophysical products considered, confirms this expectation; especially pressure and geopotential height results exhibit markedly increased errors in case of the "Hawaii" event.

2.4. Atmosphere Profiles Retrieval

The last step necessary in the instrumental error simulation process is the Inversion/Retrieval (InRet) data processing again performed by means of the EGOPS software. The atmosphere profiles retrieval of occultation data (supplemented by additional necessary geometrical information) proceeds from phases via Doppler shifts and bending angles down to quasi-vertical atmospheric profiles of refractivity, pressure, temperature, and others as needed. This processing chain typically requires, sequentially, tools for ionospheric correction and conversion of the excess phase observables to neutral-atmospheric bending angle profiles, for inversion of bending angle profiles into refractivity profiles (inverse Abel transform), and for finally retrieving the atmospheric variables (pressure, geopotential height, and temperature) from refractivity. In our retrieval simulations the air in the troposphere was assumed dry in the last stage of this processing chain, since we focus on stratospheric errors where moisture does not play a role.

The InRet input specifications for the different atmosphere profiles retrieval cases were set identical for all OSMod instrumental error scenarios (except that, of course, the Task-Ids change, both for InRet tasks and reference OSMod tasks). The following InRet input file listing shows the Inversion/Retrieval processing input settings for processing the GRAS-type "standard case" ("Europe" event):

```
[*** InRet Input File for Task I-ED ***]

-----------------------------------------------------------------
[*Project-Id and Task-Id*]
Project-Id               = ACESS-WP3100
Task-Id                  = I-ED
-----------------------------------------------------------------

[*Occ. Event Type/Specifications*]
OccDataType              = SimData
OccEventType             = Single Event/Realistic Geometry
OccNoRange               =   506  506    0
OccEv.HeightRange        =    0.5  90.0 [km]
ReferenceOSMod/Task-Id   = O-ED

[*Bending Angle Retrieval Specifications*]
BendAngleRetToolChoice   = DMI Enhanced Ion.Corr. & Bend.Angle Retrieval
IonoCorrectionType       = Bend.Angle Correction
StatOptimizationType     = Optimize using glob. BenA Search
```

```
[*Refractivity Profiles Retrieval Specifications*]
RefProfRetToolChoice     = DMI Abel Transform Atmos.Refr.Profile Retrieval

[*Atmospheric Profiles Retrieval Specifications*]
AtmProfRetToolChoice     = DMI Dry Air Prof. Retrieval

[*Atmospheric Models Choice/Specifications*]
AtmClimModelChoice       = GCM 3D Atmosphere (GCM3DAtm)
GRIB Data FilePath       = /home/jra/EGOPS/EGOPS4/test4/Daten/
GRIB Data FileName       = ecmwf19990915121.grb
Humidity Choice          = Humidity included (moist air)
AtmModelStructureChoice  = Atmos. Model Structure as is
AtmDistModelChoice       = No Atmos. Disturbance superposed

[*Ionospheric Models Choice/Specifications*]
IonClimModelChoice       = 3D Ionosphere (Iono3D_UoG)
Sol.Act./F10.7 index     = 130 [10-22Wm-2Hz-1]
IonModelStructureChoice  = Ionos. Model Structure as is
IonDistModelChoice       = No Ionos. Disturbance superposed

[*Earth Figure Model*]
EarthFigModelChoice      = Ellip.WGS84

[*** EOF InRet Input File for Task I-ED ***]
```

For the bending angle retrieval we used the "DMI Enhanced Ionospheric Correction & Bending Angle Retrieval" tool with the linear correction of bending angles as ionosphere correction type. Statistical optimization including background bending angle search was also included (the background profiles frozen, after best-fit search based on the "standard case", for both the "Europe" and the "Hawaii" event, in order to ensure identical InRet processing of all scenarios involved). This bending angle retrieval tool was in its basic form developed by Syndergaard (1999) and since then enhanced at IGAM to the present advanced algorithm, which was also employed as "high end" algorithm in the WP3200 work reported by Gobiet and Kirchengast (2001).

Refractivity profiles retrieval and the subsequent dry air profiles retrieval were accomplished by means of standard inverse Abel transform and dry air processing tools, respectively, developed as well by Syndergaard (1999) and integrated by IGAM into EGOPS, after implementing several extensions (e.g., recently computation of geopotential heights added). For more details on algorithms see the companion reports on WP3200 (Gobiet and Kirchengast, 2001) and WP3300 (Foelsche and Kirchengast, 2001), and references therein.

The InRet processing was performed for the complete set of dozens of OSMod scenarios introduced in section 2.3. After finishing all these InRet computations, the material is now ready for producing meaningful graphical outputs of the large ensemble of different instrumental error analysis results obtained.

3. ERROR ANALYSIS RESULTS

The error analysis result plots illustrate all results in terms of absolute error profiles (temperature and geopotential height) or relative error profiles (pressure, refractivity, and bending angle), respectively. For each of the six main scenario groups — Doppler biases, Doppler drifts, LEO clocks/single-differencing errors, receiver noise, local multipath/period and amplitude dependence, local multipath/phase dependence — the errors are defined and visualized as deviation against the "ideal" case of the group, i.e., the case where the sensitivity parameter(s) of interest was(were) set to zero error. For example, Doppler bias error plots show the Doppler bias errors with reference to the profiles obtained with zero along-ray velocity error. In a seventh group the results for the GRAS-type total errors are shown.

In total, 35 result figures with two panels each (upper panel "Europe" event, lower panel "Hawaii" event) were produced, each panel containing up to six separate instrumental error case results. 35 figures resulted in total, since for each of the six scenario groups plus for the seventh group on GRAS-type total errors, the results on temperature, pressure, geopotential height, refractivity, and bending angle are displayed and discussed.

For convenient identification of the individual results from the different instrumental error cases in a panel, we used three different graphical measures for all plot panels. First, different greyscales were used for displaying the individual results (smallest/most negative error specification value darkest, highest/most positive value lightest). Second, profiles obtained for negative specification values are shown as dotted lines, whereas errors from positive values are shown as solid lines. Third, a markedly more heavy line thickness was used to indicated the result for the GRAS-type standard case. The only exception from these rules was introduced for the local multipath errors/phase dependence plots; this is separately explained in section 3.6. For displaying the total errors in section 3.7 only one profile per plot was required, as only the GRAS-type standard case is shown.

In general, regarding the size of errors found, increasingly larger error specification values lead to increasingly larger error amplitudes in the result plots. This is in line with the basic expectation, that there should basically prevail a continuous, not too non-linear, mapping between input error size in OSMod parameters and observed output errors in retrieved profiles.

3.1. Doppler Biases

In this first error scenario group we analyzed the sensitivity of retrieved profiles to errors introduced due to Doppler biases. Section 2.3.1 above provided details on the error specifications used. Briefly recalled, the Doppler bias errors were simulated via variations of the POD along-ray velocity error value, while all other OSMod input parameters were kept at their standard value. The seven velocity error values explored were –0.3, –0.1, –0.05, 0, 0.05, 0.1, and 0.3 [mm/s], respectively. The reference case, i.e., the "zero line" in the error plots, is 0 mm/s; the GRAS-type standard case is 0.05 mm/s (marked as heavy line in the error plots).

The results of the Doppler bias error calculations are displayed in Figures 3.1.1 to 3.1.5, in the order temperature, pressure, geopotential height, refractivity, and bending angle.

The temperature error results are displayed in Figure 3.1.1. Common results for both occultation sites, "Europe" and "Hawaii", are that even in the two worst case Doppler bias error scenarios (POD along-ray velocity errors –0.3 mm/s, the leftmost dark grey dotted line and 0.3 mm/s, the rightmost light grey solid line) the temperatur errors up an altitude of 10 km are < 0.1 K and gradually grow to more than ±1 K at heights > 35 km. For the GRAS-type error case (0.05 mm/s, heavy solid line), the temperature error is confined to < 0.1 K up to a height of 30 km and reaches values of ~0.3 K at the stratopause. Up to 30 km all six Doppler bias error cases exhibit a more or less smoothly diverging character, whereas in the upper stratosphere some higher-frequency fluctuations become more and more visible.

The same general picture applies to the pressure, geopotential height, and refractivity Doppler bias errors, which are displayed in Figures 3.1.2., 3.1.3., and 3.1.4, respectively. Errors are very small (< 0.1%) for altitudes lower than about 20 km (pressure) or 30 km (refractivity) and then gradually grow with increasing heights. For the geopotential height errors the same is generally true, with errors < 5 gpm for altitudes lower than about 15 km. In contrast to the smooth behavior of the pressure and geopotential height errors (smeared by hydrostatic integration), the refractivity errors exhibit some fluctuations in the upper stratosphere. The errors are growing to about ±1.5% (pressure), about 100 gpm (geopotential height), and about ±1% (refractivity), respectively, at the stratopause.

The bending angle errors, which are displayed in Figure 3.1.5, are also very small (< 0.1%) for altitudes lower than 30 km, and their maximum amplitude near the stratopause is compareable to the one of refractivity errors. The bending angle errors exhibit significantly more oscillatory behavior in the upper stratosphere, however, due to less smoothing involved at this retrieval level early in the processing chain. Slightly different impact parameter errors obtained for the different scenarios have presumably contributed to the oscillatory behavior.

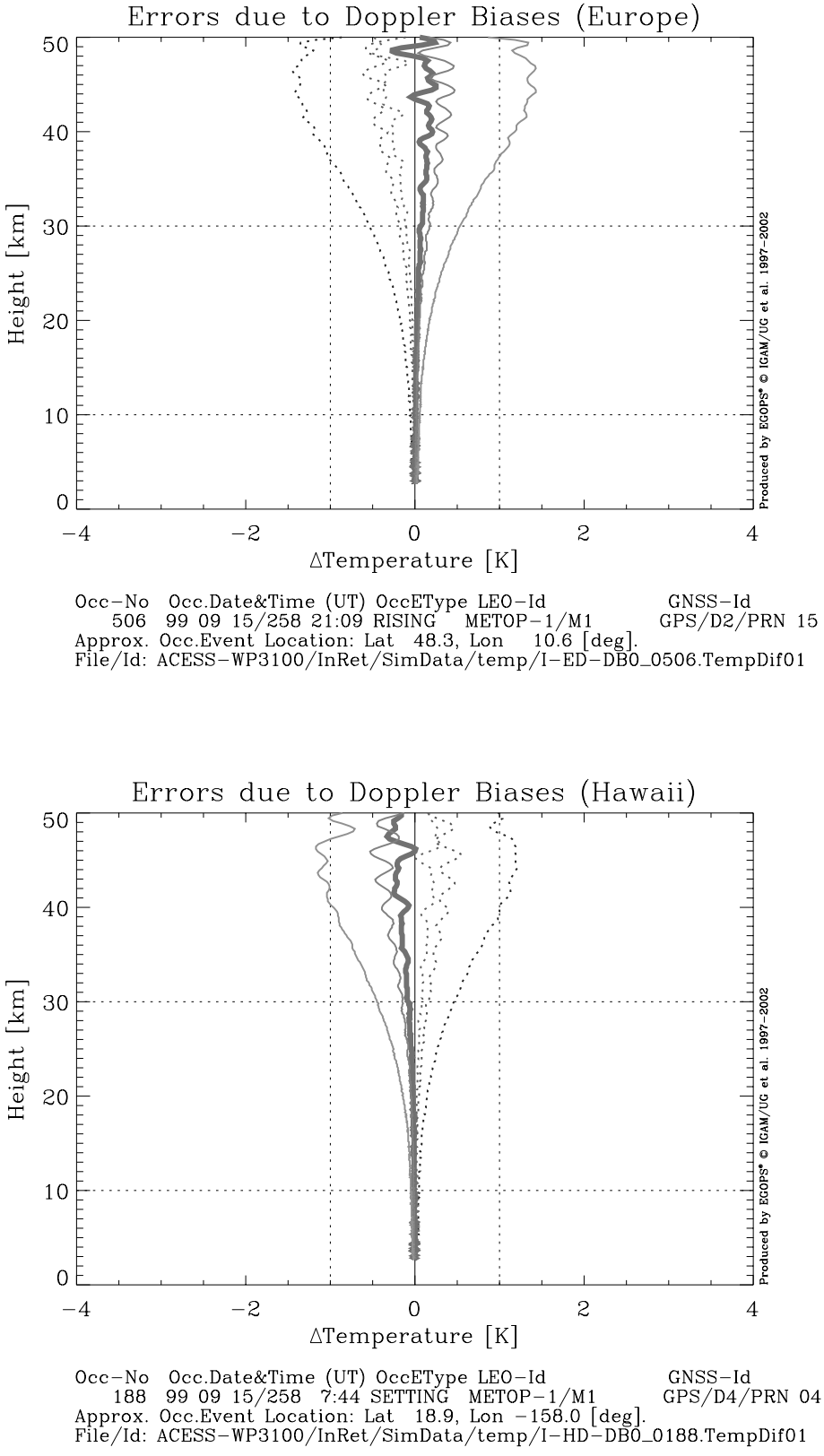

Figure 3.1.1: Temperature Errors due to Doppler Biases.

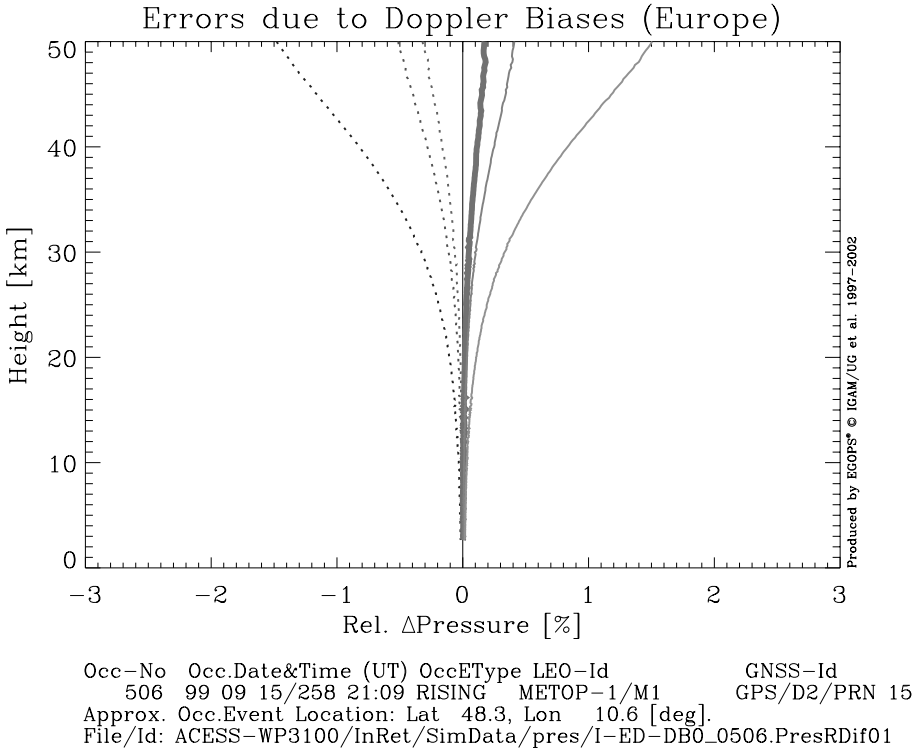

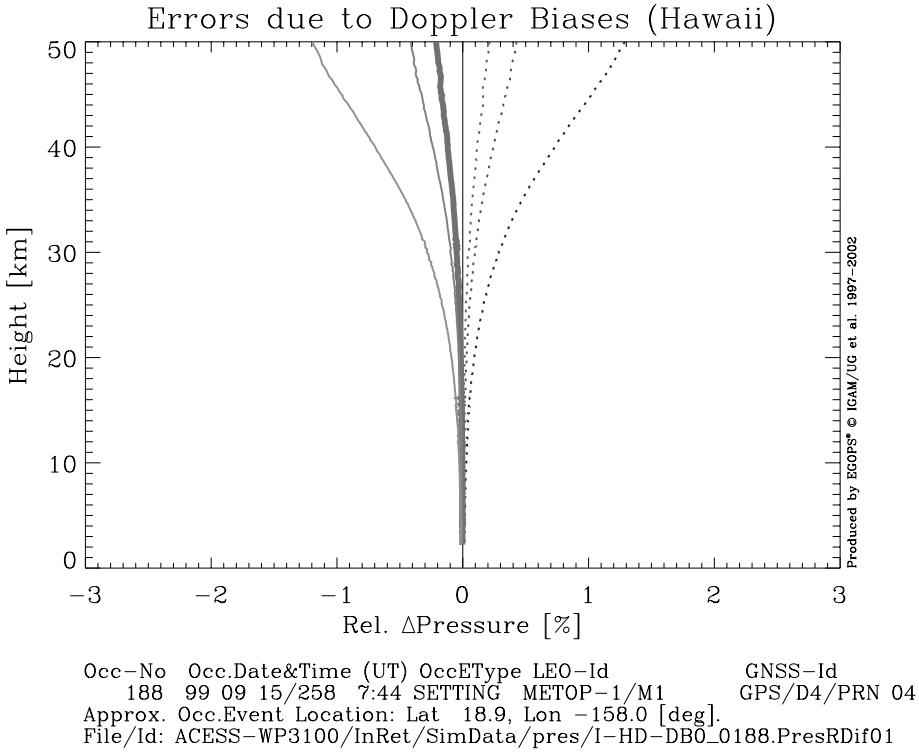

Figure 3.1.2: Pressure Errors due to Doppler Biases.

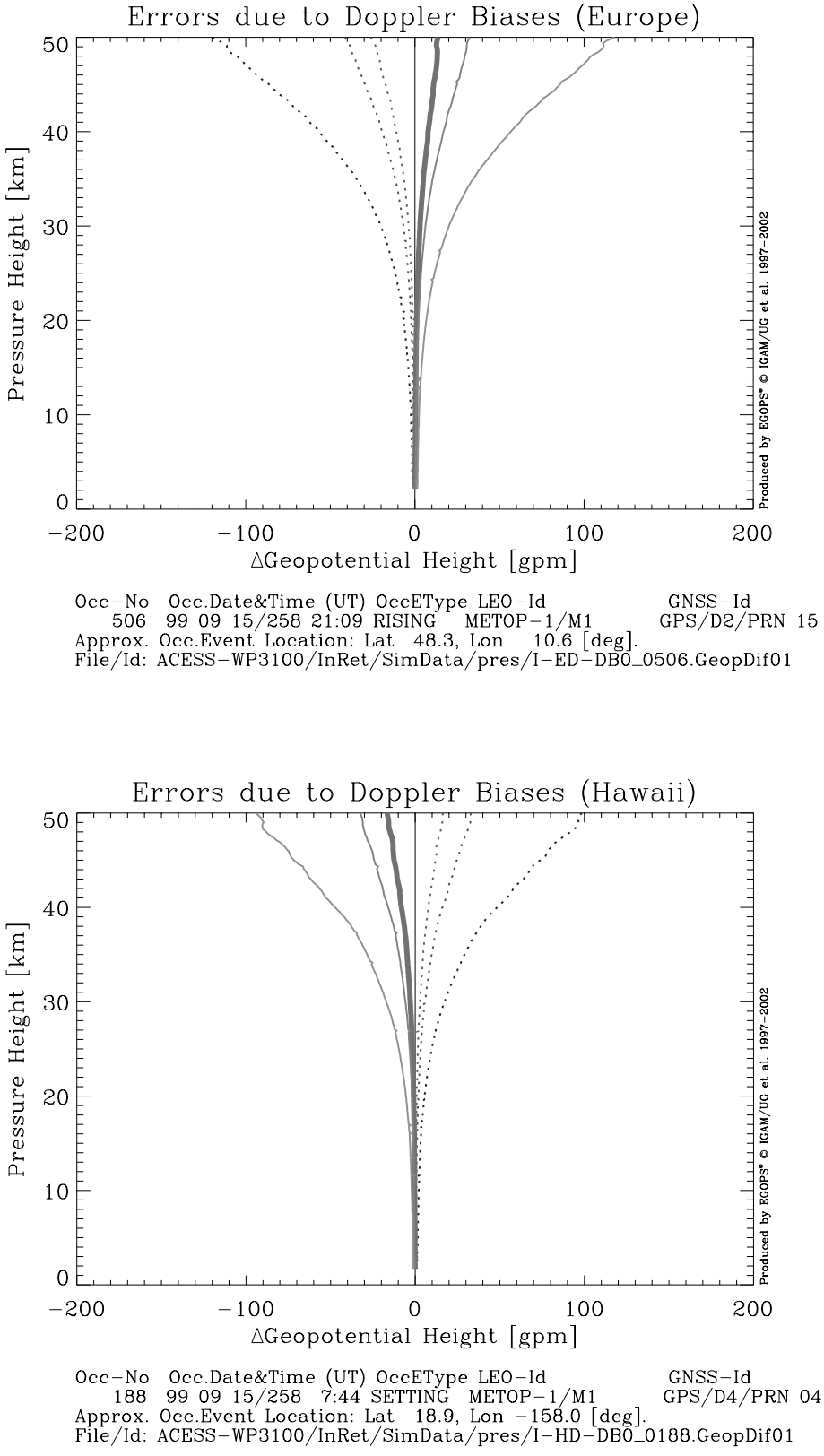

Figure 3.1.3: Geopotential Height Errors due to Doppler Biases.

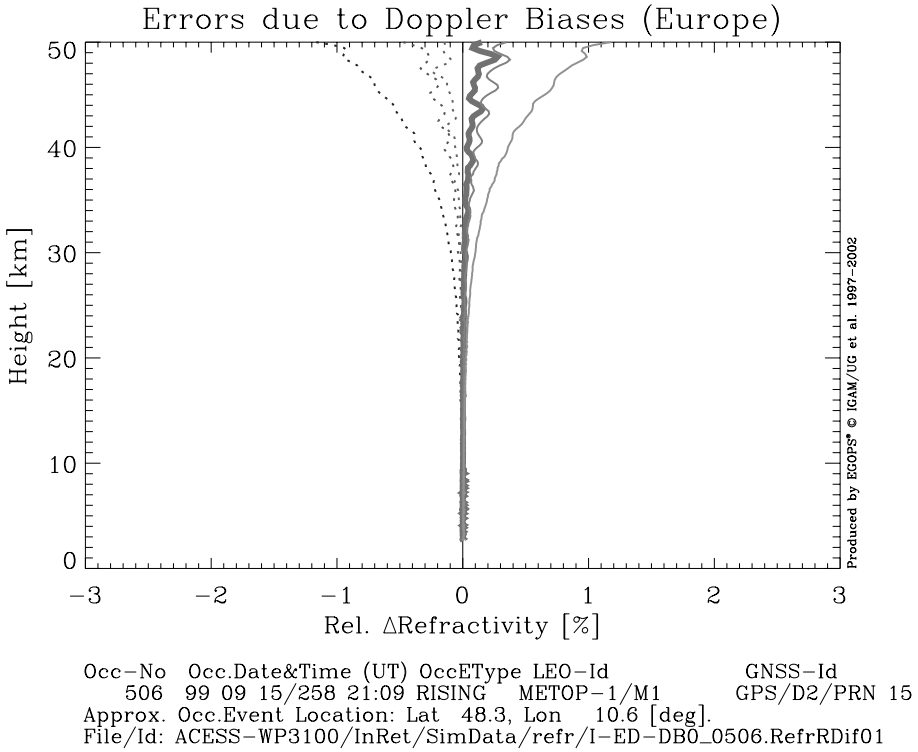

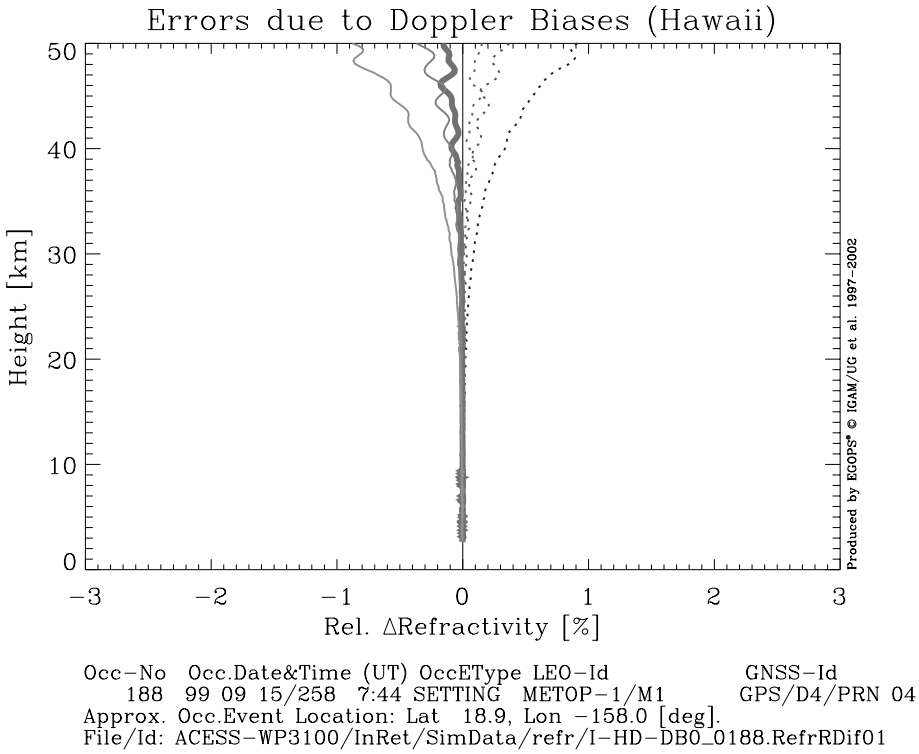

Figure 3.1.4: Refractivity Errors due to Doppler Biases.

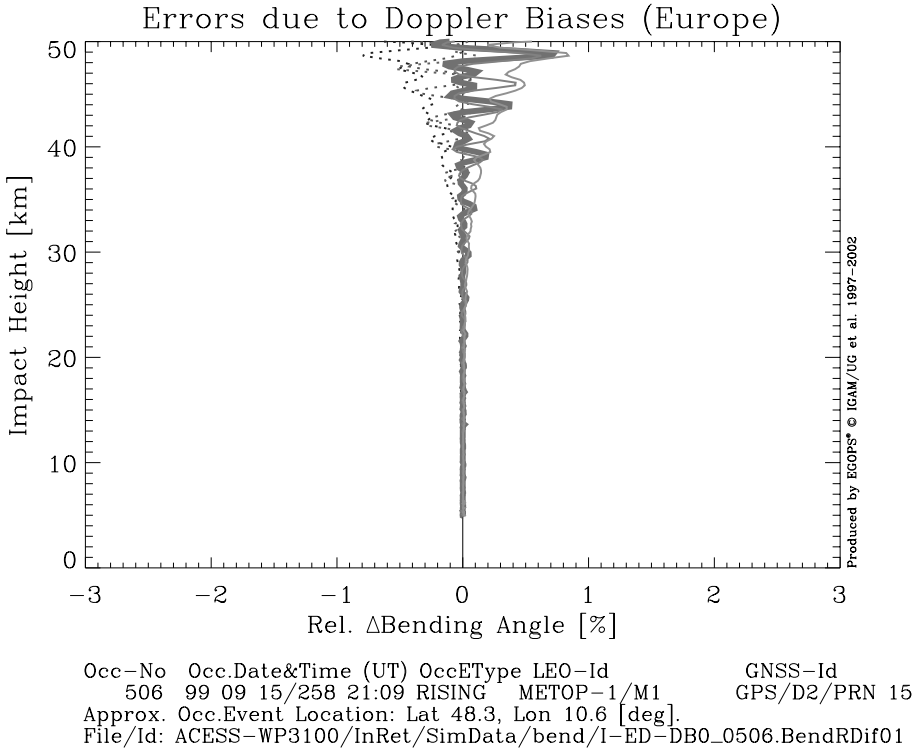

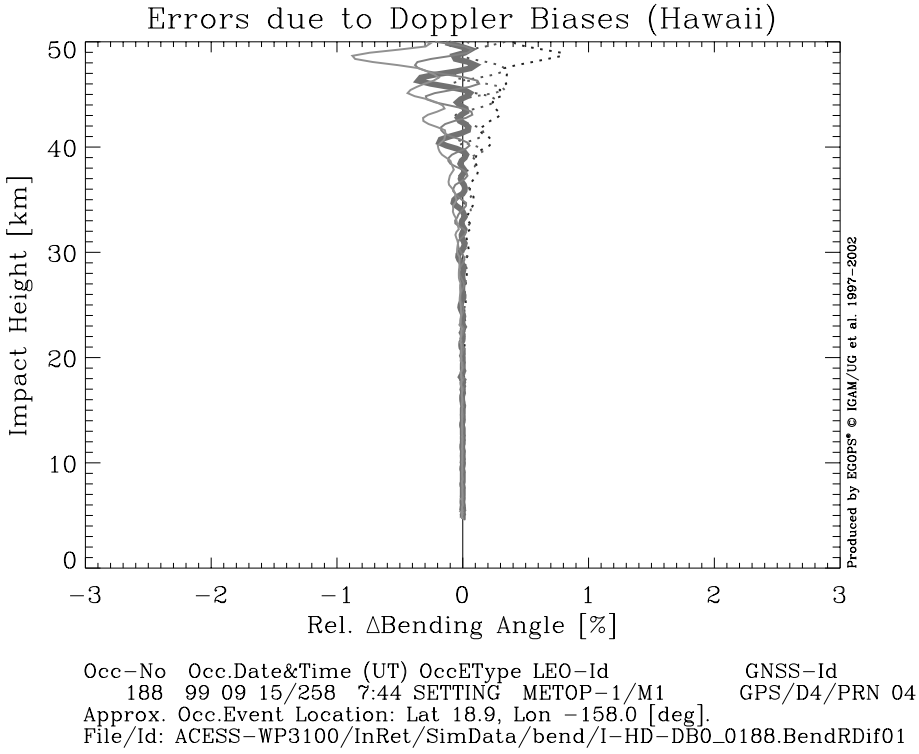

Figure 3.1.5: Bending Angle Errors due to Doppler Biases.

3.2. Doppler Drifts

In this second error scenario group we analyzed the sensitivity of retrieved profiles to errors introduced due to Doppler drifts. Section 2.3.1 above provided details on the error specifications used. Briefly recalled, the Doppler drift errors were simulated via variations of the POD along-ray acceleration error value, while all other OSMod input parameters were kept at their standard value. The seven acceleration error values explored were –0.3, –0.1, –0.05, 0, 0.05, 0.1, and 0.3 [μm/s²], respectively. The reference case, i.e., the "zero line" in the error plots, is 0 μm/s²; the GRAS-type standard case is 0.05 μm/s² (marked as heavy line in the error plots).

The results of the Doppler drift error calculations are displayed in Figures 3.2.1 to 3.2.5, in the order temperature, pressure, geopotential height, refractivity, and bending angle.

The temperature errors due to Doppler drifts are displayed in Figure 3.2.1. It is visible at a glance, that, in contrast to the errors due to Doppler biases, the temperatur errors due to Doppler drifts (of reasonable size as specified here) are much smaller. For both the "Europe" and the "Hawaii" event the temperature errors are found to be < 0.1 K in the lower stratosphere (up to ~35 km) and reach their maximum of ~0.5 K at 50 km height, at the same time showing increasingly oscillatory behavior at greater heights. Error magnitudes are at a sufficiently small level so that their is not much difference between the different scenarios. Overall, the temperature errors due to the Doppler drifts are practically negligible compared to the Doppler bias errors are rather shown in Figure 3.1.1 (the difference may be even more clearly expressed in reality, since the drift error magnitudes adopted here are relatively conservative).

In general the same picture is valid for the pressure, geopotential height, and refractivity errors due to Doppler drifts as well, which are displayed in Figures 3.2.2., 3.2.3, and 3.2.4, respectively. The pressure (geopotential height) errors are very small and smooth and < 0.1% (< 10 gpm) over the full altitude range. Similarly, the refractivity errors are very small, while showing more oscillatory behavior at greater heights.

The bending angle errors are, in terms of their oscillation peaks, markedly larger than the refractivity errors in the upper stratosphere. Up to an altitude of about 35 km the errors are confined to the < 0.1% range, but they grow to about 0.7% towards the stratopause.

The overall picture is that errors in retrieved atmospheric profiles due to Doppler drifts are negligible compared to errors due to Doppler biases; a result confirming the results reported by Kirchengast (1998b) based on more simplified simulations.

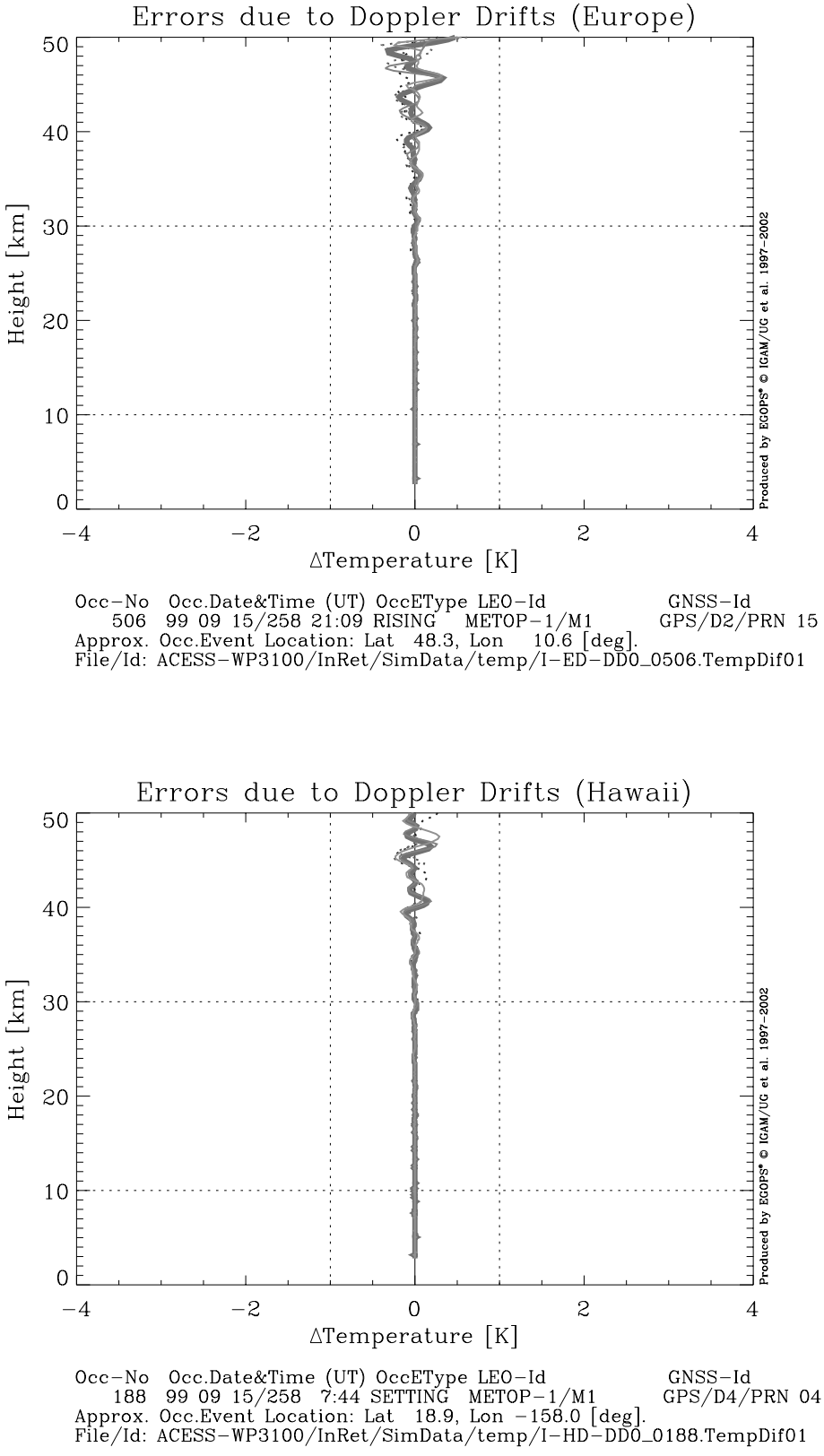

Figure 3.2.1: Temperature Errors due to Doppler Drifts.

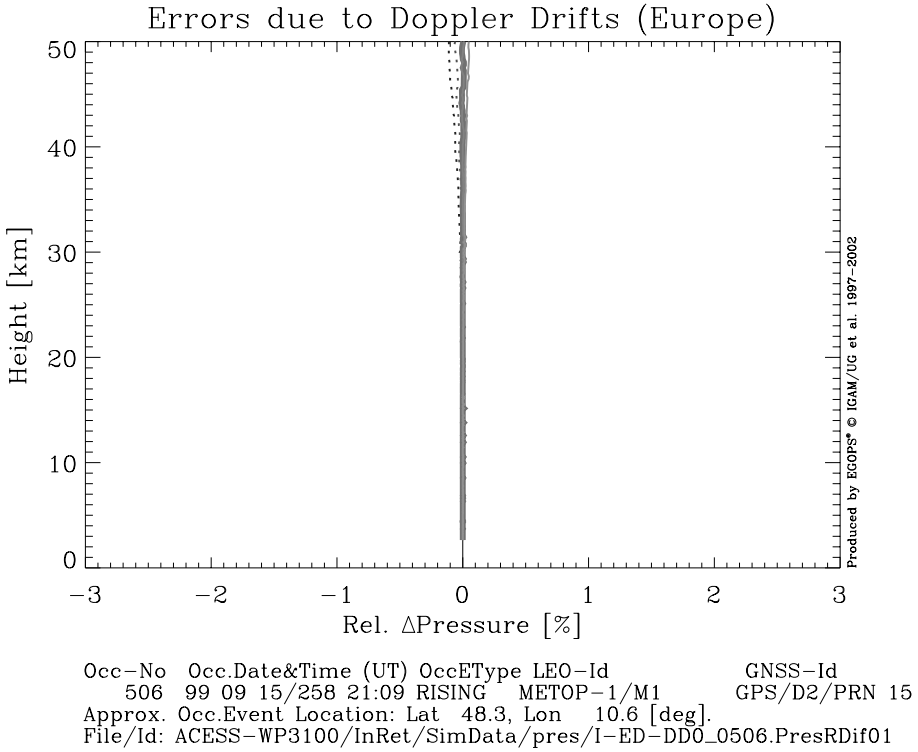

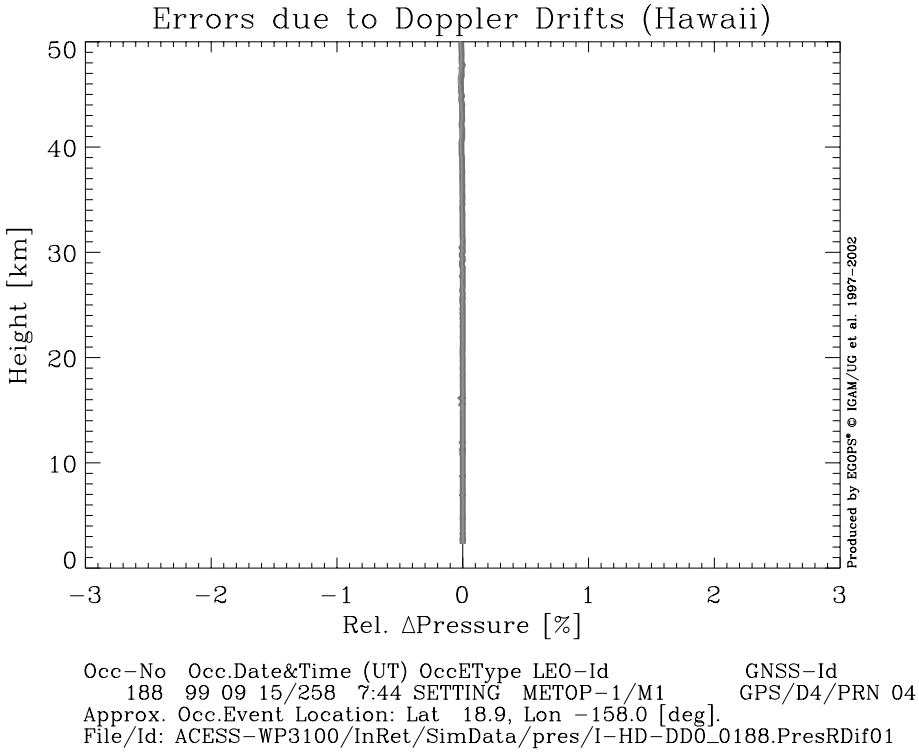

Figure 3.2.2: Pressure Errors due to Doppler Drifts.

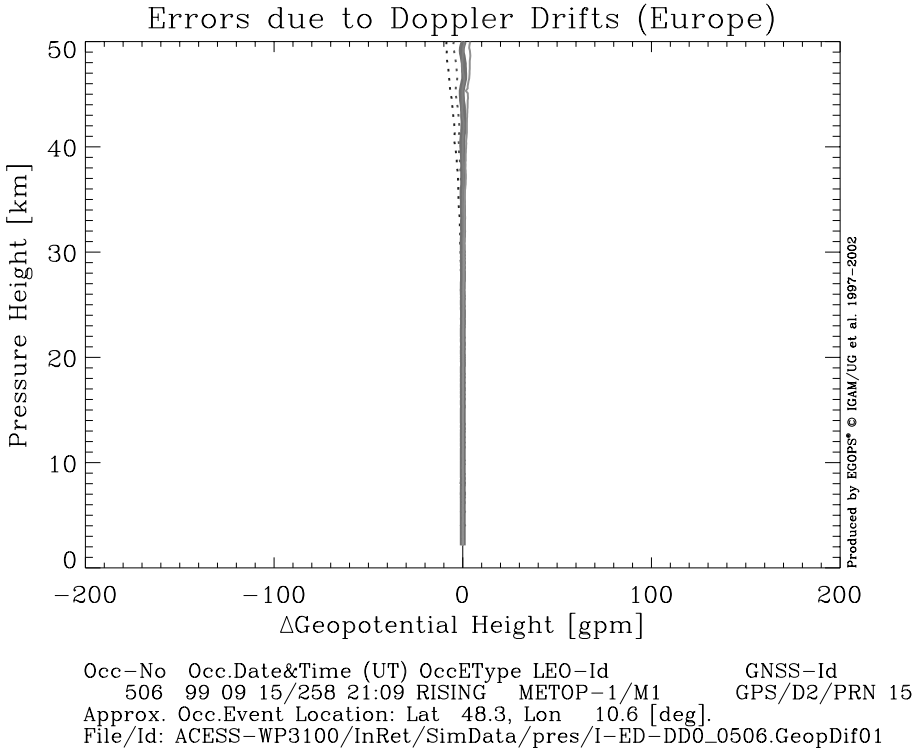

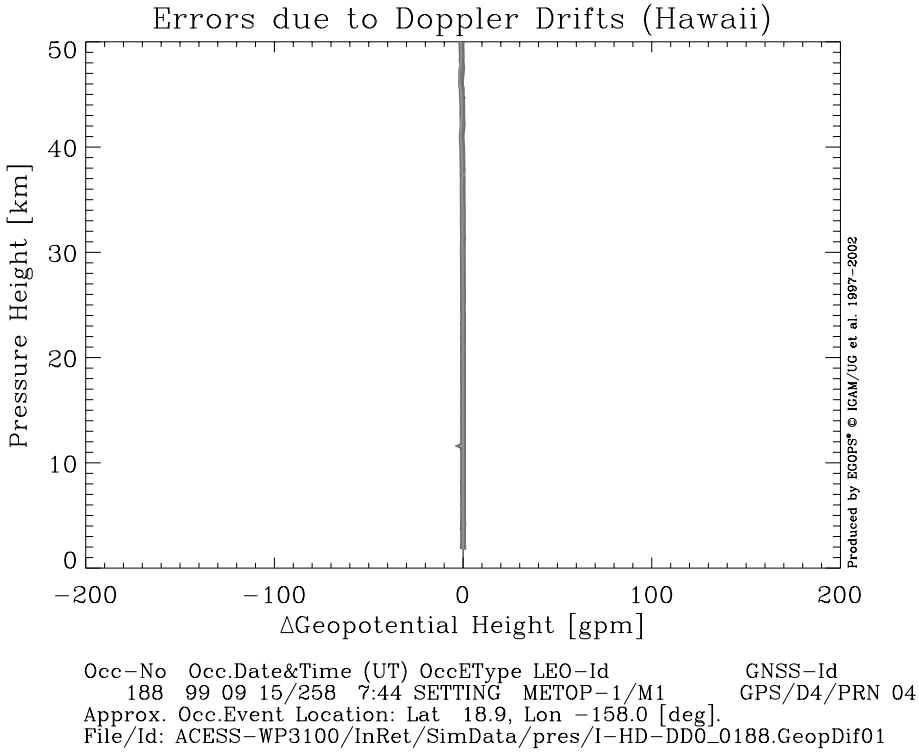

Figure 3.2.3: Geopotential Height Errors due to Doppler Drifts.

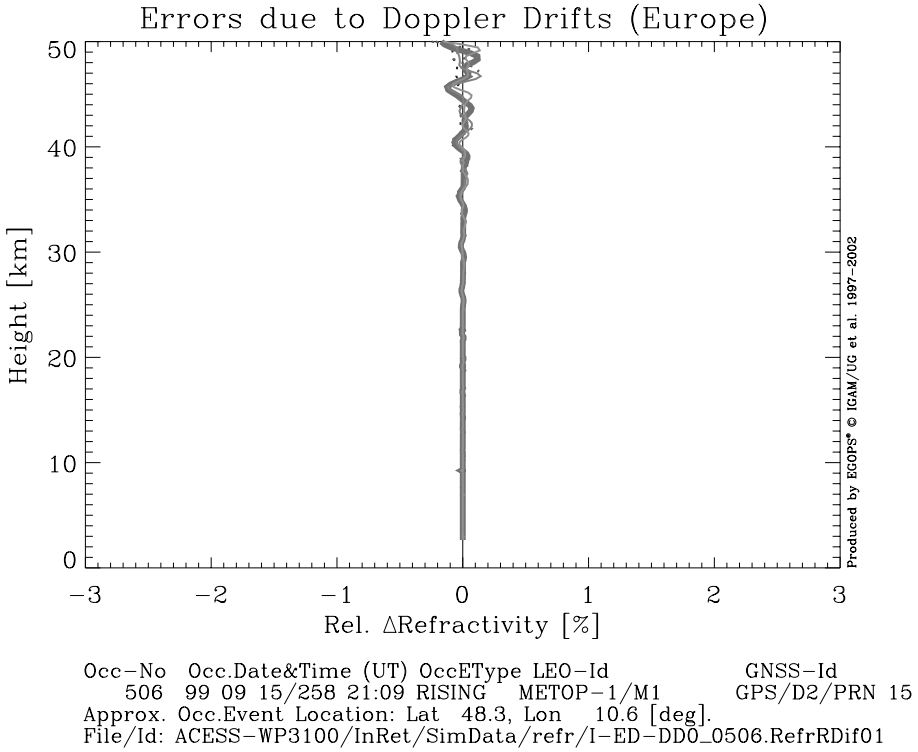

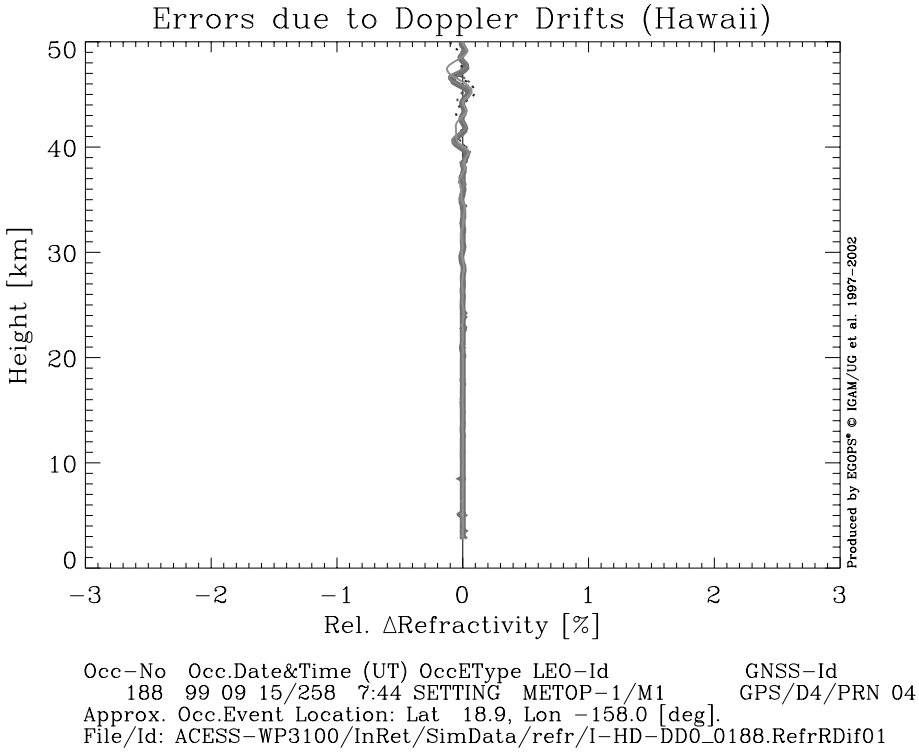

Figure 3.2.4: Refractivity Errors due to Doppler Drifts.

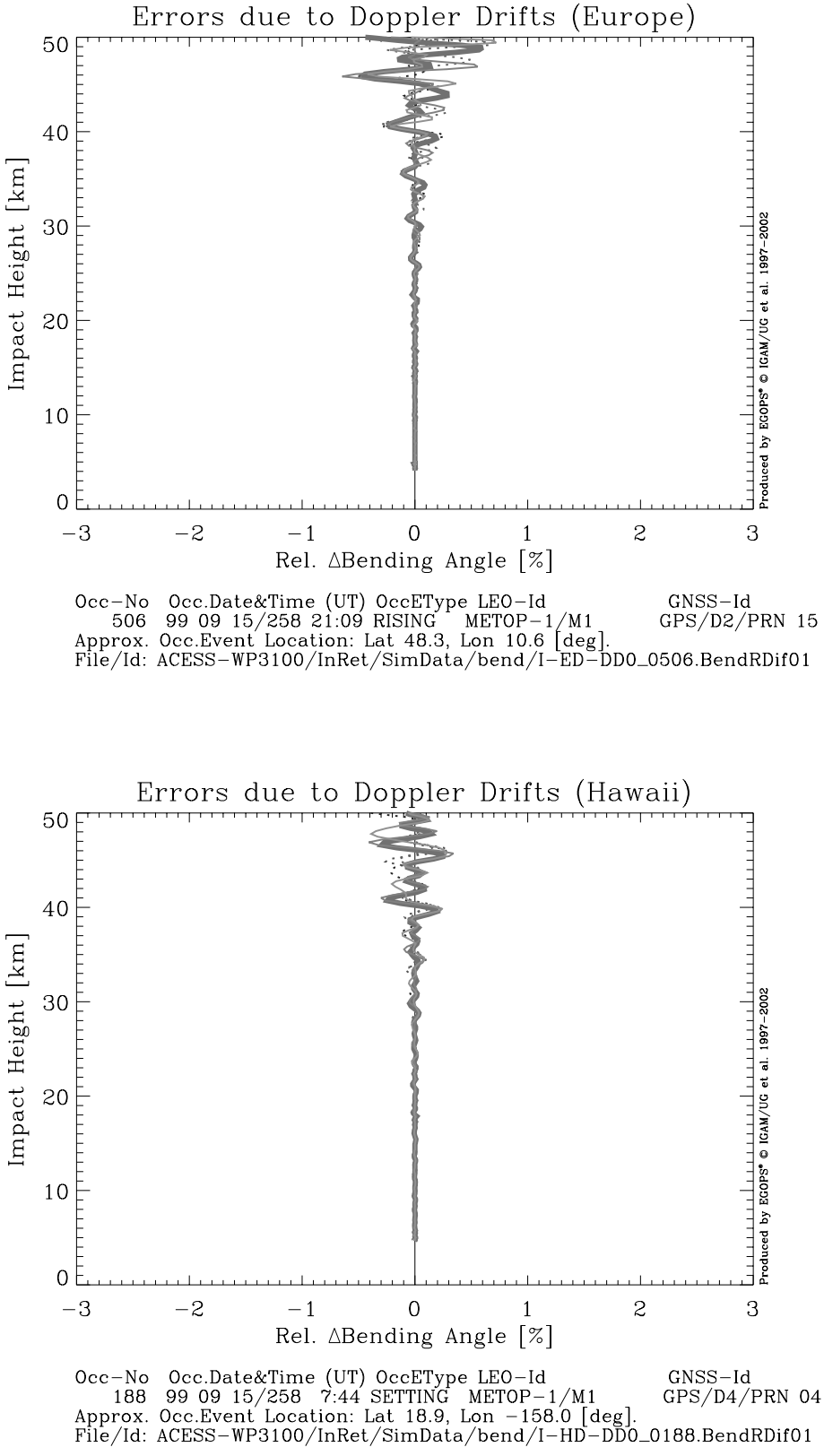

Figure 3.2.5: Bending Angle Errors due to Doppler Drifts.

3.3. Clock Stability/Single Differencing Errors

In this third error scenario group we analyzed the sensitivity of retrieved profiles to errors introduced due to clock stability/single-differencing errors. Section 2.3.2. above provided details on the error specifications used. Briefly recalled, the clock stability/single differencing errors were simulated via variations of the 1-sec Allan deviation value of the LEO clock, while all other OSMod input parameters were kept at their standard value. The four clock stability error values explored were 0, 1 x 10^{-13}, 3 x 10^{-13}, and 1 x 10^{-12} [1secAllan], respectively. The reference case, i.e., the "zero line" in the error plots, is 0 [1secAllan]; the GRAS-type standard case is represented by the 1 x 10^{-13} [1secAllan] setting (corresponding retrievals marked as heavy line in the error plots).

The results of the clock stability/single-differencing error calculations are displayed in Figures 3.3.1 to 3.3.5, in the order temperature, pressure, geopotential height, refractivity, and bending angle.

The temperature errors due to clock stability/single differencing errors are displayed in Figure 3.3.1. For both the "Europe" and "Hawaii" event the temperature errors are < 0.1 K up to 10 km height. In the lower stratosphere up to 30 km, the temperature error of the worst case scenario (1 x 10^{-12} 1secAllan) grows to about –1 K, further increasing to more than –3 K in the upper stratosphere. The two other cases with higher clock stability deliver significantly improved results; for the GRAS-type error case (heavy solid line), the temperature errors stay within 0.7 K even in the upper stratosphere. Interestingly, the temperature error of the worst case "Hawaii" event exhibits a significantly lower temperature error in the stratosphere than the one of the "Europe" event. This is presumably due to the different statistical optimization processes involving different background profiles for the two events and may partly be also due to differences in geometry (the events have different tangent point trajectories and event durations; the "Europe" event is more smearing, cf. Figures 2.2 and 2.3).

The pressure and geopotential height errors, Figures 3.3.2 and 3.3.3, behave much smoother than the corresponding temperature errrors. Up to about 10 km the pressure (geopotential height) errors are < 0.1% (< 8 gpm), but for higher altitudes they can grow to several %, e.g., reach –3 % for the "Europe" event at the stratopause (the corresponding geopotential height errors are exceeding –200 gpm). However, the GRAS-type error case (heavy solid line) leads to < 0.3% pressure error (< 25 gpm geopotential height error) also in the upper stratosphere.

The refractivity and bending angle errors, Figures 3.3.4 and 3.3.5, are < 0.1% up to about 25 km and then, with increasing height, grow to similar (just somewhat smaller) magnitudes as the pressure errors. As seen before in the temperature error result plots, the bending angle errors are more oscillating than those in refractivity.

The overall picture is that errors in retrieved atmospheric profiles due to clock stability/single-differencing errors are, roughly speaking, of similar importance in the total observation system-related error budget as the errors due to Doppler biases disussed in section 3.1.

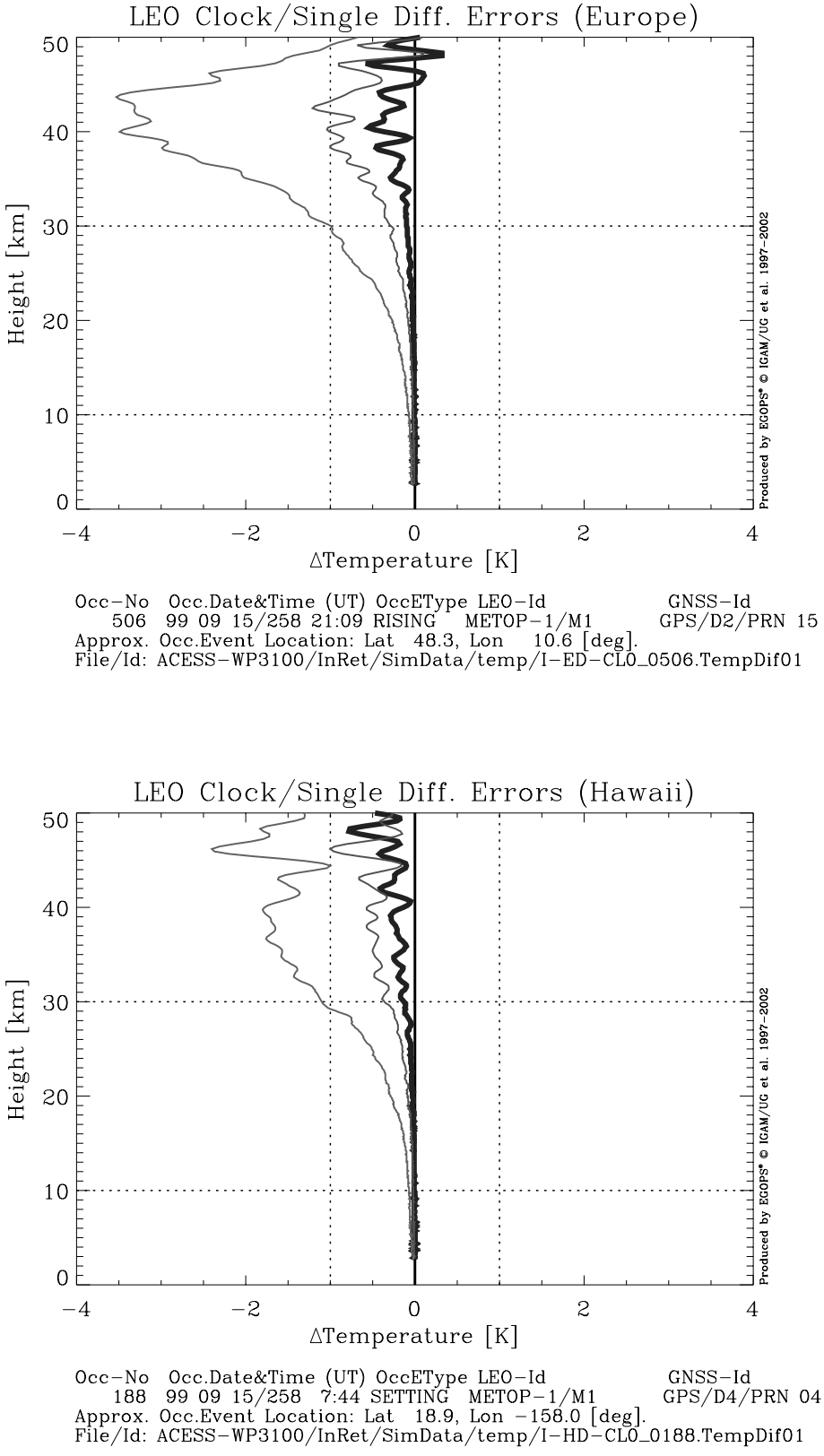

Figure 3.3.1: Temperature Errors due to LEO Clock/Single-Differencing Errors.

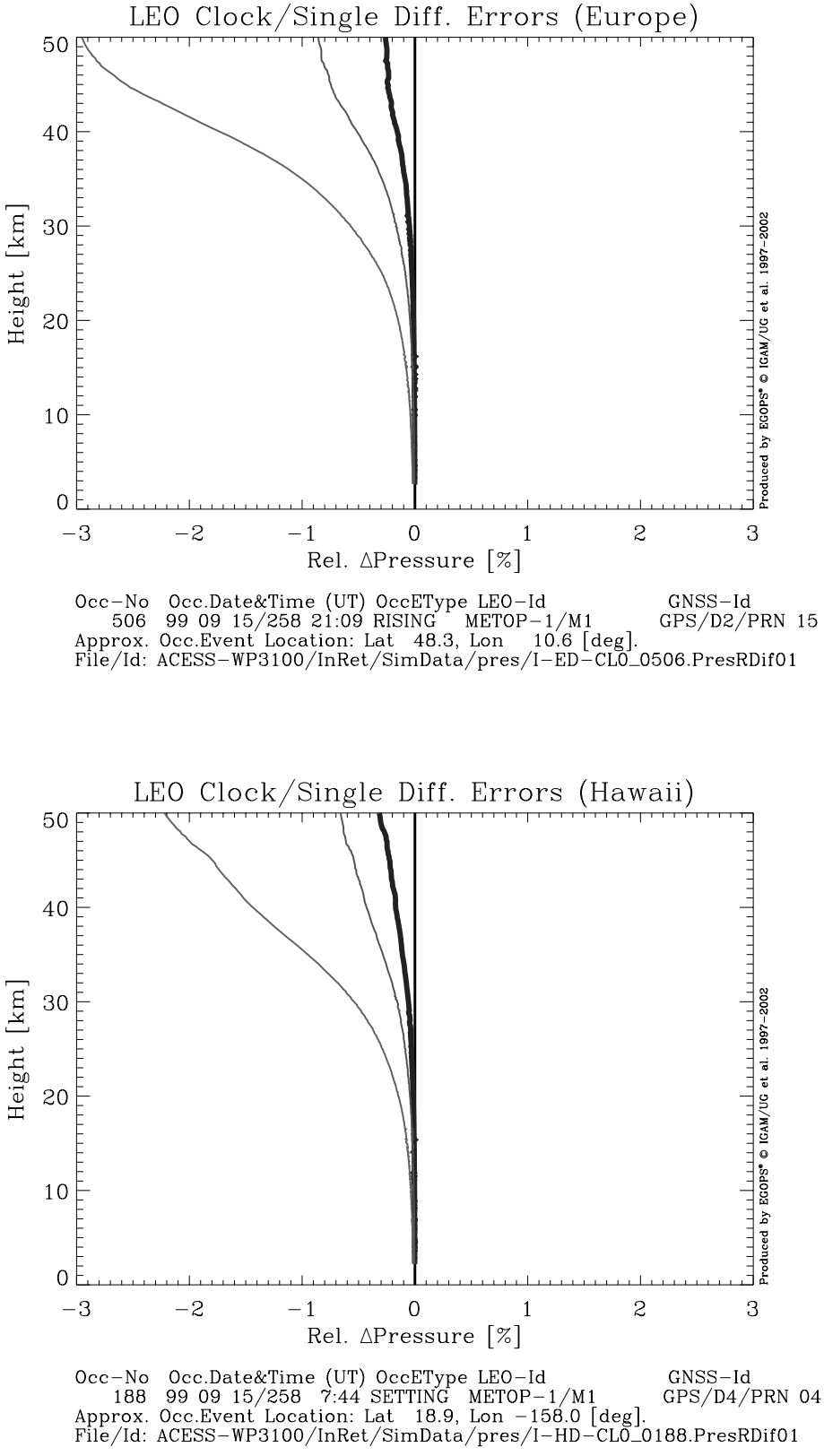

Figure 3.3.2: Pressure Errors due to LEO Clock/Single-Differencing Errors.

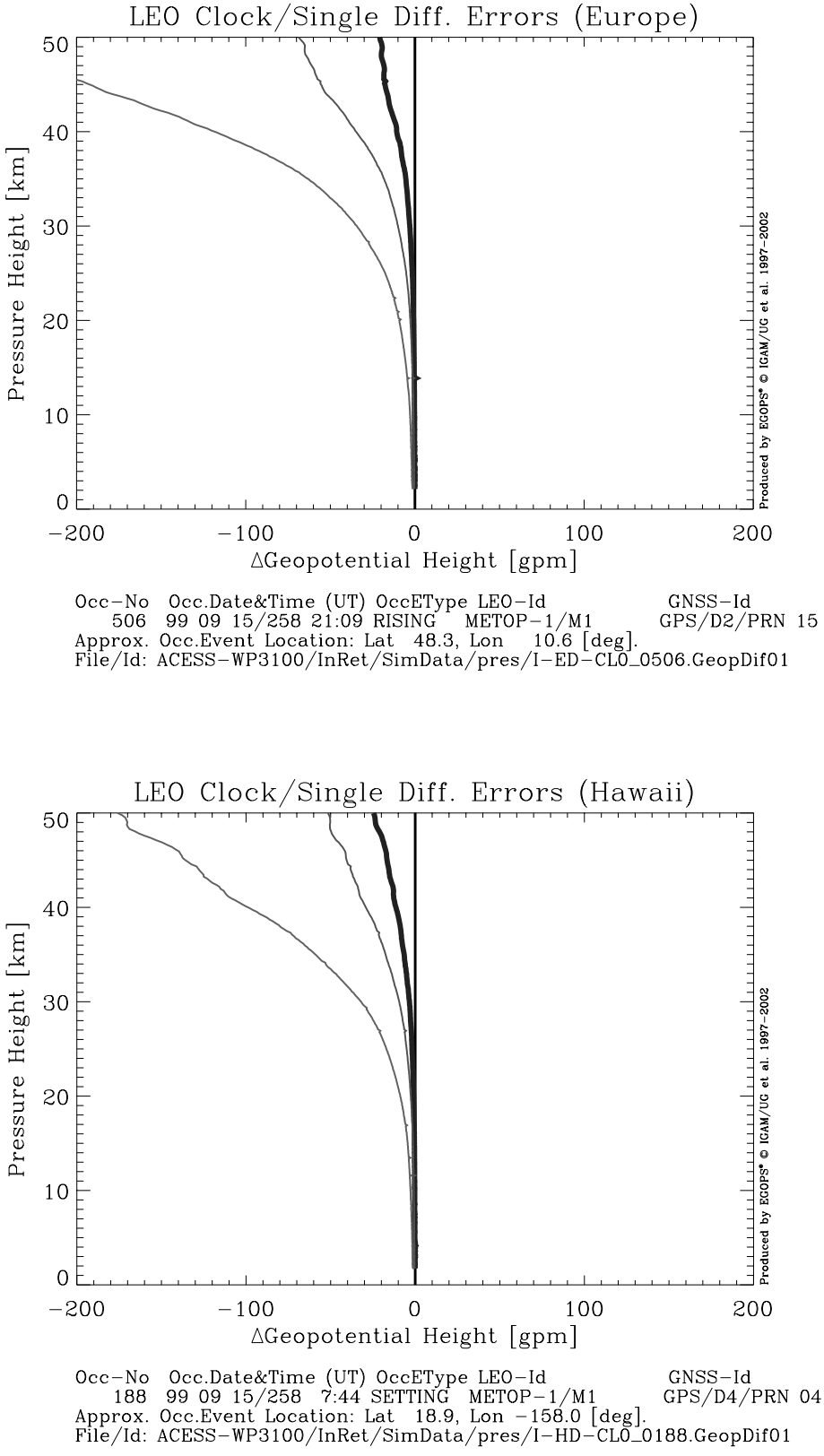

Figure 3.3.3: Geopotential Height Errors due to LEO Clock/Single-Differencing Errors.

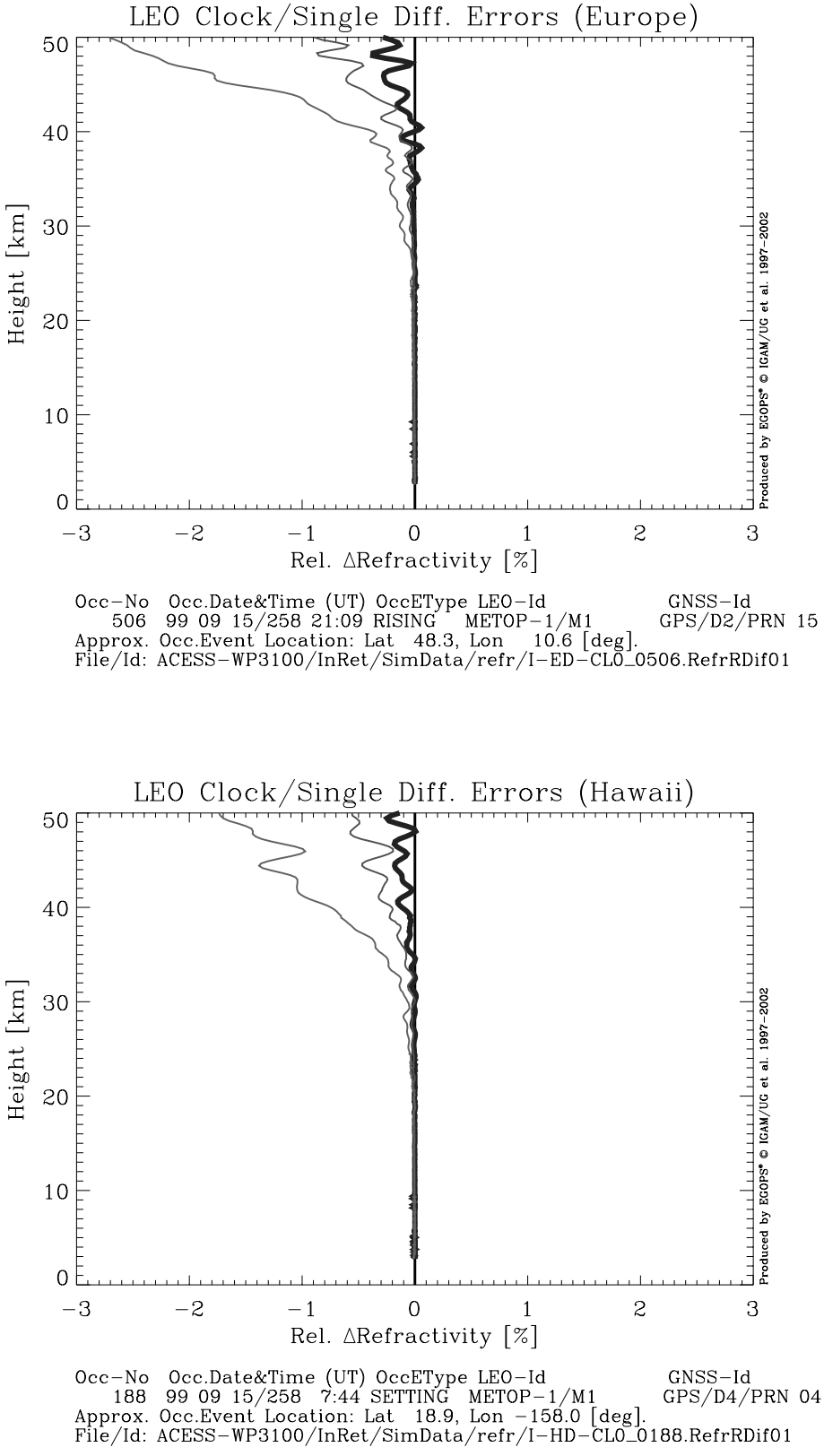

Figure 3.3.4: Refractivity Errors due to LEO Clock/Single-Differencing Errors.

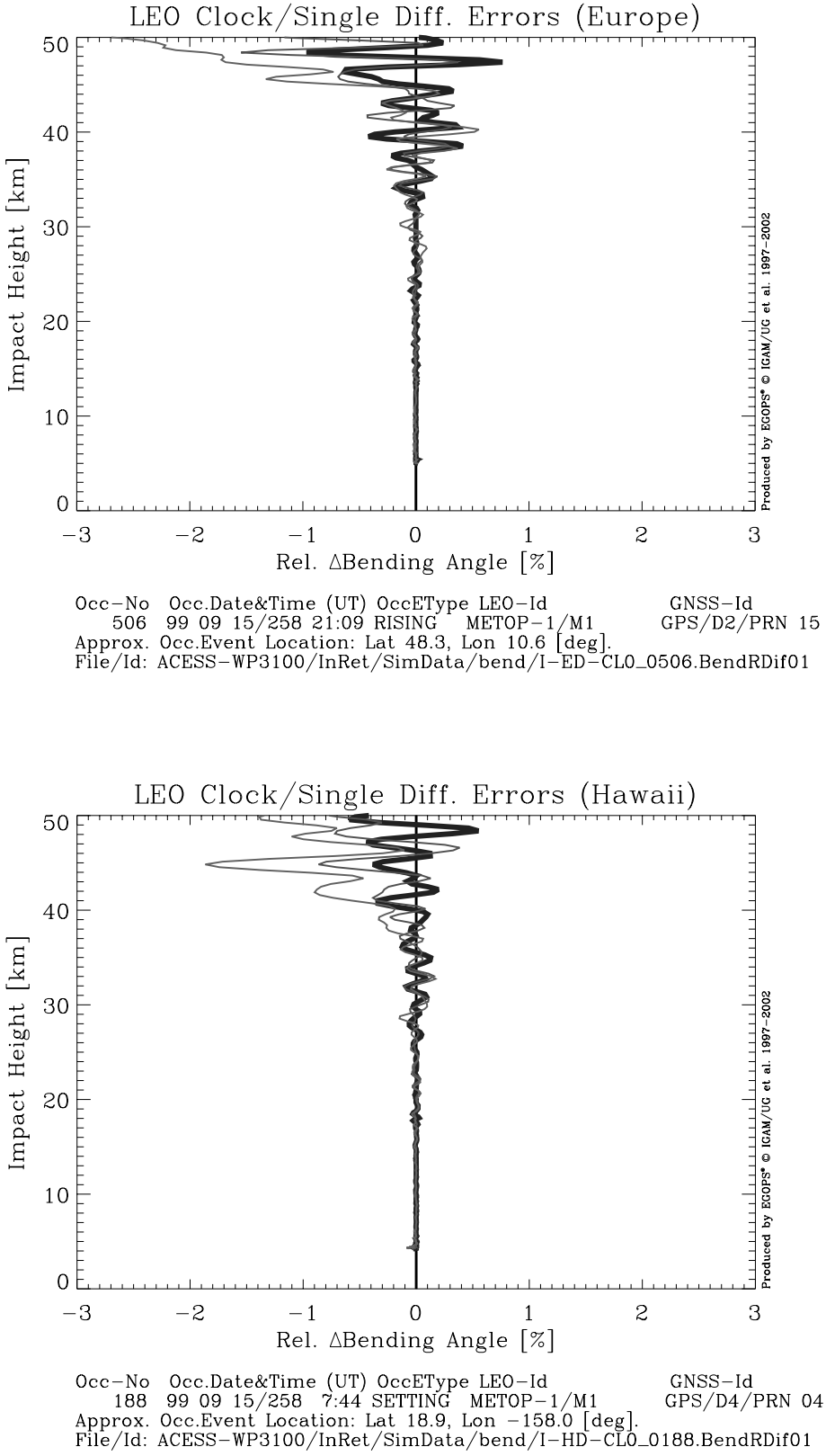

Figure 3.3.5: Bending Angle Errors due to LEO Clock/Single-Differencing Errors.

3.4. Realistic Receiver Noise Model Errors

In this fourth error scenario group we analyzed the sensitivity of retrieved profiles to errors introduced by receiver thermal noise. Section 2.3.3 above provided details on the error specifications used. Briefly recalled, the receiver noise errors were simulated via joint variations of the antenna noise temperature and loop bandwidth values, while all other OSMod input parameters were kept at their standard value. The four antenna noise temperature/loop bandwidth value pairs explored were 0 (=no receiver noise), 150|10, 150|/25, and 250|25 [K|Hz], respectively. The reference case, i.e., the "zero line" in the error plots, is 0 (no receiver noise); the GRAS-type standard case is 150|10 [K|Hz] (marked as heavy line in the error plots).

The results of the receiver noise model error calculations are displayed in Figures 3.4.1 to 3.4.5, in the order temperature, pressure, geopotential height, refractivity, and bending angle.

The receiver noise temperature error results, Figure 3.4.1, show for both the "Europe" and "Hawaiii" event that the temperature errors are < 0.5 K up to about 35 km and reach oscillation peaks of about 4 K in the upper stratosphrere (above 50 km the maximum errors start to exceed 5 K). The GRAS-type error case (heavy solid line) exhibits errors of < 1 K up to about 40 km; beyond errors also start to extend to about 4 K near the stratopause.

The pressure and geopotential height errors, Figures 3.4.2 and 3.4.3, are fairly small, < 0.1% and < 8 gpm below 30 to 35 km. Even in the upper stratosphere the errors stay within about 0.5 % (pressure) and 40 gpm (geopotential height). This clearly highlights the important role of smoothing for this type of high-frequency error source. In other words, also temperature errors in the upper stratosphere could be further decreased by smoothing, at the expense of somewhat less resolution.

The refractivity errors, Figure 3.4.4, also are relatively small up to about 30 km (< 0.1%), higher up they significantly increase to values of up to around ±2–3% near stratopause.

The bending angle errors, Figure 3.4.5, being less smoothed among all retrieval products, best exhibit the nature of the effects of high-frequency noise in high-resolution (order 100 meters) data: Oscillations stay within 0.1% bounds below 15 km, but reach up to ~0.5% already in the lower stratosphere, and start to exceed 3% levels above 40 km. Smoothing to a resolution near 1 km would of course significantly mitigate such noise.

The overall picture is that errors in retrieved atmospheric profiles due to thermal receiver noise are the major contributor of high-frequency noise in retrieval products. Receiver noise is thus an important component in the observation system-related error budget of a GRAS-type receiver. The present results, where the GRAS-type thermal noise has been modeled conservatively, confirm that a careful receiving system design towards low system noise temperature (reflected here by low antenna noise temperature and limited bandwidth), and consequently low thermal noise, is capable to keep these errors acceptably small.

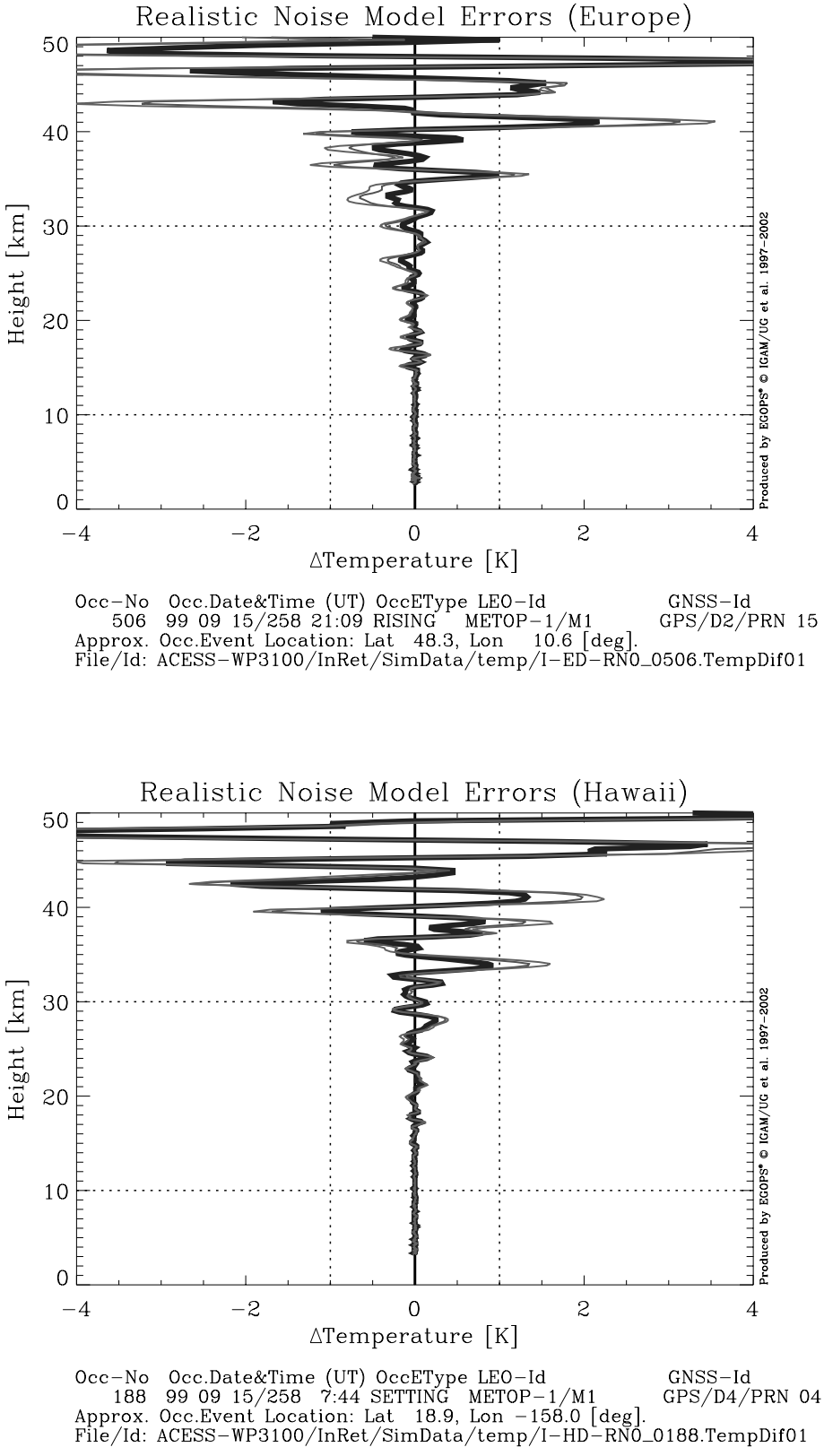

Figure 3.4.1: Temperature Errors due to Realistic Noise Model Errors.

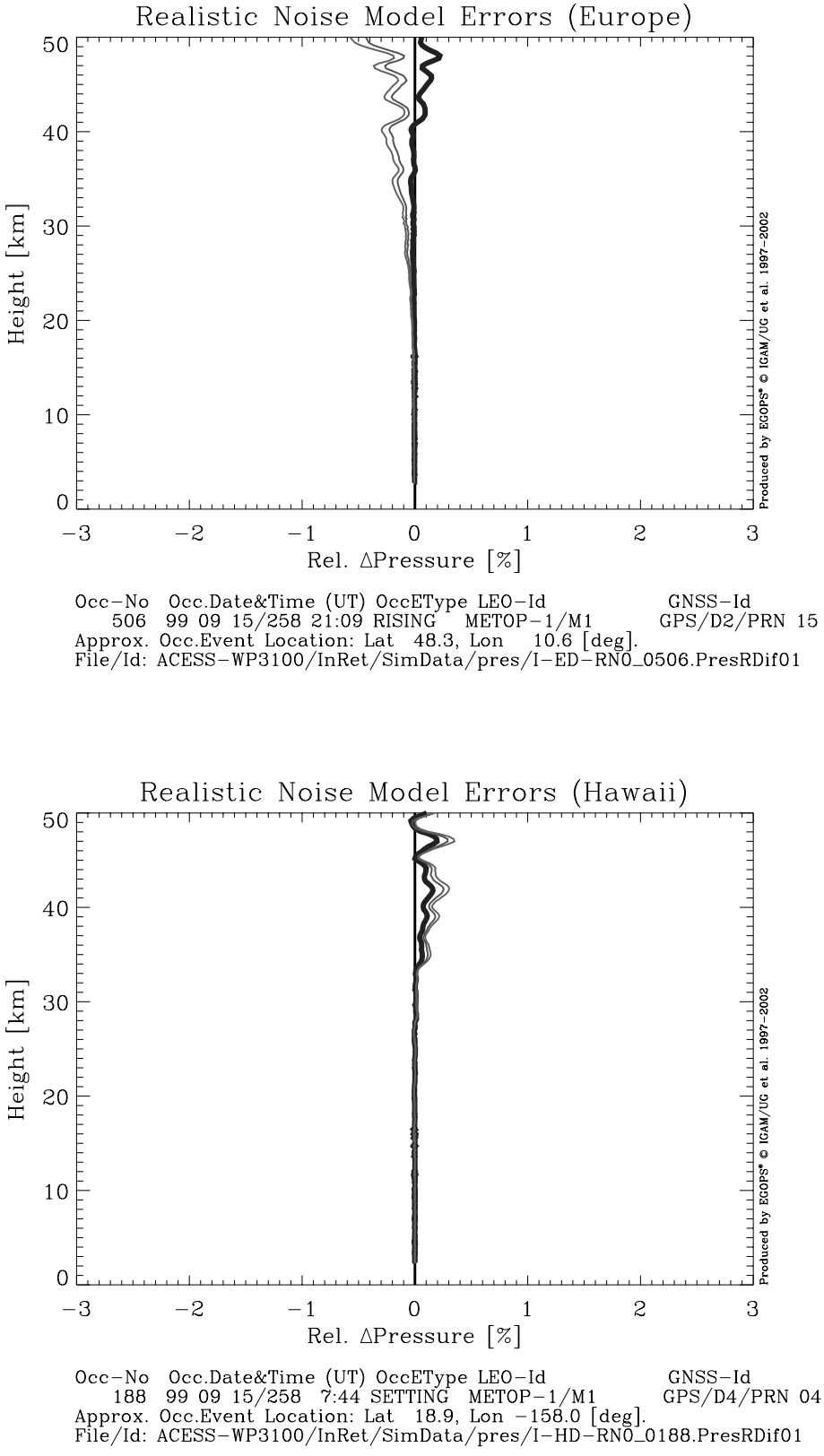

Figure 3.4.2: Pressure Errors due to Realistic Noise Model Errors.

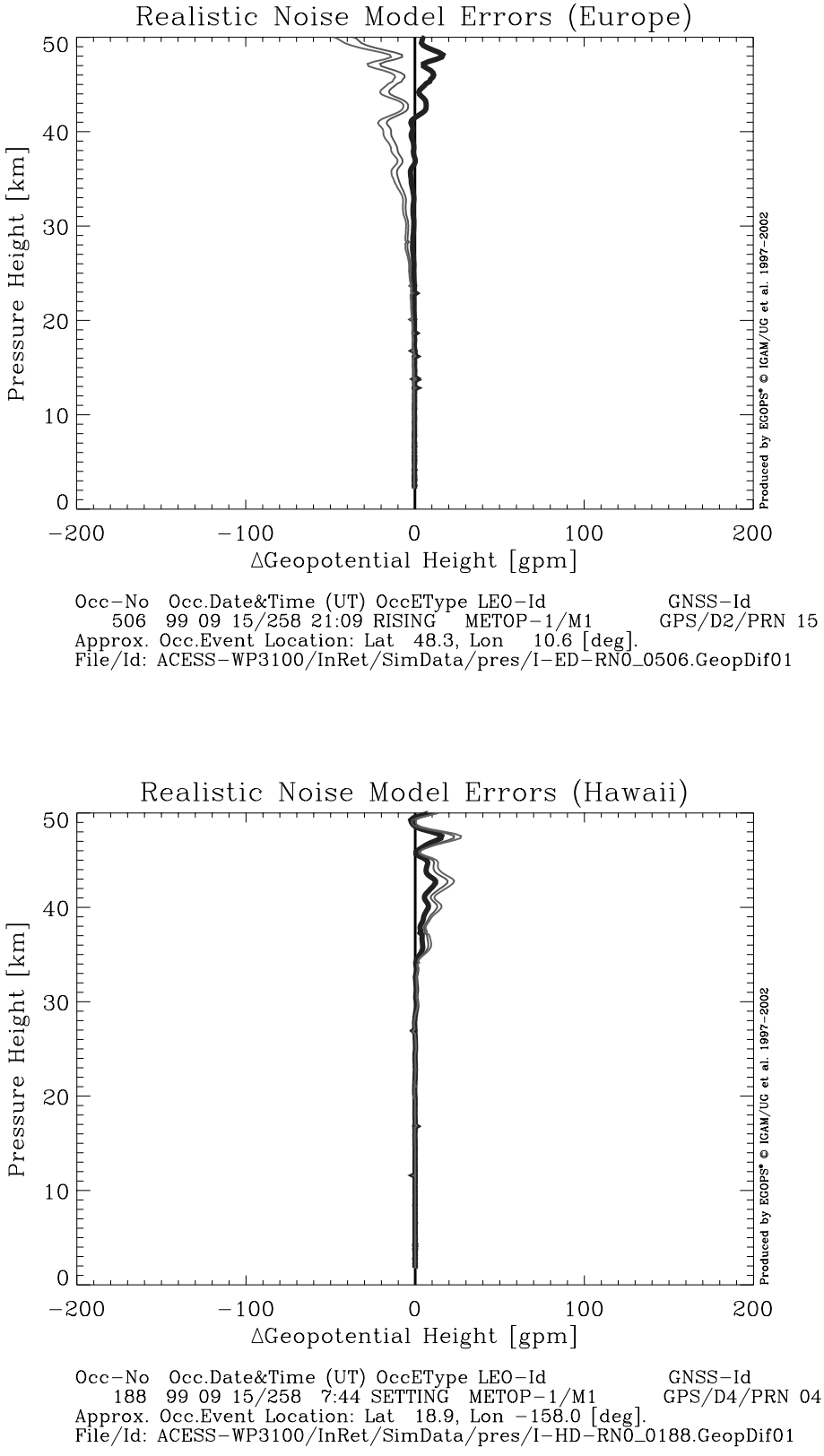

Figure 3.4.3: Geopotential Height Errors due to Realistic Noise Model Errors.

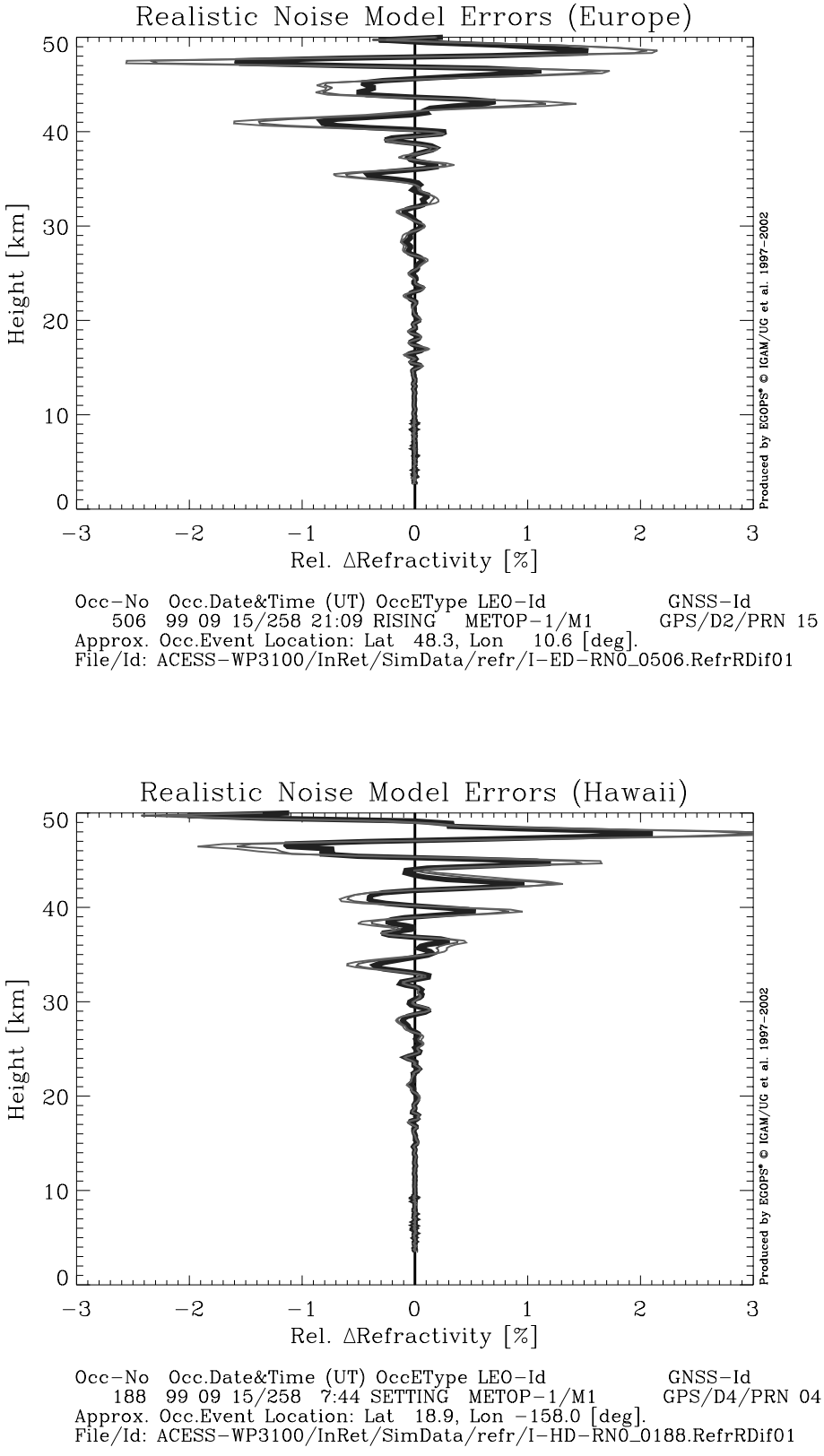

Figure 3.4.4: Refractivity Errors due to Realistic Noise Model Errors.

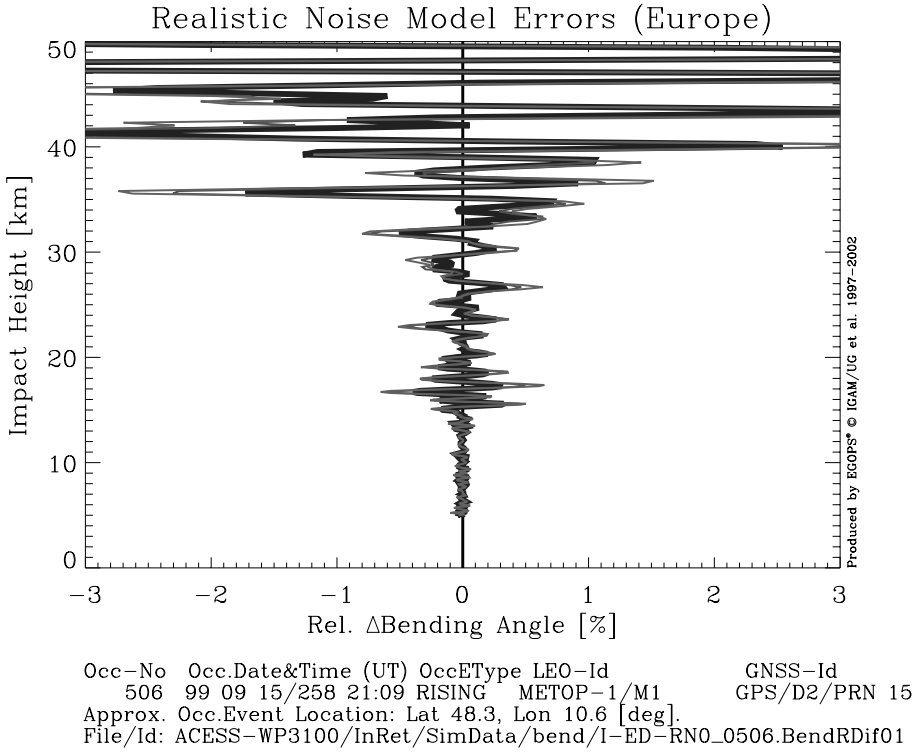

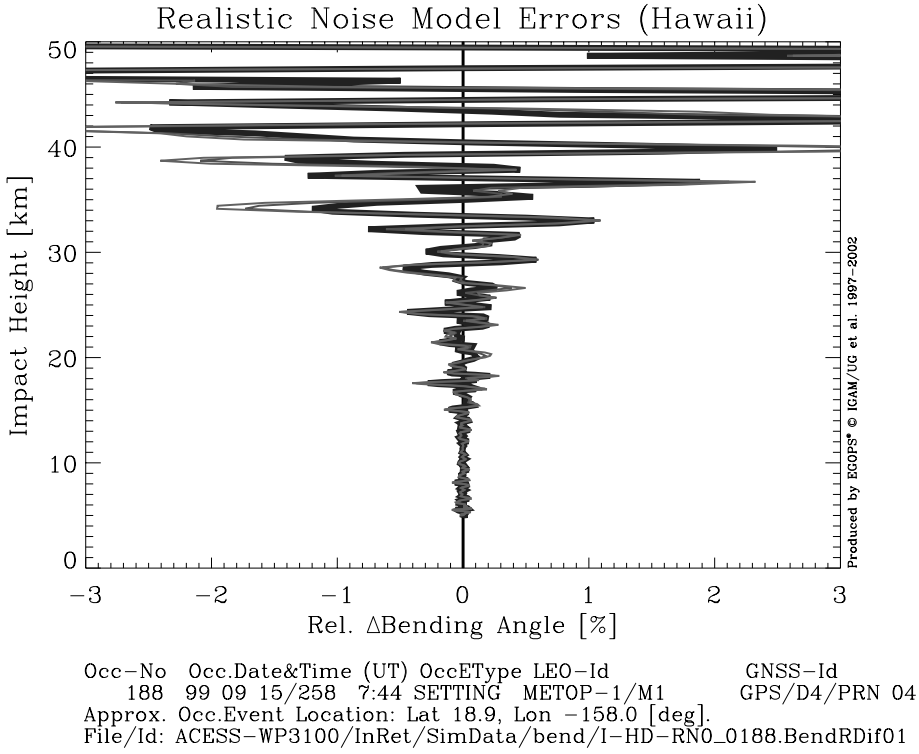

Figure 3.4.5: Bending Angle Errors due to Realistic Noise Model Errors.

3.5. Local Multipath Errors/Period and Amplitude Dependence

In this fifth error scenario group we analyzed the sensitivity of retrieved profiles to errors introduced by local multipath with different period/amplitude combinations. Section 2.3.4 provided details on the error specifications used. Briefly recalled, the local multipath errors with focus on period and amplitude dependence were simulated via joint variations of the period and amplitude values of a simple sinusoidal multipath model, while all other OSMod input parameters were kept at their standard value. The four period/amplitude value pairs explored were 0 (=no local multipath), 300|1, 100|1, and 100|2 [sec|mm], respectively. The reference case, i.e., the "zero line" in the error plots, is 0 (no local multipath); the GRAS-type standard case is 300|1 [sec|mm] (marked as heavy line in the error plots).

The results of these local multipath error calculations are displayed in Figures 3.5.1 to 3.5.5, in the order temperature, pressure, geopotential height, refractivity, and bending angle.

The temperature error results, Figure 3.5.1, show that up to 30 km the multipath induced errors are small (< 0.2 K), in the upper stratosphere they increase and can reach values of about 1 K close to the stratospause. For the GRAS-type error case (heavy solid line), the temperature errors stay within 0.3 K up to the stratopause for both events.

The pressure and geopotential height errors, Figures 3.5.2 and 3.5.3, are small in the lower stratosphere (< 0.1% and 8 gpm, respectively), throughout the upper stratosphere they to grow to about 0.75% for pressure and 60 gpm for geopotential.GRAS-type errors stay within 0.2% (pressure) and 15 gpm (geopotential height) up to the stratopause. Small residual kinks are also visible, not entirely smoothed out by the hydrostatic integration over refractivity.

The refractivity errors, Figure 3.5.4, exhibit an overall structure similar to the temperature errors (Figure 3.5.1). The errors are very small in the lower stratosphere (< 0.1% below 35 km) and stay mostly within 0.5% in the upper stratosphere, where they exhibit increasingly oscillating behavior.

The overall structure of the bending angle errors, Figure 3.5.5, are somewhat similar to the refractivity errors (Figure 3.5.4), but the average error/oscillation amplitudes are about two to three times larger in the upper stratosphere, due to the small amount of smoothing involved. The maximum oscillation peaks can reach near 1% in the upper stratosphere, for both the "Hawaii" and the "Europe" event.

The overall picture is that errors in retrieved atmospheric profiles due to local multipath errors with different period/amplitude combinations as explored are of significantly smaller magnitude than comparable low-frequency errors due to Doppler biases or clock residual errors. Nevertheless, it is clear from the results that it is important to ensure a low multipath environment for any GNSS occultation receiver, in order to keep actual multipath influence at or below the level reflected by the GRAS-type standard case in this study.

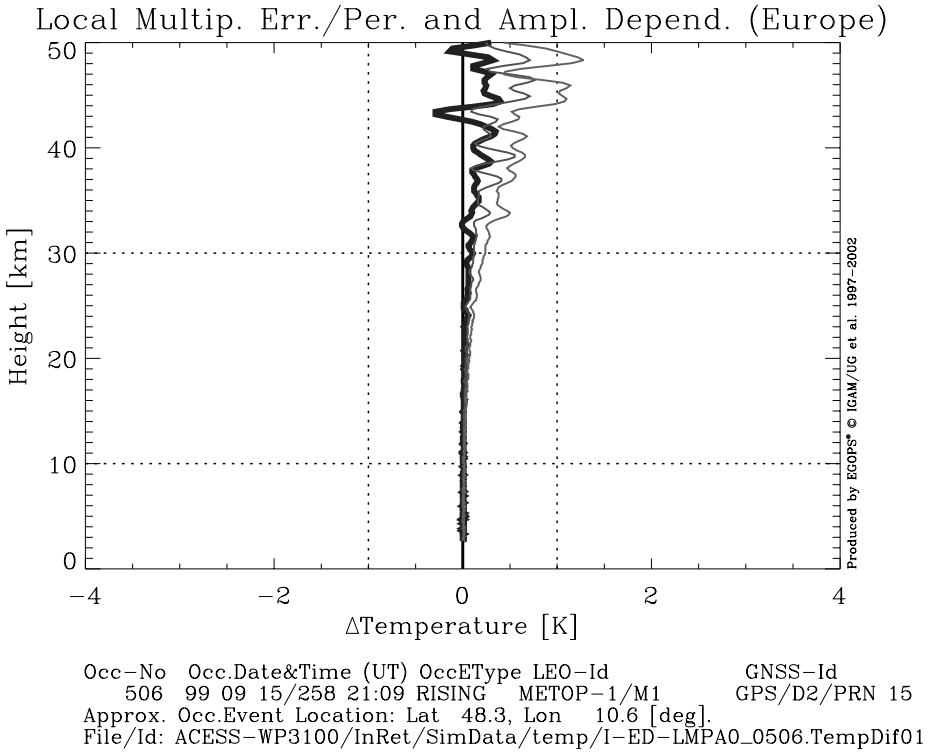

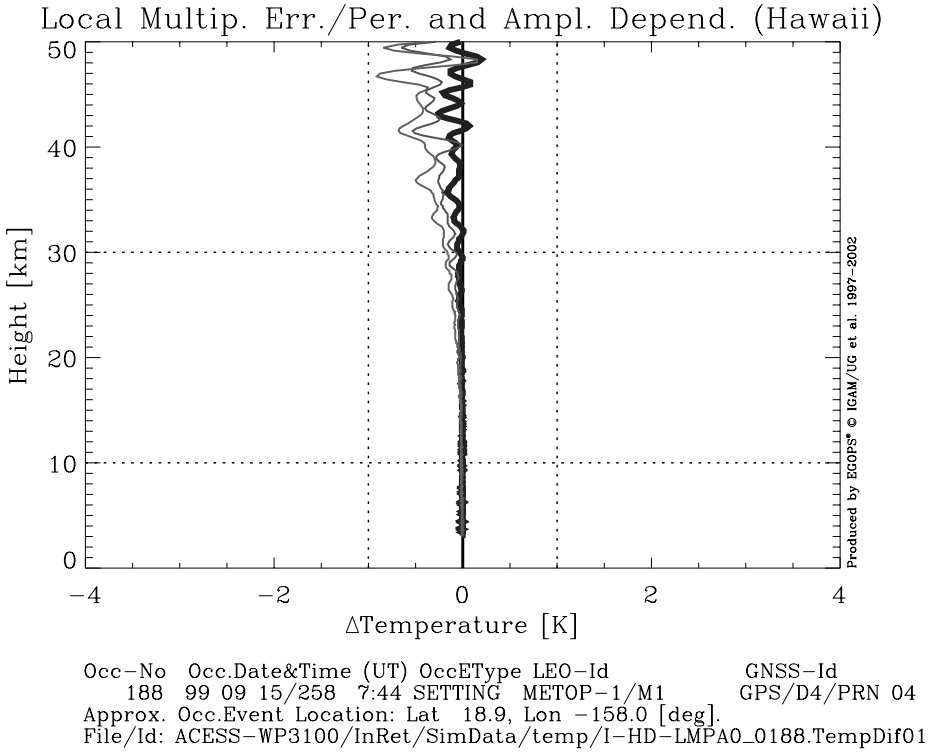

Figure 3.5.1: Temperature Errors due to Local Multipath Error/Period and Amplitude Dependence.

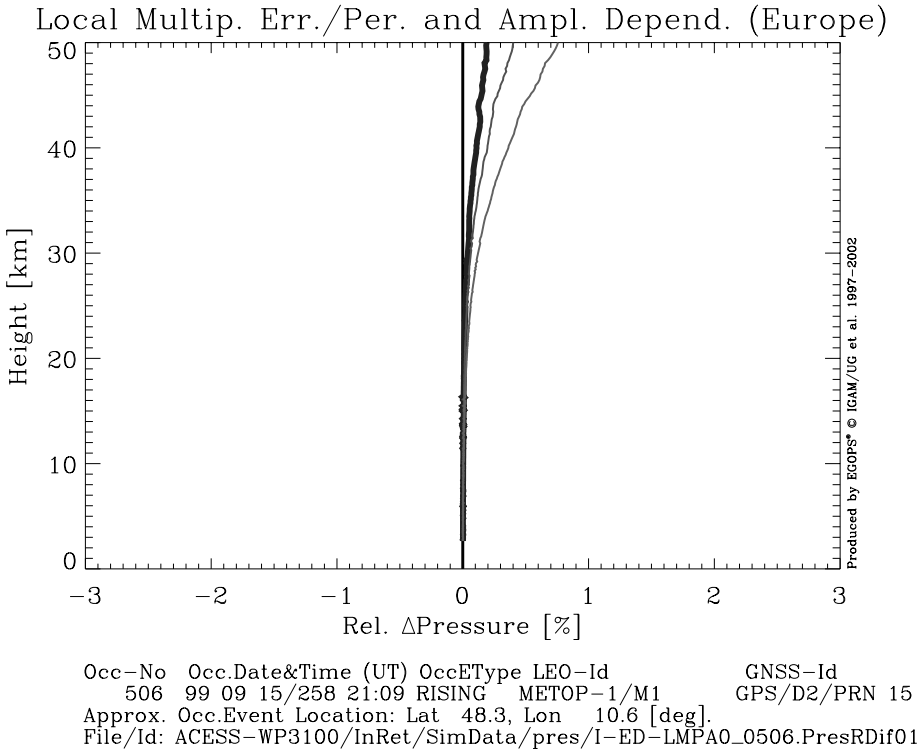

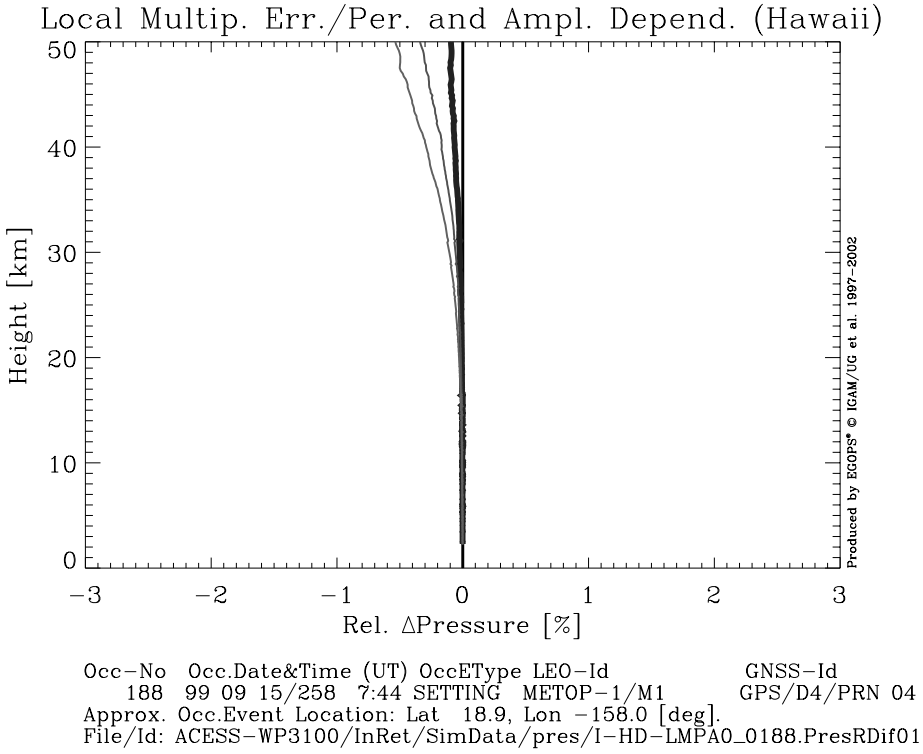

Figure 3.5.2: Pressure Errors due to Local Multipath Error/Period and Amplitude Dependence.

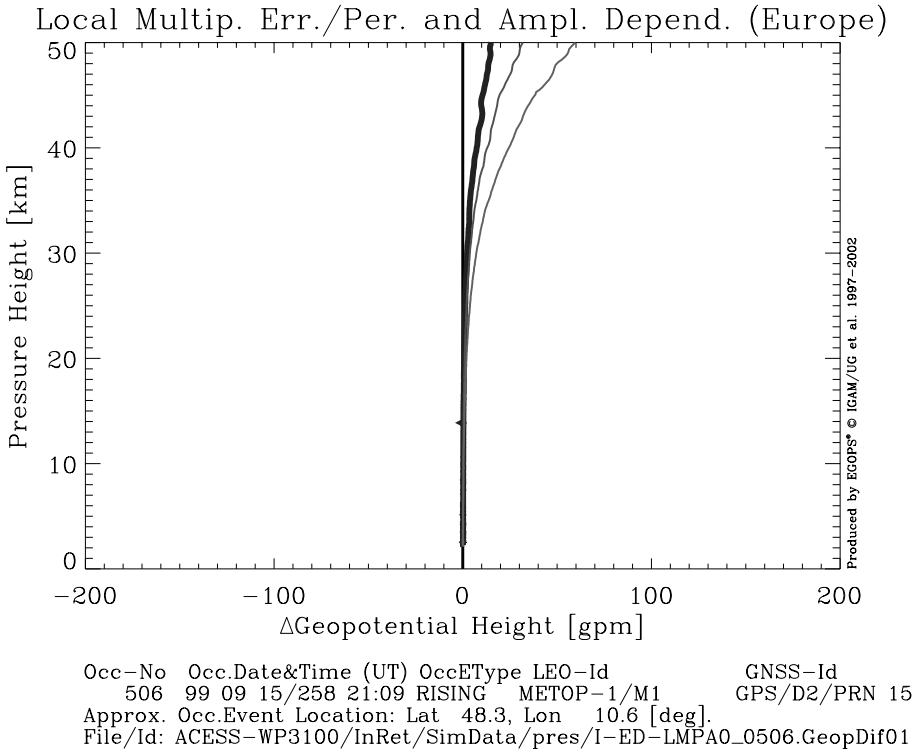

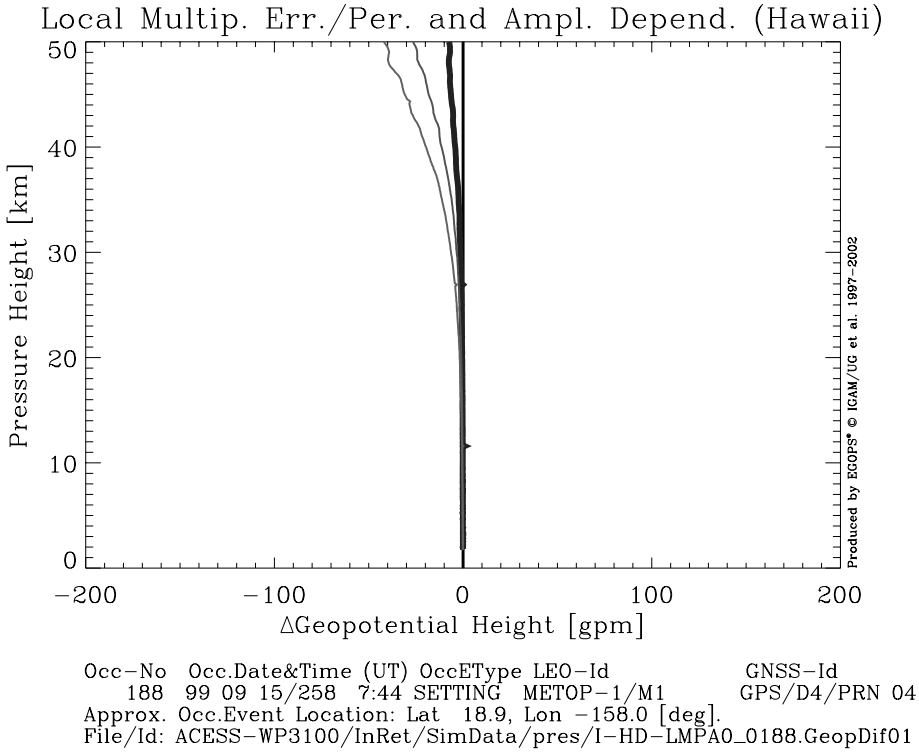

Figure 3.5.3: Geopotential Height Errors due to Local Multip. Error/Per. and Amplitude Dependence.

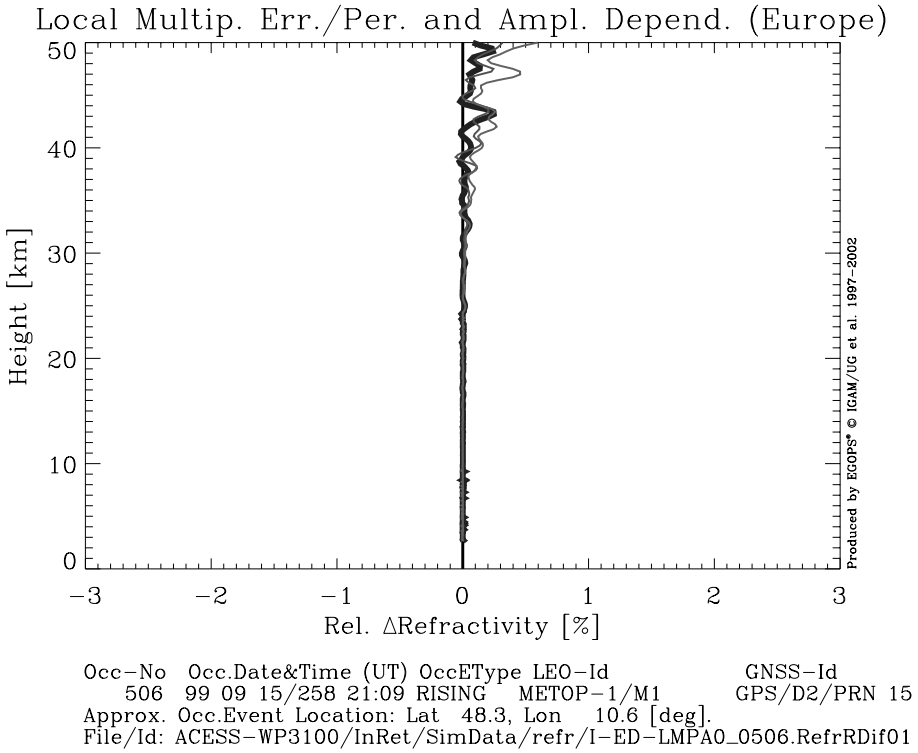

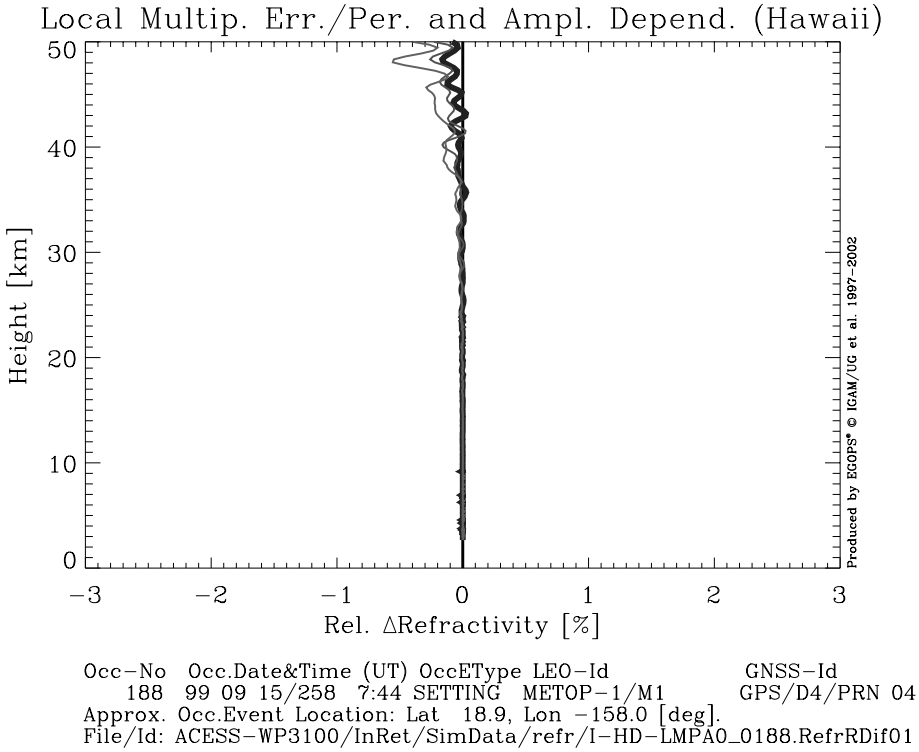

Figure 3.5.4: Refractivity Errors due to Local Multipath Error/Period and Amplitude Dependence.

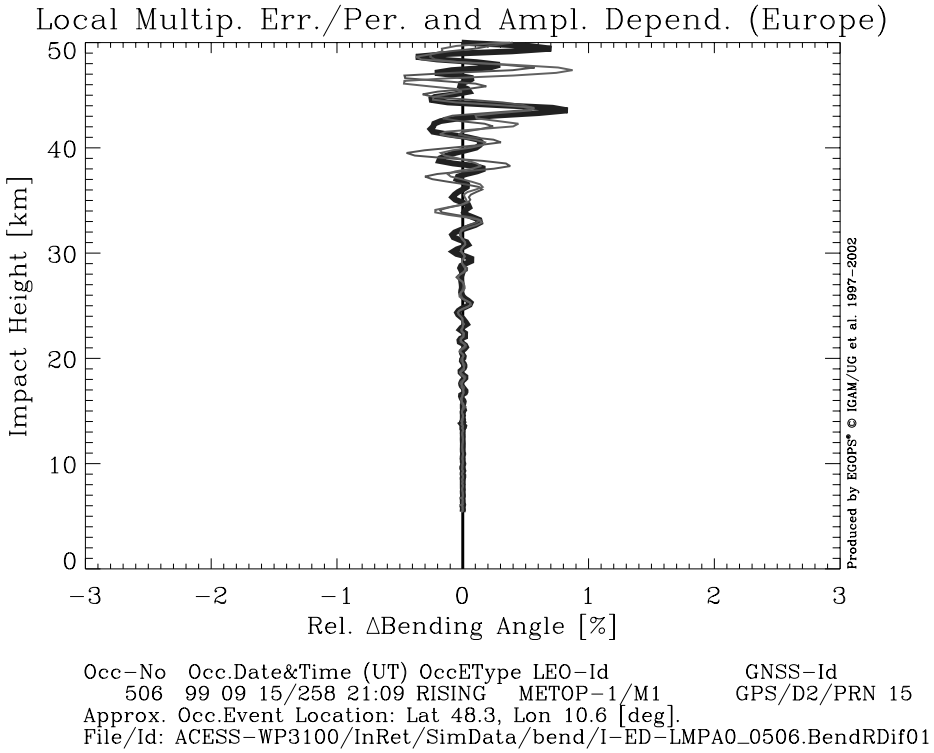

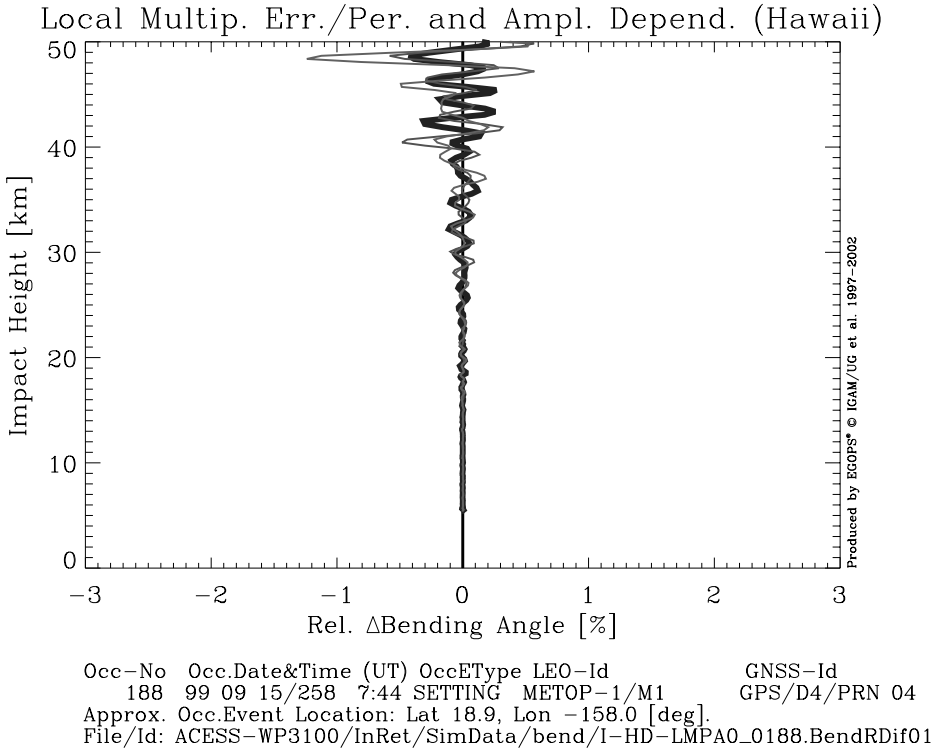

Figure 3.5.5: Bending Angle Errors due to Local Multipath Error/Period and Amplitude Dependence.

3.6. Local Multipath Errors/Phase Dependence

In this sixth and last error scenario group we analyzed the sensitivity of retrieved profiles to errors introduced by sinusoidal local multipath with different phase relative to the topmost ray of the event. Section 2.3.4 provided details on the error specifications used. Briefly recalled, the local multipath errors with focus on phase dependence were simulated via variation of the amplitude-at-topmost-ray value of the sinusoidal multipath model, while all other OSMod input parameters were kept at their standard value. The two subsets of three amplitude-at-topmost-ray values explored were: 1st subset: –1, 0, and +1 [mm], for the GRAS-type standard case of 300|1 [sec|mm]; 2nd subset: –2, 0, and +2 [mm], for the worst multipath case 100|2 [sec|mm]. The reference case, i.e., the "zero line" in the error plots, is the 0 mm case of each subset. The 1st subset represents different multipath phases for the GRAS-type standard case (marked by heavy lines in the plots, the –1 mm case heavy dotted, the +1 mm heavy solid).

The temperature error results, Figure 3.6.1, illustrate that the effects of local multipath clearly depend on the phase of the multipath variation. The cases with the wave crests at the topmost ray height (90 km), which are illustrated here, lead to higher error than the cases with the "zero-crossing" at 90 km illustrated in the previous section 3.5. The reason is that the retrieval is most vulnerable to multipath errors, if the derivatives of the sinusoidal phase variation — determining the Doppler bias due to local multipath — are strongest in the stratopause and lower mesosphere region. These derivatives are stronger in the cases shown here than in section 3.5.

In terms of magnitude, the temperature errors are, for both phases considered for the GRAS-type standard case, still < 0.1 K below 30 km and stay within 0.5 K up to the stratopause. The different-phase-cases shown for the worst multipath case (100sec/2mm) well illustrate that the phase effect is not as straightforward to understand as error magnitude effects; the time-dependent Doppler biases involved here lead to a less straightforward effect on the retrieval.

The pressure and geopotential height errors, Figures 3.6.2 and 3.6.3, are also very small up to 30 km, for the GRAS-type standard case of main interest, and moderately increase throughout the upper stratosphere. Generally, the pressure and geopotential height error structure is in line with what to expect given a temperature error structure as discussed above. Also the refractivity errors, Figure 3.6.4, are, both in their height dependence and structure, in line with what to expect given the discussed temperature error structure. As learned from the previously sections, the refractivity error behavior is generally similar to the temperature error behavior. Like in former scenarios the bending angle errors, Figure 3.6.5, are small in the lower stratosphere but then markedly increase upwards, especially at the higher-frequency scale.

The overall result is that errors in retrieved atmospheric profiles due to local multipath errors with different phases are somewhat akin to Doppler bias errors (cf. section 3.1). The error magnitude will generally be strongest if the derivatives of (sinusoidal) phase delay variations, which determine the Doppler bias due to local multipath, happen to be strongest in the stratopause and lower mesosphere region. The error magnitude found for the GRAS-type (upper bound) cases, not too much smaller than the one found for the GRAS-type Doppler bias case (section 3.1), re-enforces the closing statement of the previous section that a low multipath environment is important.

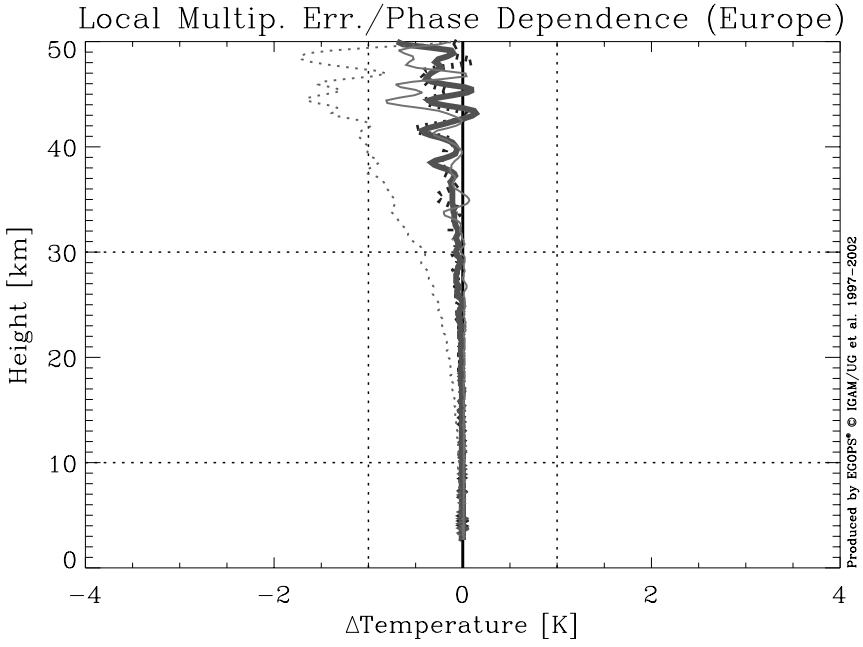

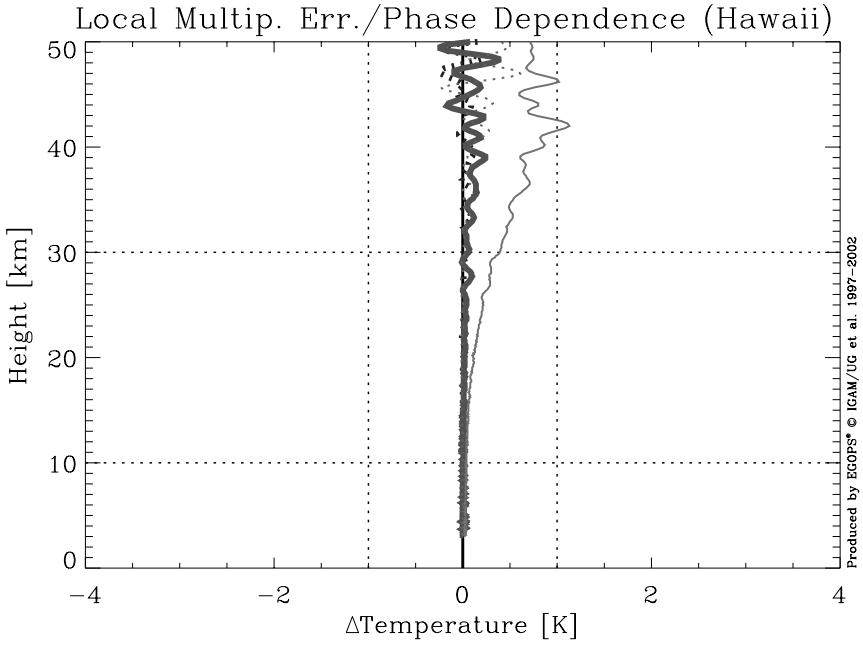

Figure 3.6.1: Temperature Errors due to Local Multipath Error/Phase Dependence.

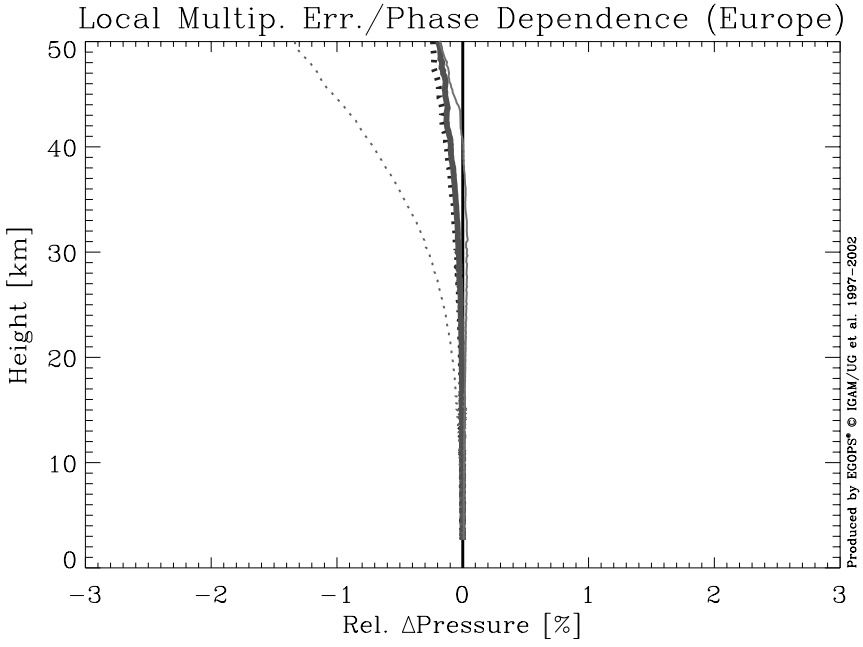

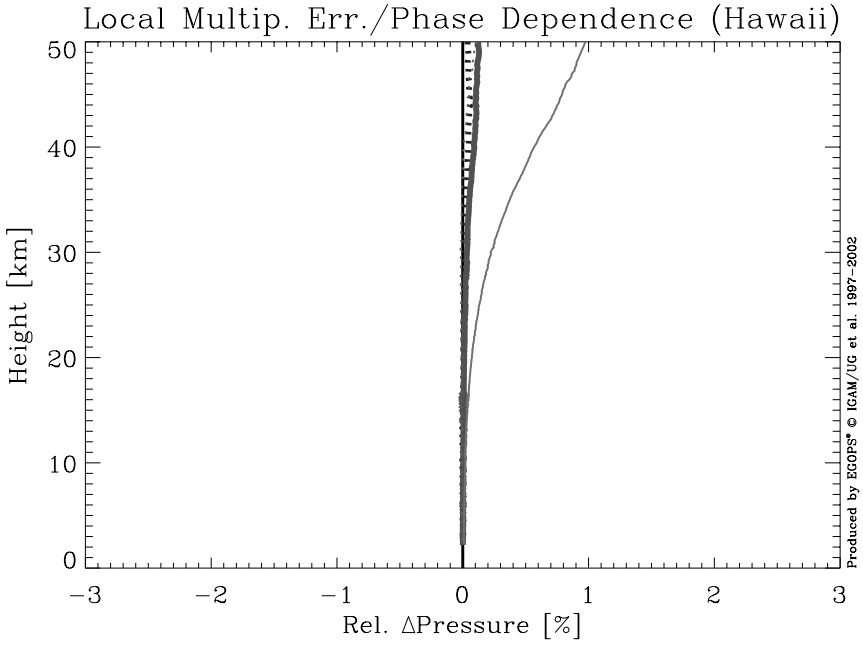

Figure 3.6.2: Pressure Errors due to Local Multipath Error/Phase Dependence.

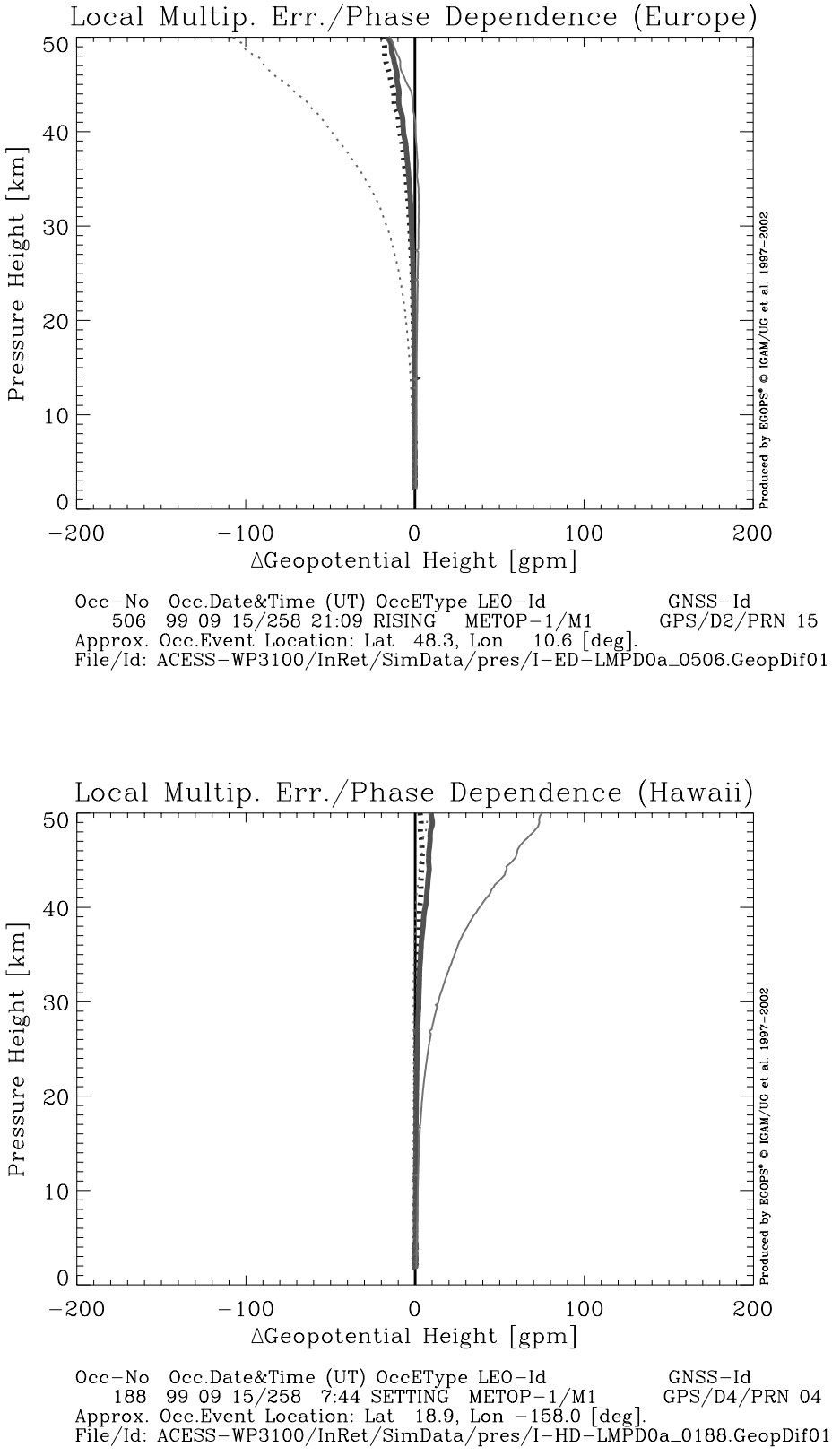

Figure 3.6.3: Geopotential Height Errors due to Local Multipath Error/Phase Dependence.

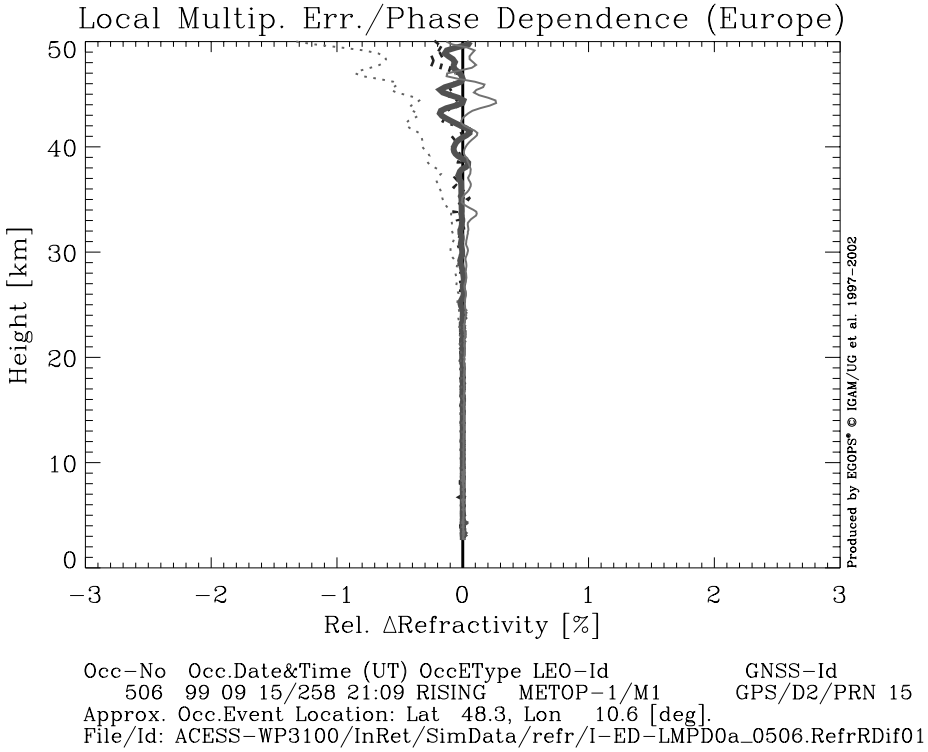

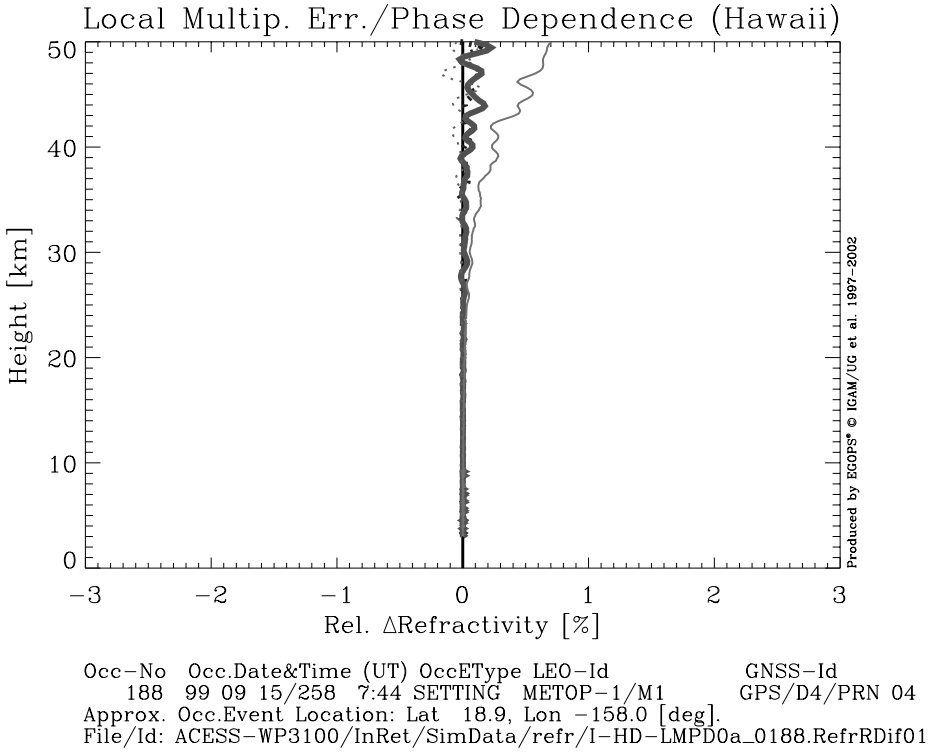

Figure 3.6.4: Refractivity Errors due to Local Multipath Error/Phase Dependence.

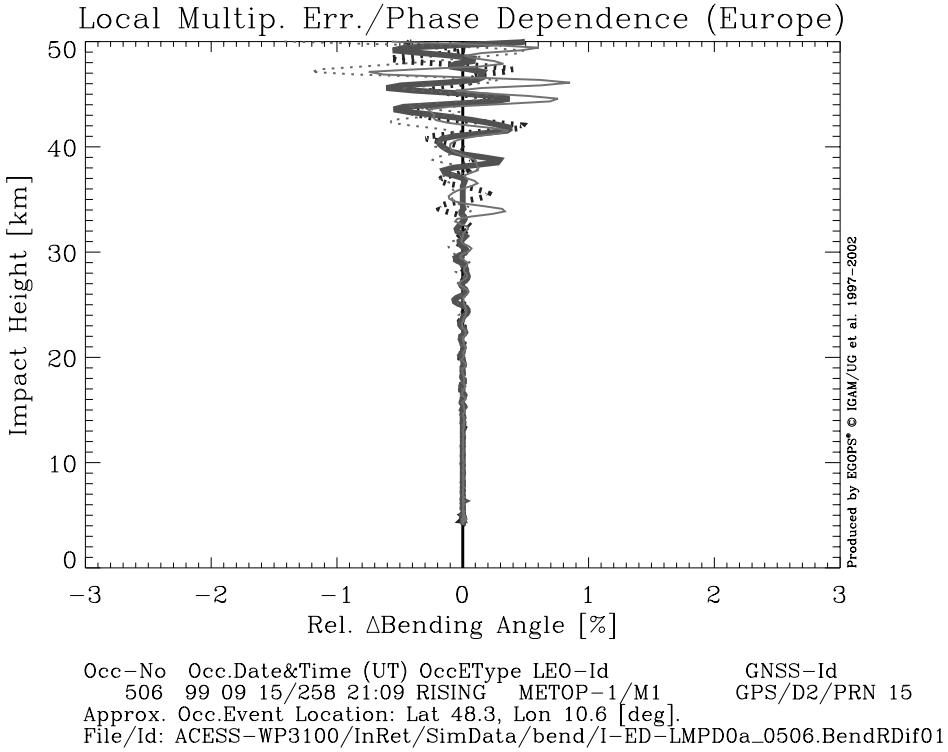

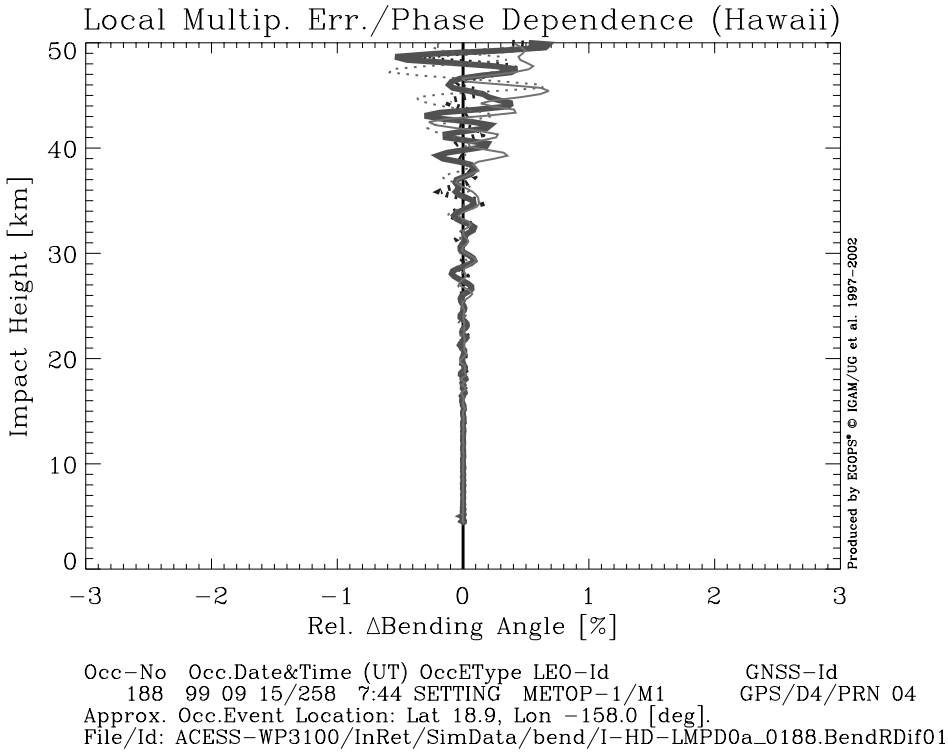

Figure 3.6.5: Bending Angle Errors due to Local Multipath Error/Phase Dependence.

3.7. Total GRAS-type Errors

In this last results subsection we analyzed the sensitivity of retrieved profiles to total GRAS-type standard errors. Detailed information on the defined OSMod standard error values and a brief discussion of the error components involved were provided in section 2.3. The error plots below exhibit the total GRAS-type errors relative to the "ideal" results (e.g., the temperature errors are obtained by subtracting temperature profiles retrieved from the "ideal" excess phase data – with zero OSMod errors – from those retrieved from the GRAS-type standard case data). The plot format is the same as in the previous sections, i.e., temperature and geopotential height errors are shown in absolute terms while pressure, refractivity, and bending angle errors are shown as percentages.

The results for the total GRAS-type errors are displayed in Figures 3.7.1 to 3.7.5, in the order temperature, pressure, geopotential height, refractivity, and bending angle.

The total GRAS-type temperature error results, Figure 3.7.1, illustrate the cumulative effects of all activated OSMod standard errors. The errors, which stay within 0.5 K below 30 km for both events, are somewhat larger for the "Hawaii" event, which is especially visible from 20 km upwards and in the pronounced oscillations in the upper stratosphere, where peak errors of about 4 K are reached from 45 km upwards. This behavior is not unexpected, given the generally worse total excess phase errors for the "Hawaii" event (see Figure 2.6).

The different character of the two events is even better visible in the pressure and geopotential height results shown in Figures 3.7.2 and 3.7.3: Whereas for the "European" event the pressure and geopotential height errors are very small throughout the entire height range of interest, the "Hawaii" event reaches error levels of about 1% (pressure) and about 80 gpm (geopotential height) near the stratopause. This indicates that these quantities are the most sensitive ones to the systematic differences in the Doppler biases between the two events, as visible in Figure 2.6 (in form of the general slope of the total phase error profiles).

The total GRAS-type refractivity errors, Figure 3.7.4, are small up to a height of 30 km (< 0.1%, generally), but grow, due to the increasing influence of thermal noise, to error levels of around 2% near the stratopause. Similarly, the total GRAS-type bending angle errors are small up to about 30 km (errors at order 0.1%) but increase to beyond 3%, in peaks of high-frequency noise, above 40 km.

The overall picture is that the total GRAS-type instrumental error budget furnishes performance to retrieve atmospheric profiles of extremely high quality up to 30 km (temperature errors < 0.5 K), still of very high quality up to near 40 km (temperature errors < 1 K), and of reasonable quality up to the stratopause (temperature errors < 2–3 K if smoothing to a resolution of ~2 km), respectively. Regarding average climatological profiles, avoidance of residual biases by careful data processing should thus allow to reach average-errors of < 0.1–0.2 K up to 40 km with ensembles as small as 30 individual events. Careful receiving system and retrieval processing design is certainly a pre-requisite to realize this performance. The results obtained here for the total GRAS-type errors indicate that such care was properly taken in the GRAS receiving system and EGOPS retrieval processing design.

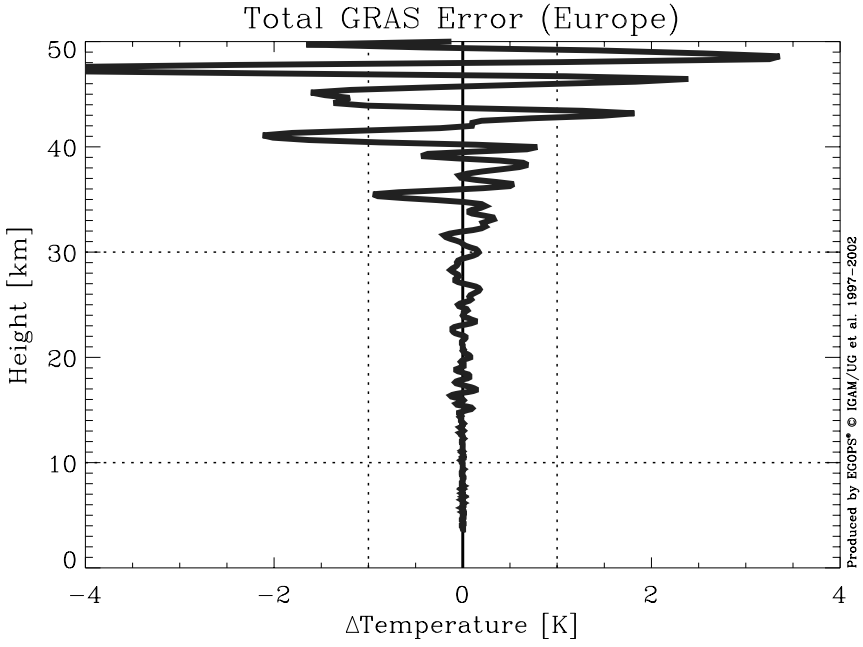

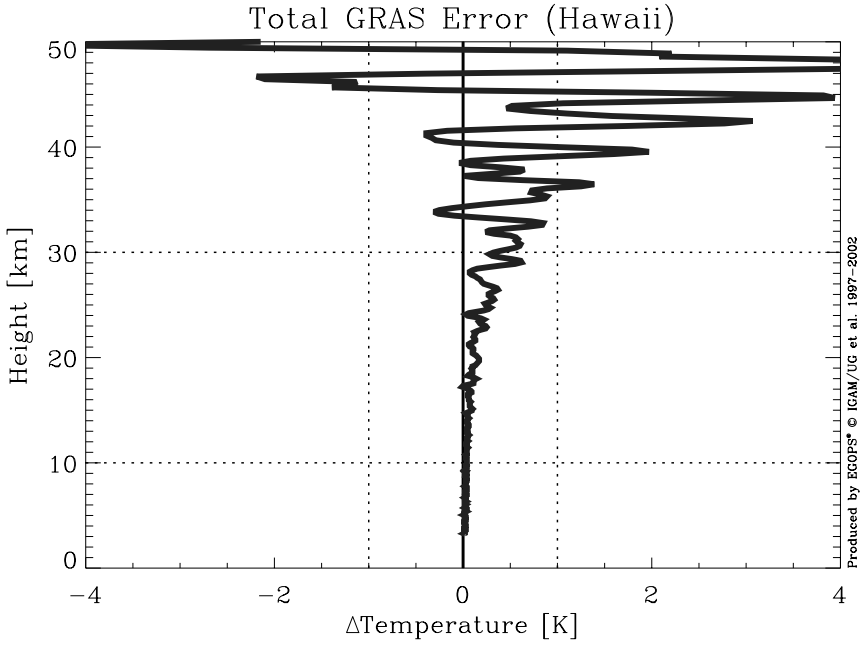

Figure 3.7.1: Temperature Errors due to Total GRAS-type Error.

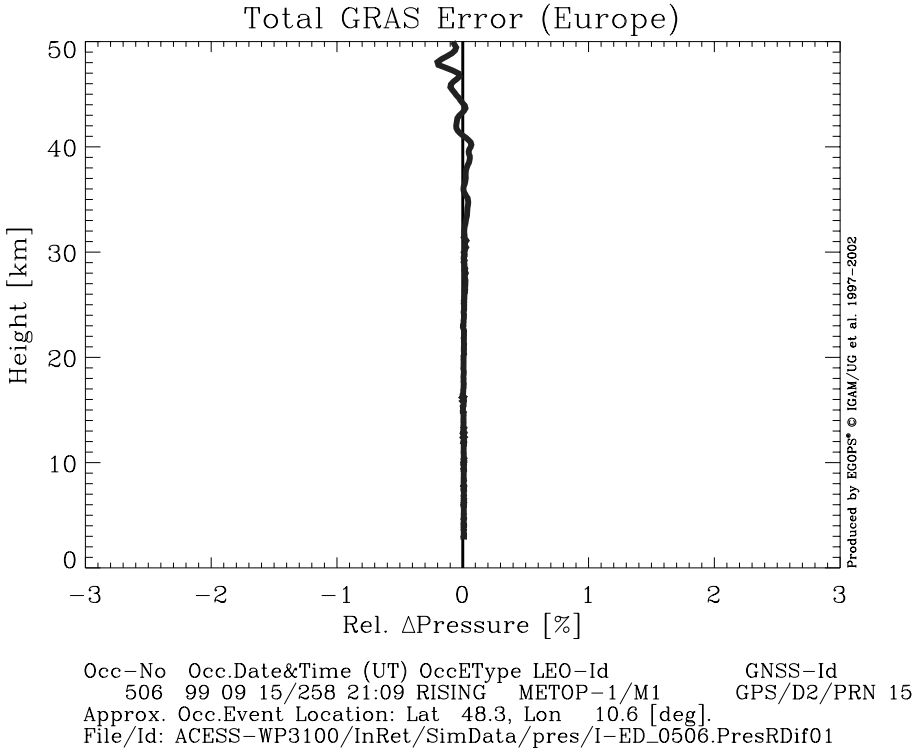

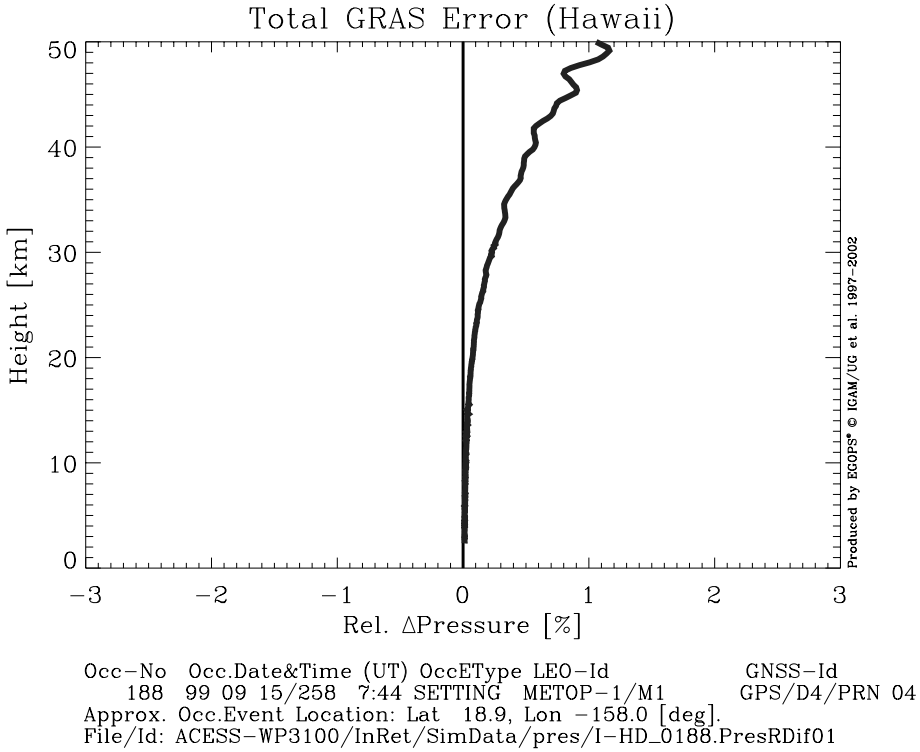

Figure 3.7.2: Pressure Errors due to Total GRAS-type Error.

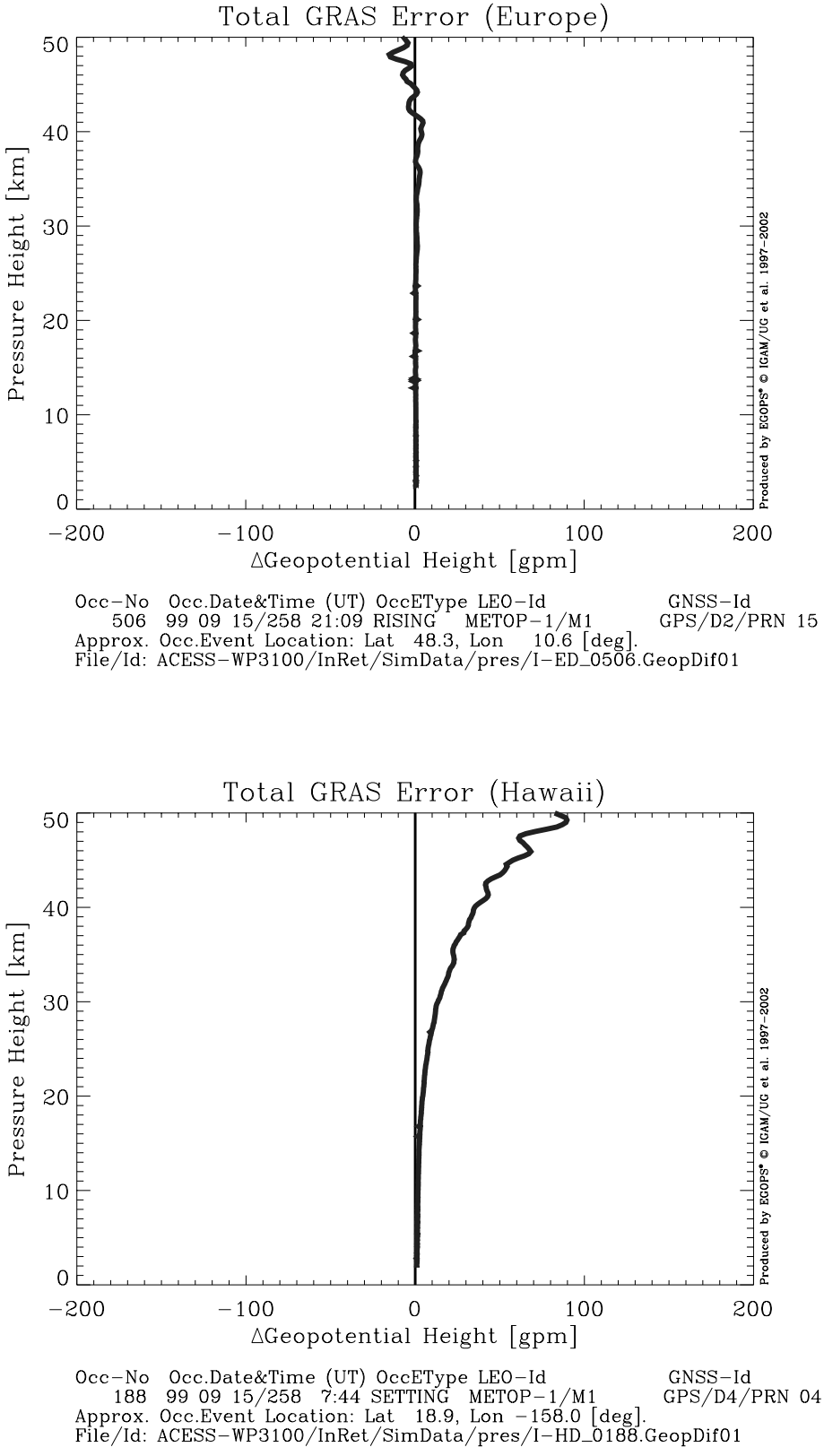

Figure 3.7.3: Geopotential Height Errors due to Total GRAS-type Error.

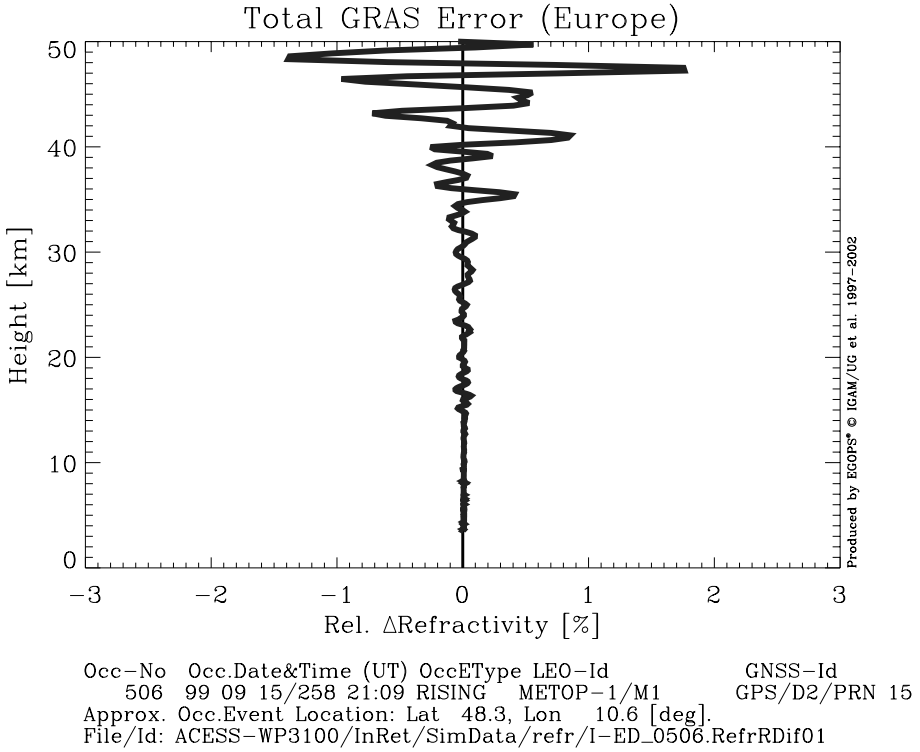

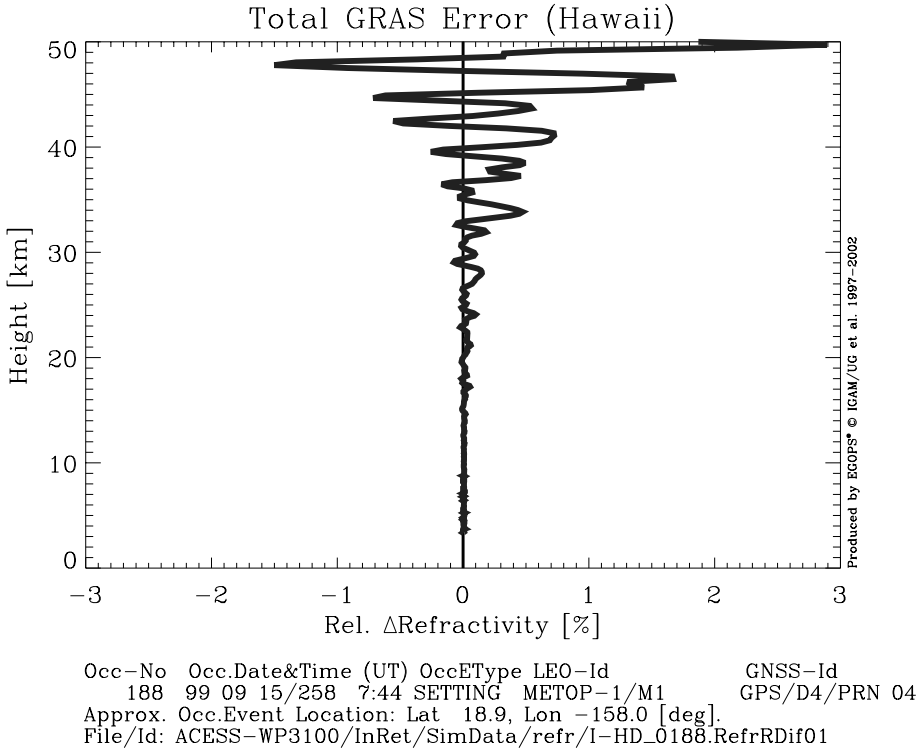

Figure 3.7.4: Refractivity Errors due to Total GRAS-type Error.

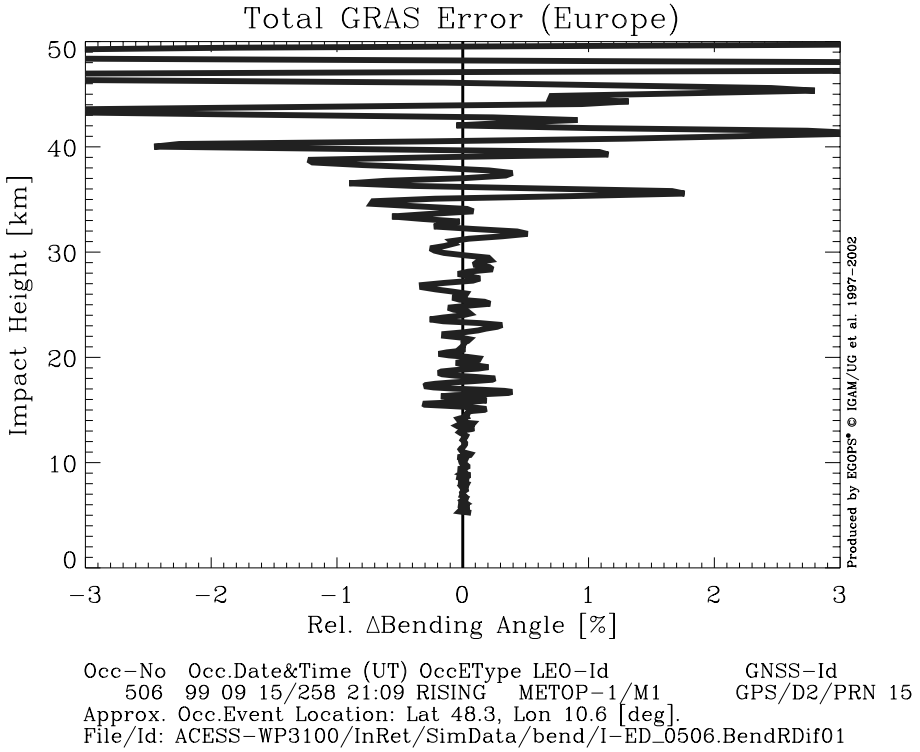

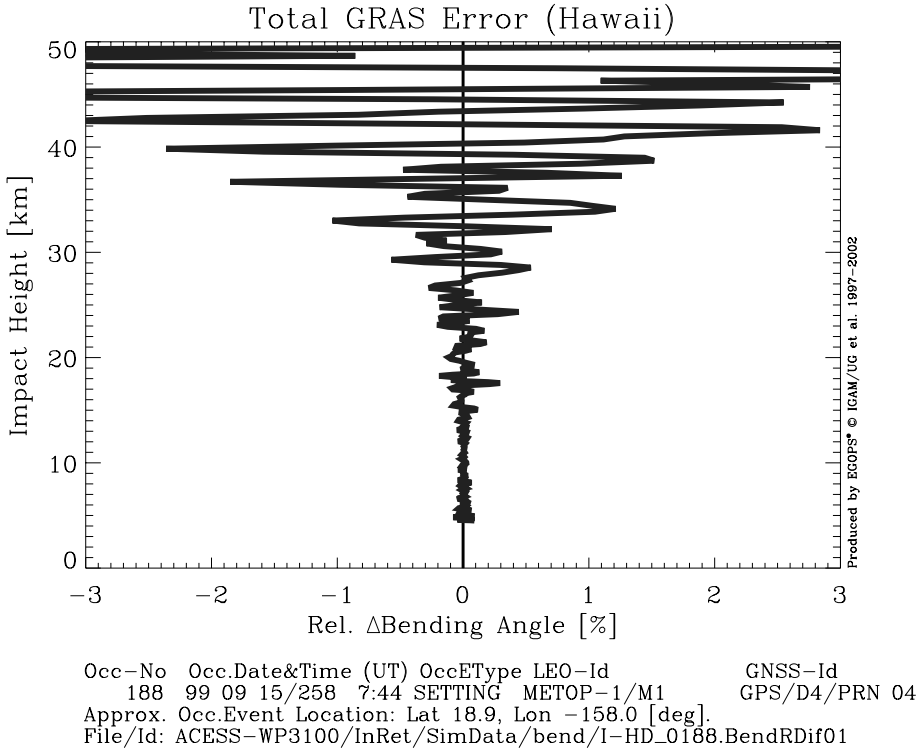

Figure 3.7.5: Bending Angle Errors due to Total GRAS-type Error.

(page intentionally left blank)

4. CONCLUSIONS AND OUTLOOK

The aim of this study was to analyze the sensitivity of atmospheric profiles retrieved from GNSS radio occultation data to observation system-related errors (also termed "instrumental errors"). The focus was on stratospheric errors, wherefore dry air retrievals were employed throughout. The effects of instrumental errors on the retrieval products temperature, pressure, geopotential height, refractivity, and bending angle were investigated in detail by a family of scenario groups, and several reasonable scenarios per group, for different error components of interest. The scenario groups addressed Doppler bias and Doppler drifts errors, clock stability/single differencing errors, receiver noise errors, and local multipath errors, the latter regarding both different (sinusoidal) multipath period/amplitude combinations as well as different phases of the (sinusoidal) variations relative to the top height of occultation events near the mesopause.

The instrumental error sources, which were found most important for ensuring high quality RO retrievals are POD-induced Doppler biases, clock stability/single differencing errors, and receiver thermal noise. Specifically, they were also found to be the major error components in the GRAS-type instrumental error budget. Doppler biases and clock/differencing errors are the major contributors to errors at the low-frequency scale (bias-like errors, but varying from event to event) while the receiver noise dominates at the high-frequency scale. These results confirm that a carefully implemented POD process, well selected ultra-stable clocks, and a careful receiver design towards low system noise temperature, and consequently low thermal noise, are key requirements in receiving system design.

A further error component of possible concern are local multipath errors, which, in general, act like time-dependent Doppler bias errors, the impact on retrievals being sensitive to the phase of (sinusoidal) phase delay errors. The retrieval error magnitudes will be strongest if the derivatives of (sinusoidal) phase delay variations, which determine the Doppler bias due to local multipath, happen to be strongest in the stratopause and lower mesosphere region. Assuming a relatively conservative scenario in the GRAS-type error budget, it was found that the impact on retrieved profiles is smaller than those of POD-induced Doppler biases, however. A low-multipath environment is nevertheless an important requirement for any GNSS receiving system.

Retrieval errors due to Doppler drifts are, favorably, safely negligible compared to errors due to Doppler biases and clock instabilities. Also in the GRAS-type budget even conservative Doppler drift values led to retrieval errors much smaller than those due to the latter sources.

In summary, the results show that the RO technique has the potential to deliver atmospheric profiles of impressively good quality, provided care is taken in receiving system and retrieval processing design. Given the results obtained for the GRAS-type specifications (temperature errors < 0.5 K up to 30 km and < 1 K up to near 40 km) it can be confirmed that such care was properly taken in the GRAS receiving system and EGOPS retrieval processing design.

Future RO system improvements such as advanced POD schemes, improved clocks& differencing treatment, further thermal noise reduction, and advanced retrieval schemes will render it possible to reduce the overall error budget even further. Thus the prospects are bright that future RO data will bring considerable benefits to climate applications such as climate change monitoring and climate model improvement.

Acknowledgments. The EGOPS software, the core tool of the study, was developed by an international consortium led by IGAM/UG and involving partner teams at Danish Meteorological Institute and TERMA Elektronik A/S, Denmark, the Met. Office, U.K., and Austrian Aerospace GmbH, Austria, with the major funding provided by the European Space Agency. The European Centre for Medium-Range Weather Forecasts (ECMWF, Reading, U.K.) provided the atmospheric analysis field used. The study was funded by the European Space Agency under ESA/ESTEC Contract No. 14809/00/NL/MM.

REFERENCES

Foelsche, U., and G. Kirchengast, Sensitivity of atmospheric profiles retrieved from GNSS occultation data to horizontal variability in the troposphere, *Techn. Report for ESA/ESTEC No. 2/2002*, Inst. for Geophys., Astrophys., and Meteorol., Univ. of Graz, Austria, 2002.

GRAS-SAG, The GRAS instrument on METOP, *ESA/EUMETSAT Rep. (ESA No. VR/3021 /PI, EUM.No. EPS/MIS/IN/9)*, 38 pp., ESA/ESTEC, Noordwijk, Netherlands, 1998.

Gobiet, A., and G. Kirchengast, Sensitivity of atmospheric profiles retrieved from GNSS occultation data to ionospheric residual and high-altitude initialization errors, *Techn. Report for ESA/ESTEC No. 1/2002*, Inst. for Geophys., Astrophys., and Meteorol., Univ. of Graz, Austria, 2002.

Hoeg, P., A.S. Jensen, H. Vedel, E. Kaas, and G. Kirchengast, ACE (Atmosphere Climate Experiment) Scientific Support Study, *Proposal to ESA/ESTEC*, 40p., Danish Met. Institute, Copenhagen, Denmark, 2000.

Kirchengast, G., End-to-end GNSS Occultation Performance Simulator overview and exemplary applications, *Wissenschaftl. Ber. No. 2/1998*, Inst. for Meteorol. and Geophys., Univ. of Graz, Austria, 1998a.

Kirchengast, G., Check of the POD performance requirements for a MAS-GRAS sensor on ISS-Alpha, *Techn. Note MPAE-MASGRAS No. 1/1998*, 12p., Inst. for Meteorol. and Geophys., Univ. of Graz, Austria, 1998b.

Kirchengast, G., J. Fritzer, and J. Ramsauer, End-to-end GNSS Occultation Performance Simulator Version 4 (EGOPS4) Software User Manual (Overview and Reference Manual), *Techn. Report for ESA/ESTEC No. 5/2001*, Inst. for Geophys., Astrophys., and Meteorol., Univ. of Graz, Austria, 2001.

Syndergaard, S., Retrieval analysis and methodologies in atmospheric limb sounding using the GNSS radio occultation technique. *DMI Scient. Report 99-6*, 131 pp., Danish Meteorol. Institute, Copenhagen, Denmark, 1999.

Ω end of document Ω